# Electromagnetic calorimeter studies for charmonium physics

Tambave, Ganesh Jagannath

**RIJKSUNIVERSITEIT GRONINGEN**

# Electromagnetic Calorimeter Studies for Charmonium Physics

**Proefschrift**

ter verkrijging van het doctoraat in de
Wiskunde en Natuurwetenschappen
aan de Rijksuniversiteit Groningen
op gezag van de
Rector Magnificus, dr. E. Sterken,
in het openbaar te verdedigen op
vrijdag 10 mei 2013
om 11:00 uur

door

**Ganesh Jagannath Tambave**

geboren op 21 februari 1984
te Dharur, India

| | |
|---|---|
| Promotor: | Prof. dr. H. Löhner |
| Copromotor: | Dr. M. Kavatsyuk |
| Beoordelingscommissie: | Prof. dr. K.-T. Brinkmann |
| | Prof. dr. N. Kalantar-Nayestanaki |
| | Prof. dr. E. Tomasi-Gustafsson |

ISBN (printed version): 978-90-367-6225-0

ISBN (electronic version): 978-90-367-6226-7

# Contents

# Chapter 1

# Introduction

The Standard Model (SM) [1] of elementary particles describes fundamental interactions of subatomic particles, namely, the electromagnetic, weak, and strong interactions. The electromagnetic and weak interactions are described in the electroweak theory [2] and the strong interaction by Quantum Chromodynamics (QCD) [3]. The SM particles are spin-1/2 fermions (quarks, leptons) and spin-1 gauge bosons. There are six quark flavours known as up, down, charm, strange, top, and bottom arranged in three families. The corresponding three lepton families are electron, muon, tau, together with their electron-, muon- and tau-neutrino. The gauge bosons are the photon, gluons, Z and W bosons acting as force carriers of electromagnetic, strong, and weak interaction, respectively. The recent discovery [4, 5] of a resonance at the expected position of the Higgs boson may complete the SM but it will take further analysis to confirm the scalar nature of this resonance, as is required for the Higgs boson.

The SM has been very successful in predicting the interactions of quarks and leptons in particular at the short-distance scale. While the SM provides a very good description of phenomena observed by experiments at high energies, it is still an unsatisfactory theory. As an example, at the long-distance scale of QCD at low energies, phenomena such as the quark confinement in the non-perturbative regime, the possible existence of glueballs and hybrids, and the origin of the masses of hadrons are not yet firmly derived from QCD and pose a challenge to the

complete understanding of the nature of the strong interaction [6, 7]. The Higgs mechanism might be responsible for the masses of the fundamental particles, but the mass-creation mechanism for hadrons is different. Only a few percent of the proton mass in the form of the bare quark masses is due to the Higgs mechanism. The remaining mass is created by the strong interaction in a way that is not very well understood. The spectroscopy of glueballs and mesons in the charmonium mass region can help to answer these questions. The charmonium system is particularly suited due to the high mass ($\approx$ 1.5 GeV/c$^2$) of the charm quark allowing a description of the dynamical properties of the charmonium system in terms of a non-relativistic potential model with relativistic corrections such as the spin-orbit and spin-spin interactions. The free parameters in this model are to be determined from a comparison with experimental data [8]. Experimental techniques such as electron-positron or antiproton-proton annihilations can be used to study the charmonium system. The discoveries and detailed studies of resonances and decay properties will help to further develop the theoretical framework and to completely understand the nature of the strong interaction.

The hadron physics experiments BESIII [9] and PANDA [10] are designed to perform these spectroscopic studies. The BESIII experiment, based at IHEP Beijing, is currently running in production mode, and has produced a large amount of data samples using electron-positron annihilations at center-of-mass energies between 3 and 4.6 GeV. The future PANDA experiment is based at the FAIR accelerator complex [11] in Darmstadt, Germany. The PANDA experiment will study antiproton-proton annihilations at center-of-mass energies between 2 and 14 GeV. Both experiments make use of advanced multi-purpose detector systems with almost $4\pi$ coverage. The detection systems mainly consist of charged-particle trackers, time-of-flight measurements for precise timing, muon counters, and an Electromagnetic Calorimeters (EMC) to measure the energy of photons, electrons, and neutral mesons.

The work described in this thesis is completely focused on the research and development of the PANDA and the BESIII EMC. For the PANDA experiment, one of the important milestones was the development and the verification of the Front-End Electronics (FEE), the corresponding Feature-Extraction (FE) algorithms, and the readout chain of the Electromagnetic Calorimeter (EMC) [12]. The project completed in the presented thesis research has two main challenges:

the high hit-rate capability and the reliable on-line data processing without any hardware trigger.

PANDA is a fixed-target experiment operating at an annihilation rate up to 20 MHz. Due to this high rate the PANDA EMC will be exposed to single-detector hit rates of up to 1 MHz, causing overlap or pile-up of detector signals. Therefore, the FEE, its FE algorithm and the data treatment in the subsequent readout chain have to be capable to handle high hit-rates at the detector. For the FE algorithms, to identify and recover the information of the pile-up signals, the pile-up identification and pile-up recovery algorithm has been developed and successfully tested using simulated and experimental pile-up signals.

In order to gain high flexibility for the physics event selection, the PANDA experiment will employ a new approach of a readout system without any hardware trigger, i.e. a trigger-less data-acquisition system. The event-selection is based on high-level reconstructed information, e.g. invariant mass, secondary vertices, and time correlations, which may be contributed from all sub-detector systems. Therefore, the FEE and the readout chain of the EMC need to be very intelligent for the on-line data processing. To this end, the EMC prototype detector, the FEE and the readout chain, as well as the pile-up identification and recovery algorithms have been developed and successfully tested in a tagged-photon beam.

In the last part of the thesis, the performance of different methods suited for the on-line reconstruction of electromagnetic showers has been studied to obtain the best possible shower-energy reconstruction and hence energy resolution. The performance was tested using simulations, and validation studies were carried out using the BESIII experimental data. The charmonium electric dipole (*E1*) transition $\psi^{'} \rightarrow \gamma\chi_{cJ}$ $(J = 0, 1, 2)$ has been studied using selection criteria which are as simple as possible and at the same time as reliable as possible so that they are well suited for the on-line processing in the PANDA experiment.

The outline of the thesis is as follows:

**Chapter 2**: In this chapter the theoretical background for the envisaged charmonium studies with PANDA and BESIII is discussed in brief. We give an introduction to the theory of QCD, the potential models, and Lattice QCD predictions; the glueball spectrum and radiative charmonium transitions will be discussed.

**Chapter 3**: This chapter gives an overview of the PANDA and the BESIII experiments. The first and the second section of the chapter are dedicated to the discussion of the PANDA experiment and the detector system. The physics goals of the planned experiment, the High-Energy Storage Ring (HESR) where the PANDA detector will operate, and the target systems are discussed. The details of the PANDA detector components, the on-line data selection and data acquisition, and the data analysis software PandaROOT are described. In the last section, some relevant aspects of the BESIII experiment are discussed. The BESIII physics program, design and operation of the BESIII detector, trigger and data acquisition, and the data analysis software BOSS are explained.

**Chapter 4**: The PANDA EMC is described in this chapter. The general principles relevant to the EMC are discussed. The EMC requirements for the PANDA experiment, the PANDA EMC design, its front-end electronics, and the concept and the prototype of the PANDA EMC readout chain, designed for on-line data-processing, are described in some detail.

**Chapter 5**: In the PANDA experiment, due to high (up to 20 MHz) annihilation rates, the EMC will be exposed to single-detector hit rates of up to 1 MHz, which will lead to pulse overlap. Hence, to identify and recover energy and time information of the overlapping pulses, a pulse pile-up identification and recovery method is developed. This chapter is dedicated to the recovery algorithm and its performance in the Front-End electronics of the PANDA EMC.

**Chapter 6**: This chapter is dedicated to the EMC prototype-detector design (proto9), the performance test of the readout chain and the pile-up identification and recovery algorithm using tagged photons at the MAMI accelerator facility in Mainz, Germany.

**Chapter 7**: This chapter is dedicated to the various studies of clustering-methods carried out to achieve the best possible shower-energy reconstruction and hence energy resolution. These methods are very important in the higher level of the readout chain of the calorimeter. In the PANDA EMC readout chain such methods will be used in the Compute Node (CN) stage where the on-line clustering and shower reconstruction will be performed. Moreover, in the PANDA experiment the data will be processed on-line in FPGAs. Therefore, it is very important to have simple but effective event-selection criteria which will

use as little resources as possible. In this context, as an example, simple event-selection criteria have been used to perform the branching-fraction measurement of the electric dipole ($E1$) transition $\psi^{'} \rightarrow \gamma\chi_{cJ}$ ($J = 0, 1, 2$). The results are compared to an advanced off-line analysis.

# Chapter 2

# Theoretical Background

The physics goals of the BESIII and the PANDA experiments are mainly focused on strong-interaction studies and, in particular, on the study of the quark-gluon confinement in the non-perturbative regime. Therefore, in this chapter an introduction to QCD, the theory of strong interactions, and associated potential models is given in section 2.1 and section 2.2, respectively. A brief introduction to Lattice QCD and its predicted glueball mass spectrum is discussed in section 2.3. Moreover, the theoretical background of radiative charmonium transitions is briefly discussed in section 2.4. The electromagnetic calorimeter plays a crucial role in the studies of radiative transitions. The radiative charmonium transition $\psi^{'} \rightarrow \gamma\chi_{cJ}$ $(J = 0, 1, 2)$ is studied (see chapter 7) for the validation of the shower-energy reconstruction method using data collected by the BESIII experiment.

## 2.1 Introduction to QCD

The interaction between quarks, mediated by gluons, is called the strong interaction. It binds quarks and anti-quarks in baryons and mesons. The strong interaction is described by an SU(3) gauge theory, called Quantum Chromodynamics (QCD) [3]. The term chromodynamics refers to the new quantum number

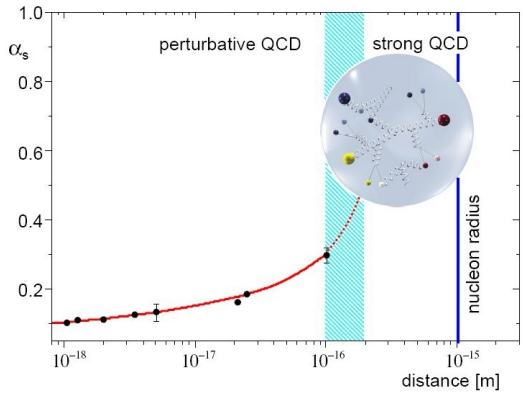


*Figure 2.1: The strong coupling constant $\alpha_s$ as a function of the distance scale [13].*

*color* introduced in the theory. According to QCD the quarks carry *color charge* denoted as *red*, *blue*, and *green*. The strong-force carrier gluon is color charged and carries a color and an anti-color. Three colors and their anti-colors can be combined to nine possible states. One of these states is a linear combination of red anti-red + blue anti-blue + green anti-green and must be non-interacting; the remaining eight states correspond to eight gluons [3]. The gluons may self-interact and couple to each other resulting into the formation of *glueballs* made up from two or more gluons. Such states have not been confirmed so far.

Two main properties of QCD are *quark confinement* and *asymptotic freedom* illustrated in Fig. 2.1. The *quark confinement* states that isolated free quarks cannot exist in nature. The interaction between the quarks gets stronger as the distance between them gets larger; beyond a certain distance the stored energy results in the formation of a new quark-antiquark pair. Consequently, we can not observe quarks as free particles. Conversely, as the distance between quarks gets shorter the interaction strength between quarks becomes smaller and this phenomenon is called *asymptotic freedom*. The *quark-confinement* phenomenon is well described in the perturbative regime but in the non-perturbative regime a quantitative description is still lacking. Since at low energies the strong coupling constant (the expansion parameter) becomes too large, the interaction of quarks with the gluon field cannot be treated perturbatively. Therefore, the PANDA

and the BESIII experiments are designed to study the quark-gluon confinement phenomenon in the non-perturbative regime. These experiments will focus on the spectroscopy of glueballs and mesons in the charmonium mass region. In this energy regime the high mass ($\approx 1.5$ GeV/c$^2$) of the charm quark allows a description of the dynamical properties of light charmonia in terms of a non-relativistic potential model with relativistic corrections such as the spin-orbit and spin-spin interactions. For heavy charmonium systems non-perturbative phenomena have sizable contributions [14].

## 2.2 Potential models

The Dynamics of the charmonium system is described in analogy with positronium and treated in the non-relativistic limit by means of the Schrödinger equation with a potential $V_{short}(r)$. Here, $r$ is the distance between the quark and the anti-quark. At short distances, single gluon exchange is approximated by a Coulomb-like interaction [1]:

$$V_{short}(r) = -\frac{4}{3}\frac{\alpha_s(r)}{r} \tag{2.1}$$

where $\alpha_s$ is the QCD coupling constant. A factor $\frac{4}{3}$ arises from requiring the quark and anti-quark to be in a color singlet state. This form of the potential is similar to a QED potential except the coupling constant $\alpha_s$, as compared to $\alpha = \frac{1}{137}$. The strong coupling constant is given by [1]:

$$\alpha_s(Q^2) = -\frac{4\pi}{[11 - (2/3)n_f]\ \ln(Q^2/\Lambda^2_{QCD})} \tag{2.2}$$

where $n_f$ is the number of fermion flavors with mass below momentum transfer $Q$ and $\Lambda_{QCD}$ is a QCD scale parameter. Asymptotic freedom is displayed since $\alpha_s(Q^2) \to 0$ as $Q^2 \to \infty$. It is clear from equation 2.2 that the perturbation theory breaks down at $Q^2 = \Lambda^2_{QCD}$, when the effective coupling constant becomes infinite. Small values of $Q^2$ are associated with large distances, and the inverse of $\Lambda_{QCD}$ is called the confinement length. As the distance between quarks increases,

the potential increases as stated in the long-distance potential:

$$V_{long}(r) = kr \tag{2.3}$$

where $k$ is a force constant with a value about 1 GeV/fm. The combination of these two extreme distance potentials is called *Cornell potential* [15] given by:

$$V(r) = -\frac{4}{3}\frac{\alpha_s(r)}{r} + kr \tag{2.4}$$

This simple potential resembles a Coulomb-like interaction at short distances and an approximately linear rise at large $r$ describes very well the spacing of the charmonium resonances. The extended description of the potential to spin-dependent interactions is documented in Ref. [14].

## 2.3 Lattice QCD and Glueball spectrum

Lattice QCD (LQCD) is a nonperturbative numerical method to determine the low-energy properties of QCD. LQCD was proposed by K. Wilson in 1974 [16]. In LQCD the fields representing quarks are defined at the sites of a four-dimensional space-time lattice while the gluon fields are defined on the links connecting neighboring sites. Glueballs predicted by LQCD are exotic since their structure does not follow the quark model. There are several candidates of glueball resonances observed experimentally [17, 18] but more studies are required to establish the glueball predictions. These glueball candidates have symmetry properties which are allowed for conventional meson states from the quark model. Therefore, it is difficult to uniquely identify these states as glueballs. There is very limited knowledge about the nature of glueballs and the confined QCD vacuum, which needs to be improved by nonperturbative approaches. The numerical LQCD calculates the glueball mass spectrum [19] and predicts glueball masses in the range of 1 GeV to 5 GeV as shown in Fig. 2.2. The masses of the lowest-lying glueballs range from 1 GeV to 3 GeV and suggest that the radiative decays of $J/\psi$ are ideal hunting grounds for glueballs in the charmonium region [22]. In $J/\psi$ radiative decays, the $c\bar{c}$ system decays into a photon and two interacting gluons form a flavor singlet. Large yields for singlet production and small octet yields are expected [14]. In

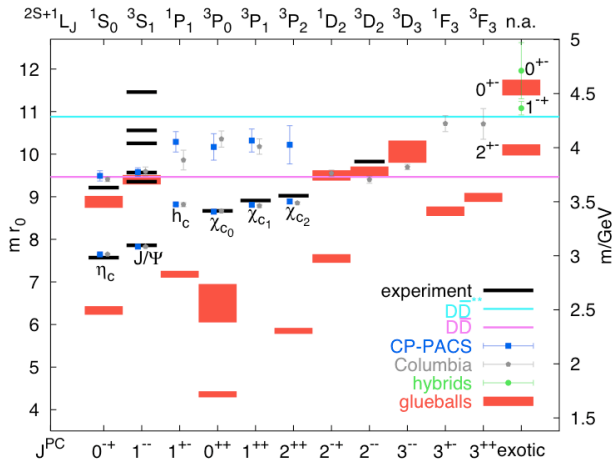


*Figure 2.2: The LQCD predicted glueball mass spectrum [19] together with charmonium states. The masses shown on the left vertical axis are given in terms of $r_0$ ($1/r_0 \approx 400$ MeV) where $r_0$ is the hadronic scale parameter. The masses on the right vertical axis are in* GeV*. The statistical uncertainty in the glueball mass is denoted by the height of each colored box. The horizontal axes denote the quantum numbers: in terms of spin-parity and charge conjugation, shown on the lower axis, and in spectroscopic notation on the upper axis. The experimentally observed resonance states are indicated by horizontal black lines. The pink and blue lines show the $D\bar{D}$ and $D\bar{D}^{**}$ thresholds. The blue and gray points with error bars are the calculations done by Columbia [20] and CP-PACS [21] collaborations.*

the predicted mass region, the PANDA experiment will perform $\bar{p}p$ annihilations and aims to study these radiative decays of $J/\psi$ for glueball search [6]. Glueballs with exotic symmetry properties are of particular interest for the PANDA experiment, since the discovery of such particles would firmly prove the validity of QCD in the non-perturbative regime. Recently, the isoscalar-meson spectrum was extracted using LQCD [23] in quite good agreement with experimental observations. The isoscalar mesons are the mesons with all flavor quantum numbers equal to zero. The reported spectrum also includes states of high spin and, for the first time, light isoscalars with exotic $J^{PC}$. These computational studies demonstrate that LQCD can reproduce the pattern of single-particle isoscalar states observed in nature. Therefore, predictions of glueball states may be taken with some confidence.

## 2.4 Charmonium radiative transitions

The annihilation of a charm and anti-charm ($c\bar{c}$) pair causes the decay of a charmonium state into light particles. Plenty of such decays have been measured, which are reported in the particle data book [24]. These charmonium state transitions (see Fig. 3.3) are classified as hadronic and radiative transitions. In this section, radiative transition are discussed in particular, since they offer an insight into the internal structure of heavy-quark bound states within QCD. Moreover, they are most sensitive to the properties of the electromagnetic calorimeter and the applied analysis techniques.

Since charmonium can be treated as a non-relativistic system, one can apply the standard multipole expansion in electrodynamics [25] to the calculation of charmonium radiative transitions. The interaction of a non-relativistic $c\bar{c}$ pair in the electromagnetic field is described by a non-relativistic Hamiltonian [14] using leading terms in the multipole expansion for *E1* and *M1* transitions:

$$H_{E1} = -e_c e(\vec{r} \cdot \vec{E}) \quad \text{and} \quad \mathrm{H_{M1}} = -\mu_\mathrm{c}(\tilde{\Delta} \cdot \tilde{\mathrm{B}}) \tag{2.5}$$

Here $e_c = 2/3$ is the charge of the charm quark, $\mu_c = e_c e/(2m_c)$ is the magnetic moment of the charm quark, $m_c$ is the mass of the charm quark and $\vec{\Delta}$ is a spin operator defined as $\vec{\Delta} = \vec{\sigma_1} - \vec{\sigma_2}$ with $\vec{\sigma_1}$ and $\vec{\sigma_2}$ acting on the $c$ and $\bar{c}$ quarks, respectively. Here $\vec{\sigma_1}$ and $\vec{\sigma_2}$ are Pauli matrices. The $\vec{E}$ and $\vec{B}$ denote the electric and magnetic fields, respectively.

The total decay rate[1] can be calculated for both the *E1* and *M1* transitions. The electric dipole term (*E1*) describes the transitions between $L = 0$ and $L = 1$ states with the same spin $S$ of the quark pair. The magnetic term (*M1*) describes transitions between $S = 1$ and $S = 0$ with the same orbital momentum $L$. Since the mass of charmonium is larger than the energy of the emitted photons, the electric dipole transitions are dominant. The general dipole formula for the total decay rate is

$$\Gamma(i \to f + \gamma) = \frac{4}{3} e_c^2 \alpha E_\gamma^3 \ \mid \langle f \mid r \mid i \rangle \mid^2 \tag{2.6}$$

[1]The decay rate is obtained using the sum over photon polarizations and the integration of the transition probability over phase space. The complete derivation of the total decay rate is documented in Ref. [26].

where $e_c = 2/3$ is the electric charge of the charm quark, $\alpha$ is the fine structure constant, $E_\gamma$ is the energy of the radiative photon, and the matrix element involves the normalized initial and final state wave functions. As an example, the transition rate for the spin-triplet state $2\ ^3S_1 \rightarrow 1\ ^3P_J\gamma$ induced by the *E1* component of the Hamiltonian (see equation 2.5) is

$$\Gamma(2\ ^3S_1 \rightarrow 1\ ^3P_J\gamma) = (2J+1)\frac{4}{27}e_c^2\alpha E_\gamma^3\ \ |\ \langle 1P\ |\ r\ |\ 2S\rangle\ |^2 \tag{2.7}$$

where the term $2J+1$ is the statistical weight of a definite $J$ state. The extra factor 9 in the denominator is the total number of states for two vector particles. The ratio of equation 2.7 and equation 2.6 is equal to the branching fraction of the decay mode $2\ ^3S_1 \rightarrow 1\ ^3P_J\gamma$.

# Chapter 3

# Overview of the Experiments

PANDA and BESIII are hadron physics experiments. PANDA is a $\bar{p}p$ annihilation experiment planned at the FAIR facility near GSI in Darmstadt, Germany. The experiment involves more than 450 scientist from 18 different countries. The construction of the FAIR accelerator complex is in progress since 2012 and preassembly of the PANDA detector will start in the year 2014. BESIII is an $e^+e^-$ annihilation experiment located at IHEP, Beijing, China. More than 200 scientists from 12 different countries are working in this experiment. BESIII has successfully collected the world's largest data set of charmonium states at center-of-mass energies corresponding to the $J/\psi$, $\psi(2S)$ and $\psi(3S)$ meson masses. During the past two years, BESIII has published many important results on the measurement of newly discovered decay modes of the charmonium states, thus successfully contributing to the research field of hadron physics.

In this chapter, the PANDA and the BESIII experiments are discussed. Section 3.1 gives an overview of the PANDA experiment comprising the PANDA physics program, the high energy storage ring, and a discussion of target and luminosity. Section 3.2 contains the details of the PANDA sub-detectors, the concept of the readout electronics, and the trigger. Section 3.3 is dedicated to

the BESIII experiment. We introduce its physics goals, the accelerator and the detector system, the trigger and data acquisition, and the off-line analysis software package BOSS.

## 3.1 The PANDA experiment

The PANDA (antiProton ANnihilation at DArmstadt) experiment [10] is one of the important hadron physics experiments because of its rich physics program. The PANDA physics program is summarized in section 3.1.1. It ranges from charmonium spectroscopy to the search for exotic hadrons and from strange baryon spectroscopy to nucleon structure studies as well as hypernuclear physics. The PANDA experiment is located at the future Facility for Antiproton and Ion Research (FAIR) [11] [27] which is currently under construction at GSI [28], Darmstadt, Germany. An overview of the FAIR facility is shown in Fig. 3.1. At the FAIR facility, the primary beams generated at the present GSI accelerator facility will be used to feed the SIS100/300 synchrotron [27] which will

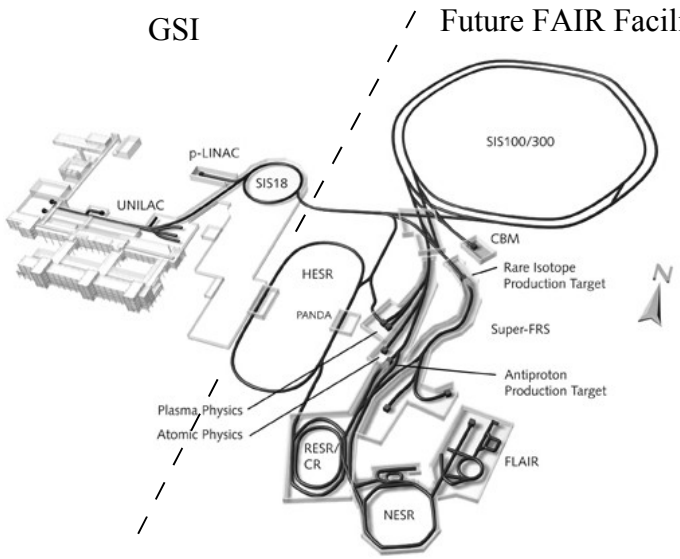


*Figure 3.1: Overview of the future FAIR facility [29].*

be used to accelerate protons or heavy ions to energies of tens of GeV. Proton beams will be sent to a target station for $\bar{p}$ production. The $\bar{p}$ beam is sent to the antiproton separator with the connecting transfer line to the collector ring (CR). The details of the antiproton production in the FAIR complex can be found in [30]. At CR [31] the stochastic pre-cooling of the antiproton (or rare isotope) beams will be done and then the antiprotons will be delivered to the High-Energy Storage Ring (HESR) [32] where they will be stacked in combination with stochastic cooling [33]. The HESR details are discussed in section 3.1.2. In the PANDA experiment, annihilation reactions of antiprotons with protons ($\bar{p}p$) and with nuclear matter ($\bar{p}A$) will be studied. The PANDA detector is located in the HESR ring. The cooled antiprotons from the HESR with momenta between 1.5 and 15 GeV/c will interact with either a pellet or a cluster-jet hydrogen target for $\bar{p}p$ annihilations and a cluster-jet or solid target of heavier nuclei ($N_2$, Ar, Cu etc.) for antiproton-nucleus reactions. The different target systems will be discussed in section 3.1.3.

### 3.1.1 The physics goals

Quark-gluon confinement, a Quantum Chromodynamics (QCD) phenomenon, has been one of the subjects of interest for several decades. The phenomenon is well described in the perturbative regime but in the non-perturbative regime a quantitative description is still lacking. Since at low energies, the strong coupling constant (the expansion parameter) becomes too large, the interaction of quarks with the gluon field cannot be treated perturbatively. The quark-gluon confinement in the non-perturbative regime can be studied by conducting an advanced meson spectroscopy and searching for predicted exotic hybrid states with explicit gluonic degrees of freedom. The PANDA experiment aims to achieve these physics goals. The PANDA physics program covers a wide range of topics summarized in Fig. 3.2. The vertical axis shows different physics topics, the top horizontal axis shows the antiproton beam momentum, and the horizontal axis at the bottom shows the corresponding mass of excited meson or baryon states. The different physics topics covered in the PANDA experiments are, e.g. $c\bar{c}$ meson ($J/\psi$, $\eta_c'$, $\chi_{cJ}$ (J = 0, 1, 2)) spectroscopy, search for exotic hadrons and glueballs ($ggg, gg$) and molecules ($qq\bar{q}\bar{q}$, $c\bar{c}q\bar{q}$) predicted by Lattice QCD (LQCD), open-charm states in

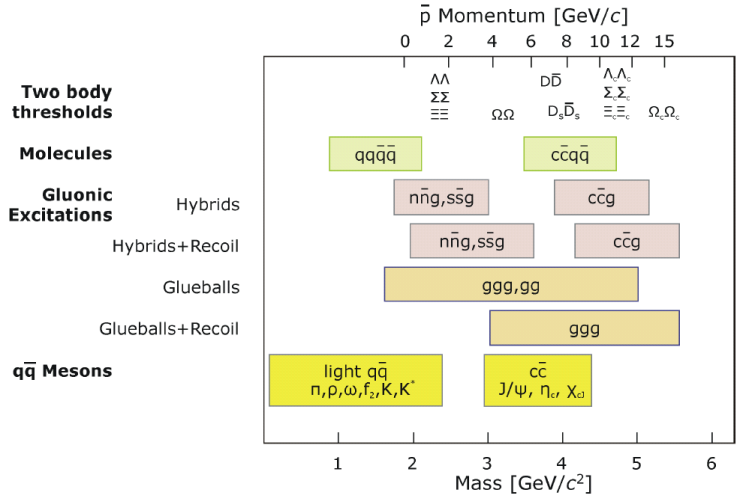


*Figure 3.2: Overview of the PANDA physics program concerning charm physics [34]. The further details are explained in the text.*

the $D$ meson ($D\bar{D}$) family, hypernuclear physics, and electromagnetic processes. Each one of them is briefly discussed in the following sections.

### Charmonium and open-charm spectroscopy

The Charmonium spectrum is shown in Fig. 3.3. In the spectrum, the low-lying states below the open-charm threshold (3.73 GeV) are arranged very similar to the positronium states. The strong-interaction potential contains two terms (eq. 2.4). The first term in the potential is Coulombic in nature, analogous to the Quantum Electrodynamics (QED) potential. The second term, called *confinement* term, guarantees that there are no free quarks in nature. For short distances, the Coulombic term is dominant. Thus the low-lying charmonium states resemble those of positronium, while the higher lying states may differ due to the confinement potential. In $e^+e^-$ annihilations only states with quantum numbers ($J^{PC} = 1^{--}$) can be formed directly because $e^+e^-$ annihilation primarily proceeds through an intermediate virtual photon, creating a bound $c\bar{c}$ state. The collaborations like BESIII [9], BELLE [36], and BABAR [37] have

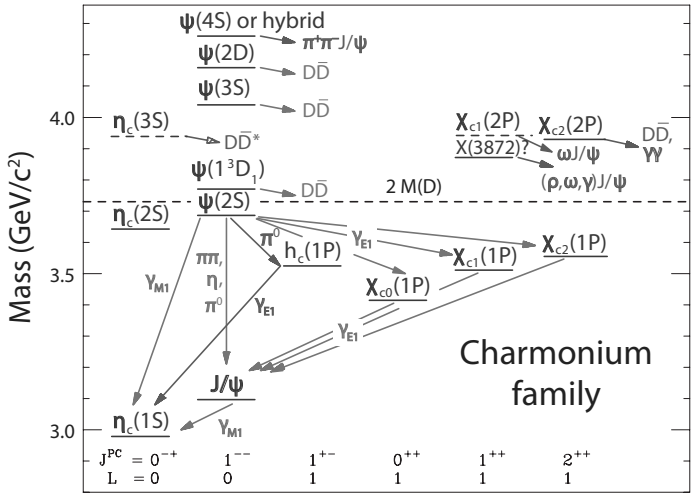


*Figure 3.3: Overview of the charmonium spectrum [35]. The vertical axis shows the Mass in* $\mathrm{GeV/c^2}$ *and the horizontal axis shows quantum numbers. The horizontal dashed line indicates the open-charm threshold.*

already produced such states using $e^+e^-$ annihilations. However, all other states are produced in the radiative decays of $J^{PC} = 1^{--}$ resonances. Therefore, the parameters of these other states (or resonances) are determined from the measurement of the recoil energy of the photon [8]. As a consequence, the precision in the measurement of the masses and widths of these states is limited by the detector resolution. In case of $\bar{p}p$ annihilation the three quarks in the proton annihilate with three antiquarks in the antiproton via intermediate states with an appropriate number of gluons and/or virtual $q\bar{q}$ pairs. Therefore, using $\bar{p}p$ annihilations, the charmonium states with all the quantum number can directly be produced. Also, the precise measurement of these states will be possible because in $\bar{p}p$ annihilations the initial state is known with high precision, being determined only by the parameters of the accelerator, and the final state is identified by the detector. Therefore, the precision in the measurement of mass and width of the charmonium states is determined by the precision in the measurement of the beam energy and its spread.

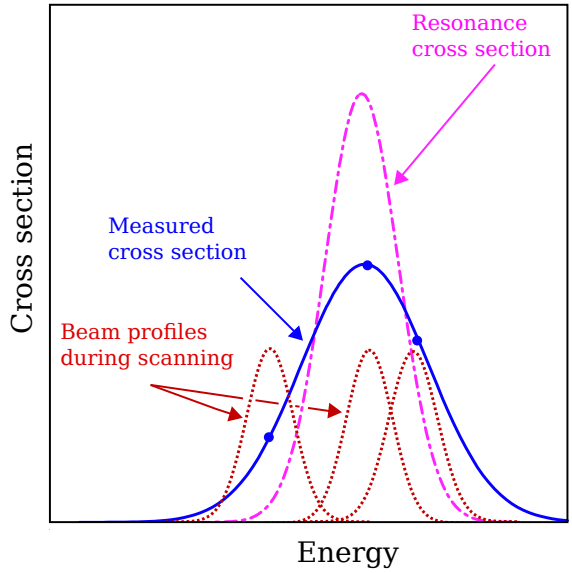


*Figure 3.4: Schematic of the resonance energy scan method [41]. The dotted (red) lines indicate the HESR center-of-mass energy distributions moving across the resonance. The (blue) dots are the observed cross sections at each energy distribution. The solid (blue) line is the excitation curve obtained using a convolution of the resonance curve and the beam profile. The dash-dotted (magenta) line shows the deconvoluted resonance cross section.*

To achieve these high precision[1] measurements, the PANDA experiment will use the resonance energy scan method schematically shown in Fig. 3.4 [6, 41, 42]. The energy of interaction obtained from the beam parameters is shown on the horizontal axis. The interaction energy can be varied in the energy region of interest to explore the charmonium resonances. The vertical axis shows the cross section for each energy distribution. Using the PANDA detector, the number of events observed at each energy point can be used to estimate the cross section. Therefore, using this technique, the mass and the width of the charmonium state can be measured with accuracies of the order of 10 keV to 100 keV. Hence using

[1]For example, the full width of the charmonium state $h_c(1P)$ reported in PDG [38] is $\Gamma(h_c(1P)) < 1$ MeV and the width recently measured by the BESIII collaboration is $\Gamma(h_c(1P)) = 0.73 \pm 0.45$ (stat.) $\pm$ 0.28 (syst.) MeV [39]. In case of the PANDA experiment, the simulated $h_c(1P)$ resonance shape yields a width of $\Gamma(h_c(1P)) = 0.5 \pm 0.14$ MeV, assuming 5 days of data taking per point in high-resolution mode [40] of the HESR.

this powerful method it will be possible to measure precisely the charmonium states below and above the open-charm threshold.

In this context, the PANDA experiment plays a very important role in measuring states with quantum numbers other than $(1^{--})$ with high precision. For example, recently in $e^+e^-$ annihilations at BESIII the mass and width of the lowest-lying charmonium state, the $\eta_c(1S)$ were measured via $\psi'(3686) \to \gamma\eta_c$ [43]. In case of PANDA, by performing $\bar{p}p$ annihilations, the $\eta_c(1S)$ state can be directly formed, which will improve the precision in mass and width measurements. Similarly, other states like $\eta_c'$, $h_c$, $\chi_{cJ}$ $(J = 0, 1, 2)$ and many other theoretically predicted resonances will be precisely measured. Moreover, most of the states above the open-charm threshold are either completely unknown or some have been observed (e.g. X(3872)) but need to be studied further to understand their nature [41]. The HESR running in High Luminosity (HL) mode at $\bar{p}$ momentum of 6.4 GeV/c will produce a large number of $D$ meson pairs. This high-statistics data set will allow a precision study of the $D$ and $D_s$ meson spectrum.

**Gluonic excitations: Hybrids and Glueballs**

The gluonic excitations fall into two main parts, namely hybrids and glueballs. Hadrons are described as bound states of quarks which interact through color forces mediated by gluons. Due to this color charge gluons are subject to self-coupling and can be constituents of hadronic matter. These self-coupled quarkless states are called glueballs. Glueballs can be formed by the coupling of two or more gluons. Hybrids are $\bar{q}q$ states with an additional constituent gluon. According to LQCD calculations [19, 44] glueballs and hybrids lie in the same mass region as ordinary $(\bar{q}q)$ states, which makes their experimental identification difficult. Since glueballs do not emerge from the quark model, a complete understanding of the conventional meson spectroscopy is necessary to distinguish exotic states from the conventional $(\bar{q}q)$ mesons. Therefore, in the PANDA experiment the $\bar{p}p$ annihilations provide the gluon-rich environment to validate the glueball mass spectrum predicted by LQCD (see Fig. 2.2) [19].

### Hypernuclear physics

Hypernuclei are nuclear systems in which one or more nucleons are replaced by one or more hyperons and a new quantum number *strangeness* is introduced into the nucleus. The hyperon is a baryon containing one or more strange quarks. At present only single-$\Lambda$ hypernuclei have been observed close to the valley of stability in the nuclear chart and only six double-$\Lambda$ hypernuclei have been detected [45, 46]. By performing hypernuclear spectroscopy it is possible to study the hyperon-nucleon and the hyperon-hyperon interactions. Also the production of the famous six-quark object ($uuddss$) H-dibaryon [47, 48] is possible.

In the PANDA experiment, hypernuclei will be produced using unique $\bar{p}A$ interactions, in which the antiproton beam will interact with a primary solid target of Carbon (C) to produce a large number of $\Xi\bar{\Xi}$ pairs. Some of the $\Xi$ will be so slow that they will be absorbed in a secondary target which is a sandwich structure of silicon micro strip detectors and absorbing material ($^{9}$Be, $^{10}$B or $^{11}$B, or $^{12}$C or $^{13}$C). The double-$\Lambda$ hypernuclei will be formed by a nuclear reaction: $\Xi^{-}p \rightarrow \Lambda\Lambda + 28$ MeV in the secondary target. The weak decay cascade will be studied by tracking using the silicon micro-strip detectors and the gamma decay scheme will be measured using high-precision Germanium detectors.

### Electromagnetic processes

In addition to the physics program discussed above, the PANDA experiment will be able to investigate the nucleon structure using electromagnetic processes to measure Deep Virtual Compton Scattering (DVCS), Electromagnetic Form Factors (EFF) of the protons, or Drell-Yan (DY) pair production. In the DVCS process, the two-photon final state $\bar{p}p \rightarrow \gamma\gamma$ can be measured using the advanced PANDA Electromagnetic Calorimeter (EMC). The EFFs of the proton in the time-like domain can be measured using the $\bar{p}p \rightarrow e^{+}e^{-}$ process. In DY pair production two polarized or unpolarized hadrons annihilate into a lepton ($l^{+}l^{-}$) pair. In the PANDA experiment only the unpolarized DY process is possible since the target will be unpolarized. However, studies are ongoing for a polarized proton target and antiproton beam [49, 50].

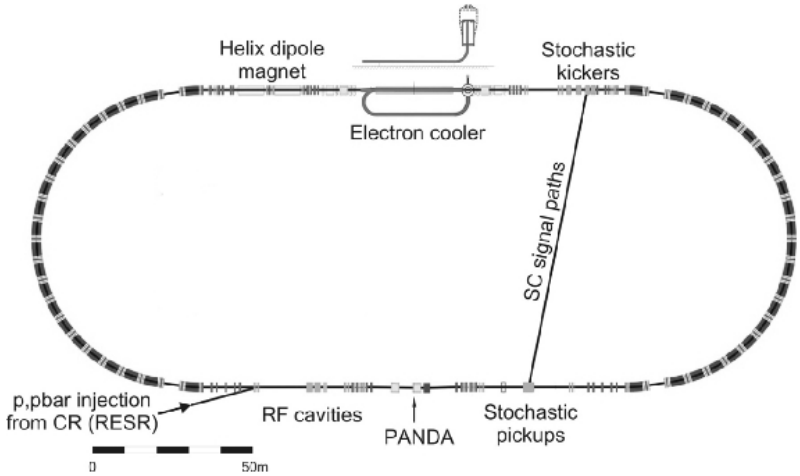


*Figure 3.5: Overview of the High Energy Storage Ring [12]. The antiproton or heavy ion beam will enter from the left side and will be directed towards the PANDA detector for $\bar{p}$ annihilation. The location of the PANDA detector is indicated by an arrow.*

### 3.1.2 High Energy Storage Ring - HESR

The HESR has been specially designed for the PANDA experiment. It will be used to store and cool antiproton beams accumulated in the CR/RESR ring system. The RESR is an accumulator and decelerator ring designed for the accumulation of high intensity antiproton beams and the deceleration of rare isotope beams. The HESR is designed as a race-track shaped ring as shown in Fig. 3.5. The HESR has two straight sections: the upper section will be used for complementary electron cooling in combination with stochastic cooling via several kickers and opposing high-sensitivity pick-ups located at the lower straight section of the ring. By combining both beam cooling systems, the relative momentum spread can be further improved. The lower straight section will accommodate the PANDA detector. The antiproton beam with momenta between 1.5 and 15 GeV/c will enter the HESR from the left side. The mean beam lifetime in the HESR ranges between 1540 s and 7100 s [12]. The HESR can be operated in High Luminosity (HL) as well as in High Resolution (HR) mode. The operational parameters for both the HR and HL modes are shown in Table 3.1 [51]. The most

| Operational parameters | | | | |
|---|---|---|---|---|
| **HESR mode** | $\bar{p}$ momentum (GeV/c) | RMS momentum spread ($\sigma_p/p$) | Peak Luminosity ($cm^{-2}$ $s^{-1}$) | stored $\bar{p}$ |
| HR | 1.5 to 8.9 | $4 \cdot 10^{-5}$ | $2 \cdot 10^{31}$ | $10^{10}$ |
| HL | 1.5 to 15 | $10^{-4}$ | $2 \cdot 10^{32}$ | $10^{11}$ |

*Table 3.1: The HESR operational parameters at target density of* $4 \cdot 10^{15}$ atoms/$cm^2$ *for the High Resolution (HR) and High Luminosity (HL) mode.*

important antiproton beam parameters required for the PANDA experiment are the number of stored antiprotons ($\geq 10^{10}$ $\bar{p}$), and beam momentum between 1.5 GeV/c to 15 GeV/c with RMS momentum spread ($\sigma_p/p$) $\leq 10^{-4}$. The HESR parameters easily meet the antiproton beam requirements for the PANDA experiment.

### 3.1.3 Targets

To study the different physics topics discussed above, the PANDA experiment will use both gaseous and non-gaseous targets. To achieve a high effective target density of $10^{15}$ atoms/$cm^2$, a fine tuning of the target size and thickness is very important. Presently the development and testing of two different target systems, namely the Cluster-jet target and the Pellet target system is, in progress. In interactions with high-energy cooled antiprotons stored in the HESR both target systems are capable of meeting the PANDA requirements [51].

In the cluster-jet target, pressurized cold hydrogen gas expands into the vacuum through a nozzle and the ejected gas condenses to form a narrow jet of hydrogen clusters. Using the cluster-jet target a homogeneous target density profile can be achieved. The Interaction Point (IP) is thus defined transversely but has to be reconstructed longitudinally in the beam direction. However, the lateral spread of the cluster jet leads to an uncertainty in the IP definition along the beam axis.

The pellet target provides a stream of frozen hydrogen micro-spheres named pellets. High target densities can be achieved using the pellet target but it has

a non-uniform time distribution which causes variations in the luminosity [51, 52]. The simulation studies of luminosity variations are reported in Ref. [53, 54]. The maximum achievable average luminosity is very sensitive to the deviations of individual pellets from the target axis. Moreover, the luminosity is directly proportional to the number of antiprotons in the HESR. The theoretical upper limit of the maximum average luminosity is close to $3 \cdot 10^{32}$ cm$^{-2}$ s$^{-1}$ [51], if the number of antiprotons is not restricted. Under realistic conditions the number of antiprotons is restricted due to the Coulomb repulsion. In the HL mode of the HESR, at 15 GeV/c $\bar{p}$ beam momentum with $10^{11}$ antiprotons, average luminosities up to $1.6 \cdot 10^{32}$ cm$^{-2}$ s$^{-1}$ will be reached The PANDA experiment aims at an average $\bar{p}p$ annihilation rate of 20 MHz. However, target density fluctuations may lead to a peak annihilation rate up to 40 MHz for time durations of 15 ms, when the pellet array will cross the antiproton beam [54]. At such high rate the forward endcap EMC will be exposed to a peak hit rate of 1 MHz causing pile-up of detector pulses. The pulse pile-up recovery method and its performance test are described in chapter 5.

Improvements in both the target systems are in progress. The targets will be connected to their source placed above the PANDA detector, and to a target dump below the PANDA detector by a thin pipe going vertically through the whole PANDA detector (Fig. 3.6). To perform antiproton-nucleus ($\bar{p}$A) reactions the antiproton beam will collide with solid targets (Cu, Au etc.) or gaseous targets ($N_2$, Ar etc.). For hypernuclei production combined targets such as Au + $^{12}$C will be used.

## 3.2 The PANDA detector

The PANDA detector has been designed to study a wide range of physics topics discussed in the previous section. The design requirements of the experiment are: almost $4\pi$ coverage of the detector, a large dynamic range for the momentum measurement, and high resolution for tracking, time-of-flight, calorimeter, and muon counters. PANDA is a fixed-target experiment where an antiproton beam with momentum between 1.5 to 15 GeV/c will interact with a proton or nuclear target. The interaction rate will be about $2 \cdot 10^7$ events/s causing high hit rates

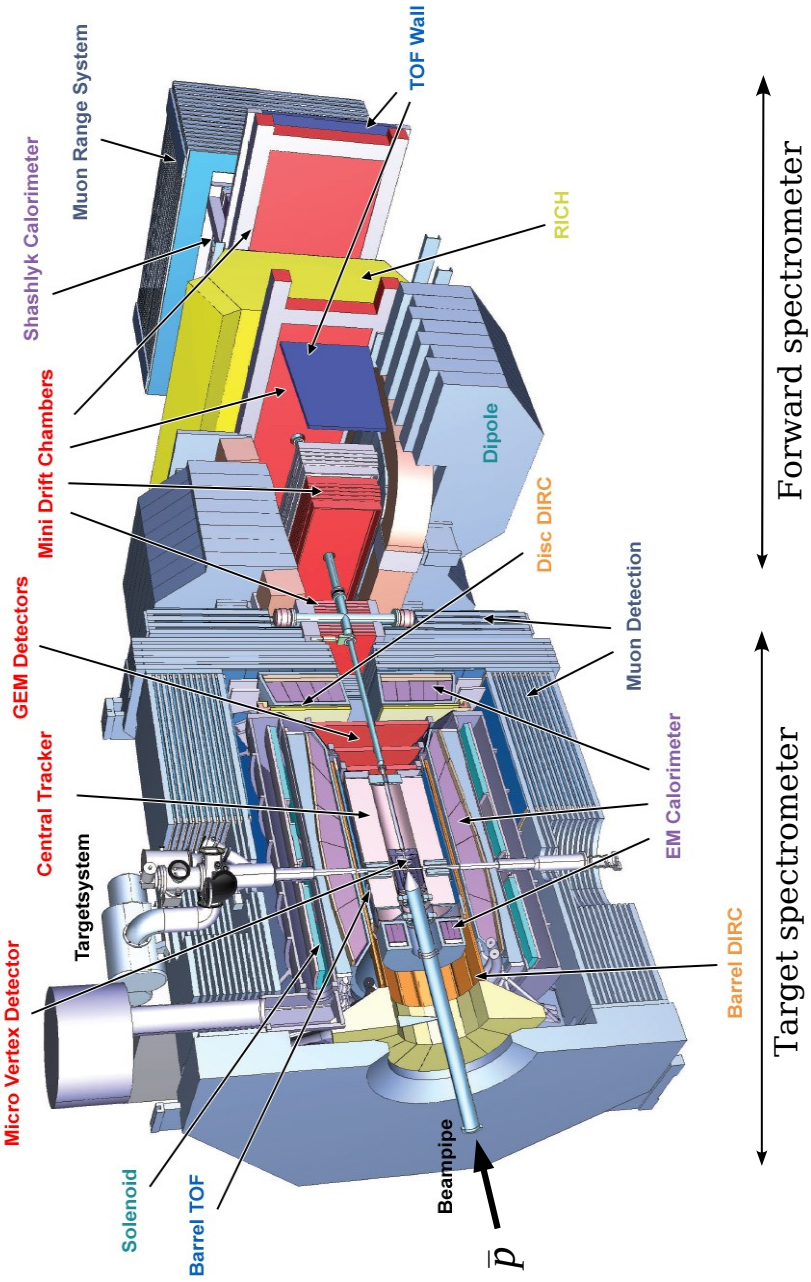


*Figure 3.6: Overview of the PANDA detector [55].*

at the PANDA detector. Therefore, the PANDA detector should be capable to work in a high detector hit-rate environment. The readout and the event selection criteria should be very much advanced to perform efficiently in real-time during the operation of the detector. The interaction of antiprotons of high beam momentum with a fixed target will result in a forward boost. Therefore, the PANDA detector is designed in two parts, namely the target spectrometer with a solenoid magnetic field and the forward spectrometer with a dipole magnetic field. The overview of the PANDA detector consisting of both the target and the forward spectrometer is shown in Fig. 3.6.

### 3.2.1 Target spectrometer

The target spectrometer is rather symmetric and provides almost $4\pi$ coverage. The spectrometer surrounds the IP defined by the crossing of antiproton beam and the target. To reduce cost, the size of the whole spectrometer is kept as small as possible. The spectrometer is designed in three parts: the barrel to cover polar angles from 22° to 140°, the forward endcap to cover 5° to 22°, and the backward endcap to cover 145° to 170°. The spectrometer consists of a solenoid magnet, the target system (see section 3.1.3), different detection systems such as Micro Vertex Detector, Straw-Tube Tracker, Time-Of-Flight, Detection of Internally Reflected Cherenkov radiation, Electromagnetic Calorimeter, and Muon filters. All these components are discussed briefly in the following sections.

#### Solenoid magnet

The solenoid magnet provides a rather homogeneous magnetic field of 2 T and is designed to perform charged-particle tracking. The field will be achieved by building a solenoid with a superconducting coil of 2.8 m length and with 105 cm inner radius, using a laminated iron yoke for the flux return. The solenoid coil will be placed outside the EMC to avoid dead material in front of the calorimeter and other inner detectors. The cryostat for the superconducting coils has two warm bores of 100 mm, one placed above and one below the target position. The details of the PANDA magnet system are documented in Ref. [56].

### Micro Vertex Detector

The Micro Vertex Detector (MVD) is the innermost tracking detector of PANDA. The MVD will be mounted very close to the IP to achieve maximum possible acceptance. The MVD is designed to improve the transverse momentum resolution and to obtain energy loss information of slow protons, kaons, and pions for Particle Identification (PID). In particular the identification of kaons will enhance the efficiency for $D$ mesons which have large branching ratios for channels accompanied by kaons. The MVD will play a crucial role in secondary vertex detection from open-charm physics and hyperon decays. The track information from the MVD will be used as input to the event reconstruction. The MVD makes use of radiation-hard silicon pixel detectors with fast individual pixel readout and silicon strip detectors. More details about this detector can be found in Ref. [52].

### Straw-Tube Tracker

The Straw-Tube Tracker (STT) is the central tracking detector designed for the tracking of charged particles inside the solenoid field of the target spectrometer. The STT is designed to operate in a high-rate environment because it will be placed very close to the interaction point, surrounding the MVD. The straws are gas-filled (mixture of Ar + 10%$CO_2$) cylindrical tubes with a conductive inner layer as cathode and an anode wire stretched along the cylinder axis. A high electric field applied between these two electrodes separates electrons and positive ions produced by a charged particle along its trajectory through the volume of the gas. The energy loss of the charged particle measured in the straw gas volume can be exploited for PID. The STT has a high tracking efficiency and a high spatial resolution (less than 150 $\mu$m) depending on the tube diameter and the gas characteristics. The STT will cover polar angles from 22° to 140°. The particles emitted below the polar angle of 22° will be covered using gaseous micro-pattern detectors based on Gas Electron Multiplier (GEM) foils. More details of the STT and GEM detectors are reported in Ref. [57].

### Detection of Internally Reflected Cherenkov radiation

The DIRC will be designed into two parts, the Barrel DIRC to cover polar angles from 22° to 140° and the forward endcap DIRC to cover the range from 5° to 22° in polar angle. The DIRC is designed for PID of relativistic charged particles. The DIRC will be built using 1.7 cm thick fused silica (artificial quartz) slabs which will detect internally reflected Cherenkov light. The readout will be done using Mirco-Channel Plate Photo-Multiplier Tubes (MCP PMTs). They are insensitive to the magnetic field. The endcap DIRC will be a silica disk of 2 cm thickness and 110 cm radius placed in front of the forward endcap EMC.

### Time-Of-Flight

The Time-Of-Flight (TOF) detector is designed for PID of slow particles at large polar angles. The design concept of the TOF is based on scintillator tiles ($28.5 \times 28.5$ mm$^2$) with a readout using two Silicon Photo-Multiplier (SiPM) coupled to each tile [58]. The TOF will be surrounding the DIRC detector where it can also be used to detect conversion photons from the DIRC radiator. The time resolution of 100 ps is expected to meet the PANDA requirement of fast event selection and event building.

### Electromagnetic Calorimeter

The PANDA Electromagnetic Calorimeter (EMC) is designed to measure energy, time, and position of photons and electrons over a large dynamic energy range from a few MeV upto 15 GeV. A precise determination of the opening angle between two photons is required for the invariant-mass reconstruction, which can be achieved by a calorimeter with fine granularity. Therefore, for the PANDA EMC high density lead-tungstate ($PbWO_4$ or PWO) inorganic scintillating crystals are chosen. PWO crystals are being used for the EMC of the CMS [59] and ALICE [60] detectors operating in the LHC [61] at CERN [62]. To achieve a wide dynamic energy range which includes low-energy photon detection, in PANDA the PWO crystals will be cooled to $-25$°C to increase the light yield almost four times above the yield at room temperature. The EMC will be built from almost 16,000 PWO crystals coupled to either Avalanche PhotoDiode (APD) or Vacuum

Photo-Tetrode (VPTT) photosensors. Different EMC prototypes have been built and successfully tested with tagged high-energy photons [63,64]. An energy resolution of about 2.5% at a photon energy of 1.4 GeV and a time resolution of less than 1 ns were achieved with a prototype of sixty PWO crystals [64]. To achieve almost $4\pi$ coverage, the EMC is designed in three different parts. The details of the PANDA EMC are documented in its Technical Design Report (TDR) [12].

#### Muon detectors

The muon detectors are designed to detect muons originating from the decay of charmonium states (e.g. $J/\psi$), semi-leptonic $D$-meson decays, and the DY process. The DY muon pairs will be used to optimize the muon system because these muon pairs have maximal momentum spread which covers the other processes of interest with muons in their final state. These processes of interest with muons in their final state have small cross sections compared to the muons coming from the decay of pions or kaons. Therefore, the muon identification has to be very efficient in obtaining a high signal to background ratio. To meet this requirement, a range-tracking system will be implemented in the yoke of the solenoid magnet. To this end, the yoke is split in a number of segments and tracking detectors are placed between those segments. Such a system will allow to discriminate the energy losses of muons and pions. Aluminum drift tubes similar to the ones in the muon detection system of the COMPASS experiments [65] will be used as tracking detectors which will be placed between the segments.

### 3.2.2 Forward spectrometer

PANDA is a fixed-target experiment where most of the particles will travel in the forward direction. The forward spectrometer shown in Fig. 3.6 will be used to detect these particles. The magnetic field of a dipole magnet will be used to perform charged-particle tracking employing Mini Drift Chambers (MDC). The expected RMS momentum resolution ($\delta p/p$) of the tracking system at 3 GeV protons is 2% [6]. To achieve good PID, the TOF wall with expected time resolution of 50 ns and RICH detectors as those in the HERMES detector [66,67] will be used. The energy of photons and electrons will be measured using a

Shashlyk calorimeter [68]. In the muon detectors, the range tracking system will be used for the muon detection, which allows discrimination of pions from muons. Further details of the forward spectrometer are reported in Ref. [69].

### 3.2.3 Trigger and data acquisition

The trigger and Data Acquisition (DAQ) system of the PANDA experiment is very challenging because of the high interaction rate and a wide physics program. The various topics mentioned in the physics program require different event selection criteria where different sub-detectors will contribute in the event selection process. The readout of each detector needs to be done in parallel wherever possible to maximize the physics yield. To achieve this goal, the traditional approach of a hierarchical hardware trigger has to be abandoned. Therefore, the PANDA experiment will use a new approach, where all the sub-detector channels will be self-triggered. The schematic of the PANDA Data Acquisition (DAQ) system is shown in Fig. 3.7. The front-end electronics of each subsystem will process data on-line in Field Programmable Gate Arrays (FPGAs) and transmit the relevant hit information to the next level in the DAQ. The data coming from these different subsystems will be synchronized by distributing a precise common clock to the front-end modules from which the time tag for every hit is derived. The data belonging to a certain period of time are grouped in a block and one block is called an event. For the time synchronization a specially developed time distribution system named SynchrOnization of Data Acquisition (SODA) [70] will be used. The event selection will be done in the Compute Node (CN) [71] using on-line high level trigger algorithms [72]. To provide the link for all building blocks, a high-bandwidth network fabric will be used. Based on such an approach a prototype of the hardware-trigger-less system has been developed and successfully tested with prototypes of the PANDA EMC [73]. The performance results of the PANDA EMC prototype readout chain will be discussed in chapter 6.

### 3.2.4 Data analysis software - PandaROOT

PandaROOT [74] is the Monte Carlo (MC) simulation, reconstruction, and analysis software framework specially developed for the PANDA experiment. Panda-

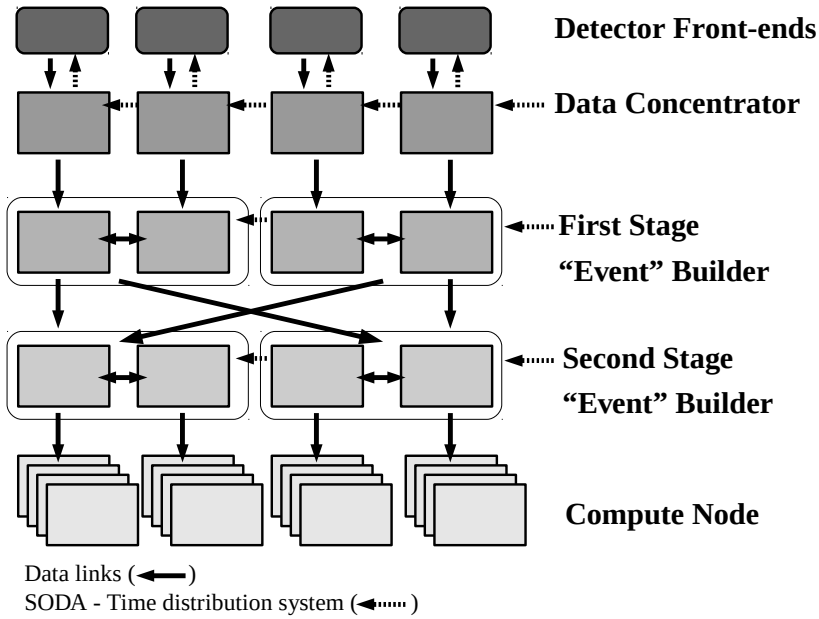


*Figure 3.7: Schematic representation of the PANDA Data Acquisition (DAQ) system as suggested in Ref. [70].*

ROOT is a very flexible, fast, and robust software package based on an object-oriented approach. Most of the software is developed using the C++ programming language. The core services for the detector simulation and the offline analysis are provided by the FairROOT framework [75] which is based on the object-oriented data analysis framework ROOT [76] and the Virtual Monte Carlo (VMC) interface [77]. The detector geometry can be defined in Geant4 [78] or in ROOT format. The Geant3 or Geant4 software package is used as transport engines for the simulation of physical processes such as the energy loss and multiple scattering inside the detector volumes. The digitization and reconstruction (track, EMC shower energy etc.) algorithms are successfully implemented and tested and further improvement is in progress. More details about the software and its physics performance are given in Ref. [6]. In this thesis for the pile-up simulation studies (chapter 5), the photon energy distribution for the forward endcap EMC is simulated using PandaROOT.

## 3.3 The BESIII experiment

BESIII (Beijing Electron Spectrometer) is an $e^+e^-$ annihilation experiment [79, 80] running in the Beijing Electron Positron Collider (BEPC)-II [81] at the Institute of High Energy Physics (IHEP), Beijing. The BEPC-I as well as BES detector were upgraded (in the years 2003 to 2008) to the current BEPCII collider and the BESIII experiment which is successfully taking data since August 2008. The BEPC-I was a single-ring $e^+e^-$ collider, while the new BEPC-II is a double-ring multi-bunch collider with improved luminosity of $1 \cdot 10^{33}\text{cm}^{-2}\text{s}^{-1}$ and a factor 100 higher center-of-mass energy reaching $2 \cdot 2.3$ GeV. The physics program of BESIII covers different topics such as charmonium spectroscopy, light hadron spectroscopy, charm physics, and $\tau$ physics. These physics goals are briefly discussed in section 3.3.1. The BESIII detector is equipped with advanced detector systems to perform tracking, PID, calorimetry, and muon detection. All these detectors are briefly discussed in section 3.3.2. The trigger, data acquisition, and the offline analysis software are discussed in sections 3.3.3 and 3.3.4, respectively.

### 3.3.1 The physics program of BESIII

Although the BESIII experiment is an $e^+e^-$ annihilation experiment, its physics program is similar in some aspects to the physics program planned with the PANDA experiments. BESIII covers physics topics within the center-of-mass energy range up to 4.6 GeV [82] including a high statistics study of charmonium and light hadron spectroscopy, $D$-meson and $\tau$ lepton physics. In charmonium spectroscopy the states like $J/\psi(1S)$, $\psi(2S)$ and $\psi(3770)$ have been measured using the world's largest data set collected during the past couple of years. The states like X(3872), Y(4260) will also be measured soon. The light hadron spectroscopy will be performed by studying various $J/\psi$ decay modes. This spectroscopy includes searches of glueballs and exotic mesons and also of new resonance states decaying from $J/\psi$ in the mass region of 2.5 GeV. To measure the $D - \bar{D}$ mixing and search for $CP$-violation [83, 84], $\bar{D}D$, $D^0\bar{D}^0$, $D^+D^-$ pairs will be produced through decays of $\psi(3770)$. The state $\psi(3770)$ has high branching fractions for decays to D-meson pairs. At the production threshold of 3.55 GeV the $\tau$ leptons can be produced. The $\tau$ is the only known massive ($\sim 1.77$ GeV/c$^2$) lepton which

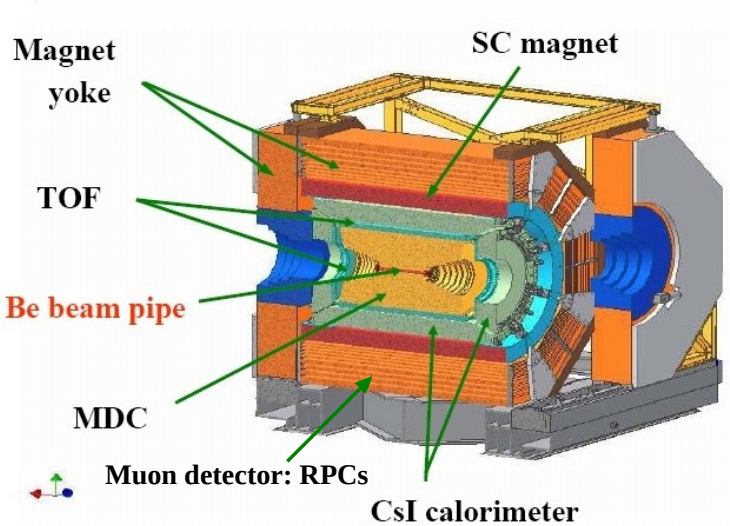


*Figure 3.8: Overview of the BESIII detector [79].*

decays to hadrons. Therefore, the various $\tau$ decays, such as hadronic, leptonic, and semi-leptonic $\tau$ decays, will be studied. The detailed physics program of the BESIII experiment is documented in the dedicated physics book published by the BESIII collaboration [7].

### 3.3.2 The BESIII detector

The scheme of the BESIII detector is shown in Fig. 3.8. The detector mainly consists of four sub-detector systems, namely the Multilayer Drift Chamber (MDC) surrounding the beam pipe close to the interaction point, the Time-Of-Flight (TOF) system built from two layers of plastic scintillators placed around the MDC. The Electromagnetic Calorimeter (EMC) is built from almost six thousand CsI(Tl) crystals surrounding the TOF. These three detector elements are placed inside a 1 T superconducting solenoid magnet. The Muon Detector (MD) uses Resistive Plate Chambers (RPCs) which are inserted in gaps inside the magnet yoke. In this way, the spectrometer covers almost $4\pi$ solid angle and a polar angle range $21^\circ < \theta < 159^\circ$. The detector parameters obtained after successful

| Subsystem parameters | Values |
|---|---|
| **MDC** | |
| **Resolution** | |
| Position: Single wire $\sigma_{r\phi}$ | 130 $\mu$m |
| Momentum $\sigma_p/p$ at 1 GeV/C | 0.5% |
| $\sigma(dE/dX)$ | 6% |
| **TOF** | |
| **Time resolution** $\sigma_T$ | |
| Barrel | 100 ps |
| Endcap | 110 ps |
| **EMC** | |
| **Resolution at 1 GeV** | |
| Energy $\sigma_E/E$ | 2.5% |
| Position $\sigma_{x,y}$ | 0.6 cm |
| **MD** | |
| Cut-off momentum | 0.4 GeV/c |

*Table 3.2: The list of the operation parameters of the BESIII detector subsystem [79].*

performance are listed in Table 3.2. The technical details of the BESIII detector can be found in Ref. [79, 80].

### 3.3.3 Trigger and data acquisition

The BESIII trigger and data acquisition system is designed to operate with multi-beam bunches separated by 8 ns and with a data rate of $\sim$ 40 MB/s. The trigger system is divided into two parts, the Level 1 (L1) hardware trigger and the Level 3 (L3) software trigger. The sub-trigger signals generated by TOF, MDC, and EMC are processed by an appropriate trigger logic near the detector to obtain basic triggers such as track count in the MDC, hit count in the TOF, and cluster count in the EMC. This basic trigger information from the sub-systems is time correlated using Global Trigger Logic (GTL). The GTL generates the L1 trigger whenever a valid trigger condition is satisfied. The GTL is implemented in FPGA from where the signals are transported by optical links. The L1 trigger system operates at 41 MHz clock frequency synchronized with the radio frequency (RF) of

the accelerator. The readout electronics uses this trigger clock to synchronize the entire BESIII operation. In this way, the L1 trigger system makes the selection of physics events with trigger efficiencies higher than 98% [85]. The maximum rate expected at the L1 trigger level is about 4 kHz at a center-of-mass energy of 3.1 GeV.

The L3 trigger is a software trigger including event building and filtering. In the event builder, the fragments belonging to the same L1 trigger from different detectors are assembled to build an event. These events are processed in the event filter (L3 trigger) using the event selection algorithms [86]. These filtered events are further stored in the event storage subsystem. The BESIII event filters are based on the ATLAS event filter framework [87] with some modifications applied to meet the BESIII physics requirements. After the L3 trigger, the trigger rate is reduced from 4 kHz to 1 kHz.

### 3.3.4 BESIII Offline Software System - BOSS

The BESIII Offline Software System (BOSS) [88] is developed for the offline MC simulations. A part of it is used for experimental data analysis. BOSS is based on the Gaudi framework [89] for providing the necessary interfaces and services for building High Energy Physics (HEP) experiment frameworks for event-data processing applications. The BOSS software uses some external HEP libraries such as CERNLIB [90], CLHEP [91], ROOT [76], and Geant4 [78]. The detector geometries are created using Geant4. The calibration software is based on GLAST's scheme [92], which consists of a calibration framework and calibration algorithms. The reconstruction of physics events from measured data is a very important step. To perform this step reliably in the offline software, a complete chain of reconstruction algorithms has been implemented in the reconstruction part of the BOSS software. This chain consists of important algorithms like the charged-particle tracking for MDC, $dE/dX$ and TOF reconstruction, EMC shower energy and position reconstruction, and muon track finding for the MD. This reconstructed information is used to perform PID, vertex finding and fitting, and kinematic fitting required for the physics analysis. The charmonium electromagnetic transition studies were performed using the BOSS software and are reported in chapter 7.

# Chapter 4

# PANDA Electromagnetic Calorimeter

In nuclear and particle physics, the electromagnetic and hadron calorimeters are used to measure energy and position of photons, electrons and charged as well as neutral hadrons. Calorimeters are blocks of radiation sensitive material in which particles lose their energy by creating a shower of secondary particles which can be measured in the form of charge or light created in an active medium. There are two types of calorimeter techniques: homogeneous and sampling calorimetry.

Homogeneous calorimeters are built from a homogenous active medium of scintillating or Cherenkov material. These calorimeters provide a very good energy resolution because the full energy of an incident particle gets absorbed in the active material. Since the scintillating material is relatively expensive, the calorimeter design is usually compact. Due to this constraint the homogeneous calorimeters are generally used for electromagnetic showers.

In the design of the sampling calorimeters, passive absorber layers (iron, lead, copper) are used to sandwich the active layers of gaseous, liquid or solid material. Due to the sampling fluctuations caused by the absorber layers, the energy resolution of the sampling calorimeter is worse than that of homogeneous calorimeters. The sampling calorimeter provides a good position resolution. These types of

calorimeters are relatively cheap, can be built in large volumes and are easy to segment. Therefore, they are generally used for hadronic showers, where larger stopping powers are required.

This chapter is dedicated to the PANDA EMC based on the homogeneous calorimetry technique. The EMC is a scintillator calorimeter which will be built from $PbWO_4$ crystals. In section 4.1, the general principles such as photon and electron interaction with matter, radiation length, electromagnetic shower and energy resolution are discussed. In section 4.2, the EMC physics requirements, its design criteria, and the associated front-end electronics are described. The EMC readout chain is discussed in section 4.3.

## 4.1 General principles

### 4.1.1 Electron and photon interaction with matter

#### Electrons

Electrons (and positrons) lose their energy while interacting with matter via two main processes: ionization or excitation of an atom with atomic number $Z$, and Bremsstrahlung radiation. The electron ionizes an atom by knocking out an outer-shell electron. This process is dominant for low-energy electrons. The energy loss via Bremsstrahlung occurs when the high-energy electron gets deflected in the electric field of the atomic nucleus. Bremsstrahlung is dominant for high-energy electrons. The total energy loss of electrons or positrons, therefore, is the sum of energy losses by excitation and ionization and by the Bremsstrahlung process. The energy at which these two processes are equal, is called the *Critical energy* $E_c$ [38] and can be expressed by equation 4.1:

$$E_c = \frac{600 \text{ MeV}}{Z + 1.2}. \tag{4.1}$$

In the region above the critical energy, Bremsstrahlung dominates completely. As an example, the electron energy loss in lead ($Z = 82$) as a function of electron energy is shown in Fig. 4.1 (a). For lead $E_c \approx 7$ MeV. In the region well below $E_c$ the process of excitation and ionization dominates although other processes

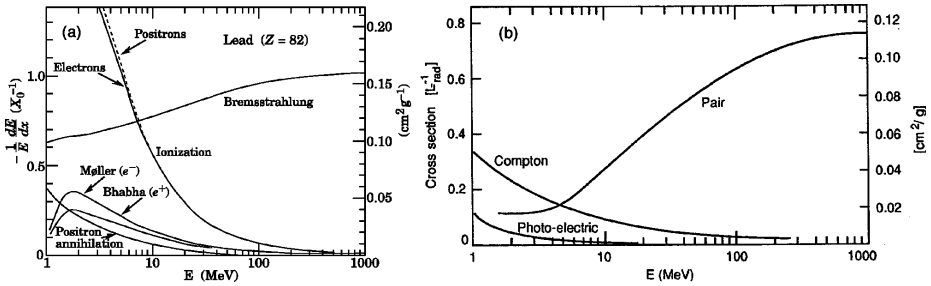


*Figure 4.1: (a) Energy loss of an electron in lead as a function of energy [38]. (b) Photon interaction cross section in lead as a function of energy [93].*

(M$\phi$ller scattering, Bhabha scattering, $e^+$ annihilation) contribute in the electron energy loss.

### Photons

Photons are the quanta of electromagnetic radiation and, since they are electrically neutral, their interaction with matter is very different in comparison with charged particles. They do not lose energy via inelastic collisions. The photon interaction with matter can be mainly characterized by three processes, namely *Photoelectric effect, Compton scattering*, and *Pair production*. The occurrence of these processes depends on the photon energy and the type of matter with which they are interacting.

In the photoelectric effect, an atom absorbs a photon and emits an inner-shell electron. The created vacancy is filled by one of the outer-shell electrons, whose transition is accompanied by the emission of Auger electrons or X-rays. The energy of an emitted photo-electron is equal to the difference between the energy of the photon and the binding energy of the electron. The photoelectric effect occurs when the energy of an incident photon is larger than the binding energy of the electron. The photoelectric effect is dominant in the low-energy region of 1-100 keV. The cross section for this process is proportional to the atomic number $Z$.

In Compton scattering, a photon collides with a weakly bound electron and scatters while suffering some energy loss. Compton scattering is dominant in

the energy region of 100 keV-1 MeV. The probability of Compton scattering is proportional to the number of electrons in the atom and inversely proportional to the photon energy.

In the pair-production process, a photon is converted into an electron-positron pair. A pair production can only occur if the photon energy is higher than twice the rest energy of an electron: $2\ m_e c^2 = 1.022$ MeV. The pair production cross section increases with increasing photon energy and the atomic number $Z$.

The photon interaction cross section for lead as a function of photon energy is shown in Fig. 4.1 (b). The cross sections for the photoelectric and the Compton process decrease while for the pair production process it increases with increasing photon energy. The mean free path $\lambda$, i.e. the average distance traveled by a photon whithout interacting with matter, is given by $1/\mu$, where $\mu$ is an attenuation coefficient defined as $\mu = N\sigma_t$. $N$ is the number of atoms or nuclei in the interacting material and $\sigma_t$ is the total cross section for the photon interaction with matter.

### 4.1.2 Radiation length

The radiation length $X_0$ is defined as the distance required to reduce the electron energy by a factor 1/e via Bremsstrahlung radiation. It is given in units of g/cm$^2$ or in cm. It can be calculated using the following equation [38]:

$$X_0 = \frac{716.4\ \text{g cm}^{-2}\ A}{Z(Z+1)\ \ln(287/\sqrt{Z})}, \tag{4.2}$$

where $A$ is atomic mass and $Z$ is the atomic number of the absorber material. For high-energy electrons, the energy loss by Bremsstrahlung $\left(-\frac{dE}{dX}\right)_{rad}$ is given in terms of radiation length $X_0$ in equation:

$$\left(-\frac{dE}{dX}\right)_{rad} \approx \frac{E}{X_0}, \tag{4.3}$$

where $E$ is the energy of the electron. When a high energetic electron interacts with matter, it loses its energy via Bremsstrahlung radiation and the resulting photon produces an electron-positron pair giving rise to a cascade, called shower

of electromagnetic particles. The mean free path of a high-energy photon for pair production is 9/7 of a radiation length [38]. Active material of the calorimeter must be thick enough in terms of radiation length in order to absorb the complete electromagnetic shower.

### 4.1.3 Electromagnetic shower

A high-energy photon interacts with matter undergoing pair production and eventually producing a large number of electrons, positrons and secondary gamma rays. It takes about one radiation length to produce an electron-positron pair. High energetic electron-positron pairs create a large number of secondary gamma rays via the Bremsstrahlung process. These secondary gamma rays again undergo pair production and in this way the number of particles in the shower grows exponentially. At each step the energy of the particles in the shower decreases and, eventually, the process stops when the energy of the electrons and positrons is less than the critical energy $E_c$. These electrons and positrons lose their energy in the process of ionization and the gamma rays get absorbed by the photoelectric effect. An electromagnetic shower-development process is illustrated in Fig. 4.2. A multiple scattering of electrons and positrons causes lateral or sideways development of the electromagnetic shower. Bremsstrahlung photons emitted by these electrons and positrons can also contribute to the spread of a shower. The lateral size of a shower can be measured by the Molière radius ($R_M$) which is characteristic of the medium in which the shower develops. It can be approximated in terms of the radiation length $X_0$ and the critical energy $E_c$ by the following expression [38]:

$$R_M \simeq \frac{21\ (\text{MeV})}{E_c\ (\text{MeV})} X_0. \tag{4.4}$$

This relation gives an average lateral deflection of shower electrons at the critical energy after traversing one radiation length.

#### Energy resolution

Particles lose their energy in the electromagnetic calorimeter by causing an electromagnetic shower. The number of particles ($n$) produced inside the shower is

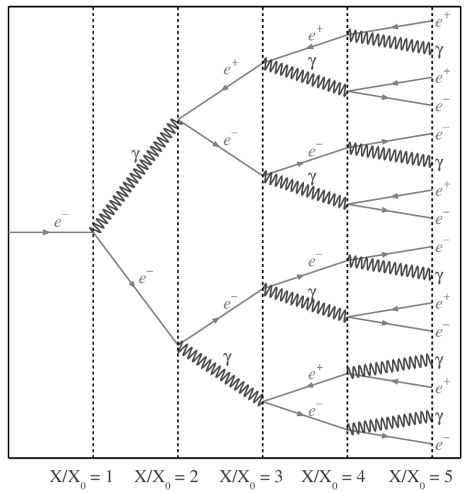


*Figure 4.2: Schematic illustration of the principle of the electromagnetic shower development process as a function of radiation length X in terms of $X_0$ [94].*

proportional to the incident energy ($E_i$). In case of scintillating material with low light yield the photon statistics causes fluctuations. An important factor arising from fluctuations on the detected signal governs the energy resolution and grows as $\sqrt{n}$. Therefore, the intrinsic relative energy resolution of an ideal calorimeter can be expressed as $\sigma(E_i)/E_i \propto 1/\sqrt{n}$. Here, the relative energy resolution is governed only by the stochastic process of shower and light production fluctuations and not by any instrumental effects like signal collection inefficiencies, electronic noise, and geometry of the calorimeter. In a realistic case, the energy resolution of the calorimeter, as shown in equation 4.5 [95], is defined in terms of three main contributing terms responsible for the deterioration in the resolution:

$$\sigma(E) = a\sqrt{E} \oplus b \oplus cE. \tag{4.5}$$

Here, $a$ is the *stochastic term* which includes intrinsic shower fluctuations, photoelectron statistics, dead material at the front of the calorimeter, and sampling fluctuations. The second term $b$ is the *noise term* which includes contributions from the readout electronics noise and does not depend on energy. The third term $c$ is a *constant term* which includes non-uniformities in signal collection and

the possible error in the detector calibration. The symbol $\oplus$ represents addition in quadrature. According to the Cauchy-Schwarz inequality for all vectors $x$ and $y$ it can be shown that:

$$\begin{aligned}
\left(\sum_{i=1}^{n} x_i\ y_i\right)^2 &\leq \left(\sum_{i=1}^{n} x_i^2\right)\left(\sum_{i=1}^{n} y_i^2\right), \\
\left(\sum_{i=1}^{n} x_i\right)^2 &\leq \left(\sum_{i=1}^{n} x_i^2\right)\ n \qquad for\ y = 1, \\
\left(\sum_{i=1}^{n} x_i\ \frac{1}{\sqrt{n}}\right)^2 &\leq \left(\sum_{i=1}^{n} x_i^2\right).
\end{aligned} \tag{4.6}$$

Therefore, the parameter values (such as $a$, $b$, and $c$ in eq. 4.5) for the addition in quadrature ($\oplus$) will be larger by a factor $\sqrt{n}$ than for the simple addition ($+$), which is used in section 5.3.4.

## 4.2 PANDA EMC

### 4.2.1 PANDA experimental requirements

In order to be able to address the different physics topics discussed in chapter 3, the EMC in the PANDA experiment has to meet the following requirements [12]:

- Energy equivalent noise level: 1 MeV,
- Energy threshold: 3 MeV (single crystal) and 10 MeV (cluster),
- Wide dynamic energy range: 3 MeV to 15 GeV photons,
- High resolutions:
  1. Energy $\sigma(E)/E$: $\left(\leq \frac{2\%}{\sqrt{E/\mathrm{GeV}}}\right) \oplus \frac{0.1\%}{E/\mathrm{GeV}} \oplus (\leq 1\%)$,
  2. Time: $\leq$ 1 ns,
  3. Position: $<$ 2 mm,
- High single-crystal hit rate capability: 100 kHz (Barrel) and 500 kHz (Forward endcap),
- Probability of pulse pile-up close to 1%.

In combination with the above-listed technical requirements, the PANDA EMC has to be very efficient in particle identification and in the separation of photons, electrons, $\pi^0$, and $\eta$ mesons. Such performance is required because in charmonium spectroscopy various charmonium states ($J/\psi(1S)$, $\psi(2S)$, $\chi_{cJ}$) and $Y(4260)$ decay via radiative transitions with photons in the final state. In these radiative transition studies, the main background contribution stems from $\pi^0$ and $\eta$ coming from hadronic decays. The $\pi^0$ and $\eta$ mainly decay in two photons. Moreover, the charmonium states $J/\psi(1S)$ and $\psi(2S)$ decay to lepton pairs.

### 4.2.2 Design criteria

The PANDA EMC is one of the crucial sub-detectors of the target spectrometer. The EMC will be placed inside the 2 T magnetic field created by a superconducting solenoid magnet. The EMC is designed to measure energy, position and hit-time of photons, electrons, positrons and neutral mesons; it is designed in three parts, namely the forward endcap, backward endcap and barrel EMC, as shown in Fig. 4.3. High density $PbWO_4$ (PWO) crystals have been chosen as detector material for the PANDA EMC. The PWO crystals will be cooled to $-25°C$ to increase the light yield, which will help to achieve a wide dynamic energy range. At high annihilation rates of 20 MHz, the barrel and the forward endcap EMC will be exposed to single-crystal hit rates up to 100 kHz and 500 kHz, respectively. The different hit rates and mechanical constraints imply different front-end electronics for both the barrel and the forward endcap EMC part. In the barrel readout, Large Area Avalanche Photo Diodes (LAAPD) will be employed as photo sensors with an Application Specific Integrated Circuit (ASIC) pre-amplifier. While in the forward endcap readout Vacuum Photo Tetrodes (VPTT) will be used as photo sensors combined with discrete-component pre-amplifiers. Analog pre-amplifier pulses will be digitized using Sampling Analog to Digital Converter (SADC). The digitized pulses will be further processed online inside Field Programmable Gate Arrays (FPGAs), located on board of the SADC modules, by feature-extraction algorithms implemented in VHDL (Hardware Language). These SADC modules will be placed very close to the front-end electronics. Features of the pulses such as energy and time will then be transferred to the higher level readout chain where data calibration, data reduction,

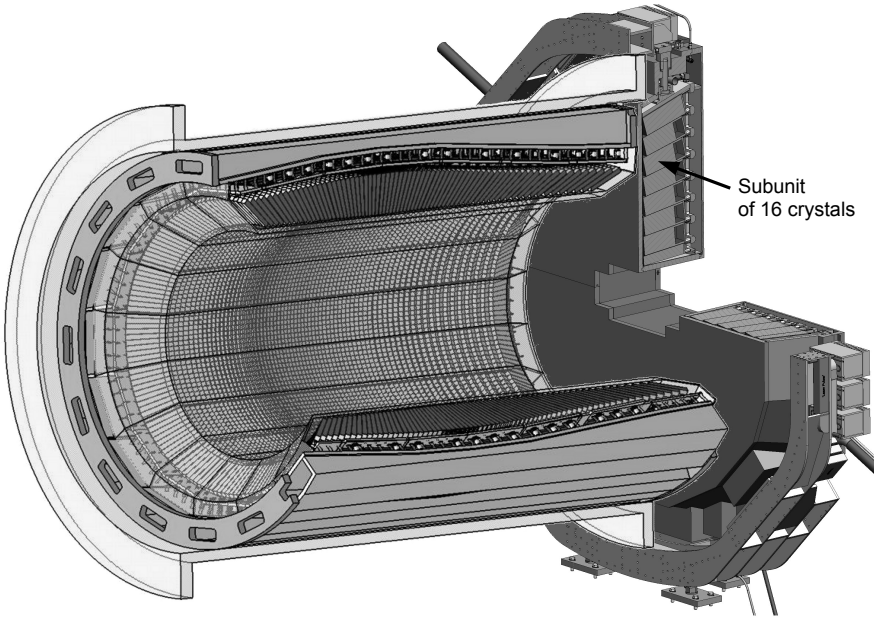


*Figure 4.3: The barrel and forward-endcap components of the PANDA EMC showing the mounting structure of individual PWO crystals and subunits of 16 crystals.*

time synchronization, clustering, and shower energy reconstruction will be done. This reconstructed shower energy information will be used for the physics analysis. The choices of scintillation material, photo sensors, and pre-amplifiers are discussed in the following sub-sections. The higher level readout electronics and the complete readout chain will be discussed in section 4.3.

### Scintillating material

Due to differences in the light production mechanism, scintillators are classified into two types: organic and inorganic scintillators. Organic scintillators are based on organic compounds containing atoms with small $Z$ and, therefore, have a long radiation length (see equation 4.2). Inorganic scintillators are usually crystals grown in high temperature furnaces, often with a small amount of activator im-

purity. These scintillators contain a large fraction of atoms with high $Z$ and, therefore, have a short radiation length.

Organic scintillators are fast but their light yield is poor as compared to inorganic scintillators which usually have a high light yield. The radiation length for organic scintillators ($\sim$ 30 cm) is very high compared to inorganic scintillators (0.9 to 2.6 cm). For gamma rays of 1 MeV energy, the mean free path is about one radiation length. Therefore, a piece of scintillator should be a few radiation lengths thick to have a good detection efficiency. Hence, due to the short radiation length of inorganic scintillators, they are used for the high-energy photon detection. Different types of inorganic scintillators such as CsI, $CsF_3$, BGO, LYSO, $PbWO_4$ are used for high-energy photon calorimetry.

The scintillator for the PANDA EMC should meet the following requirements:

- Short decay time around tens of ns, to perform efficiently in the high hit rate environment,
- Sufficient light yield to achieve a good energy resolution over a wide dynamic energy range,
- Short radiation length to achieve compactness and high granularity for good angular resolution,
- High time resolution, which is important for PID and event building,
- Radiation hardness.

The $PbWO_4$ (PWO) crystals meet all the above-mentioned requirements except the light yield. A special type of crystal (PWO-II) [12] was developed to improve the light yield of PWO by about a factor two by tuning the impurities. Furthermore, a factor four in light-yield improvement has been achieved by cooling PWO-II crystals to $-25°$C [12]. Table 4.1 shows properties of PWO-II and a photograph of PWO-II samples is shown in Fig. 4.4(a). The cross section of an average barrel crystal is $(21.3 \text{ mm})^2$ at the front face, $(27.3 \text{ mm})^2$ at the back face, and the length is about 200 mm [12]. The weight of one crystal is about 0.98 kg. Other scintillating materials such as NaI, CsI, and BGO are excluded due to their long decay time ($\sim$ 230 to 600 ns). $CeF_3$ is not chosen since it has never been produced and tested beyond 10 $X_0$ length and because its emission wavelength does not match the wavelength of optimum quantum efficiency of

| $\mathbf{PbWO_4}$(PWO-II) | |
|---|---|
| **Properties** | **Values** |
| Density $\rho$ | 8.29 g/cm$^3$ |
| Radiation length $X_0$ | 0.89 cm |
| Molière radius $R_M$ | 2 cm |
| Decay time $\tau$ | 6.5 ns |
| Light Yield (LY) relative to LY of NaI | 0.6% at RT and 2.5% at $-25°$C |

*Table 4.1: Properties of the PANDA* $PbWO_4$ *(PWO-II) crystal [12].*

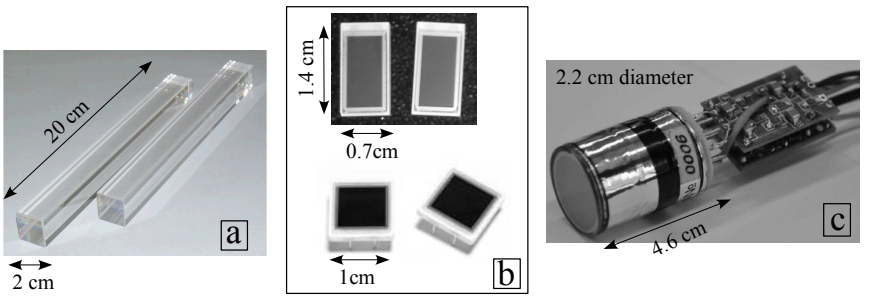


*Figure 4.4: Photograph of* $PbWO_4$ *crystals (a), Rectangular (upper) and Square (lower) Avalanche Photo Diode (b), and Vacuum Photo Tetrode (c).*

LAAPDs. LYSO is a good candidate for calorimetry but it is rejected because of its high cost.

### Photo sensors

Scintillation light, induced by secondary charged particles, will be collected using photo sensors. The main requirements for the PANDA EMC photo sensor are:

- Capability to operate efficiently inside a magnetic field,
- Capability to operate effectively at temperature of $-25°$C,
- Radiation hardness.

The conventional photomultiplier tubes are excluded because of their incapability to operate in magnetic fields. Therefore, for the barrel EMC, the PANDA

collaboration developed together with Hamamatsu Photonics K.K. an Avalanche Photo Diode (APD) [96, 97] with a large area as photo sensor. To maximally cover the end face of the PWO-II crystal, two types of APDs were developed: first, a Large Area APD (LAAPD) [98] with an active area of $(10 \times 10)$ mm$^2$; second, a rectangular APD with an active area of $(14 \times 7)$ mm$^2$. To achieve the maximum coverage, two rectangular APDs can be optically coupled to the endface of the PWO-II crystal. Figure 4.4 (b) shows a photograph of both types of APDs.

For the forward endcap EMC, due to the high expected hit rate, a Hamamatsu Vacuum Photo Tetrode (VPTT) is chosen as photo sensor. The VPTT is radiation hard and can be operated at low temperatures. The gain of the VPTT is expected to reach about 40. In case of the endcap EMC, the magnetic field will be oriented in the axial direction of the VPTT, which will deteriorate the VPTT gain by less than a factor two, thus staying within the EMC requirements [12]. The VPTT measures 46 mm in length and 22 mm in diameter. The photograph of the VPTT is shown in Fig. 4.4 (c). Further details about the APD and VPTT can be found in Ref. [12].

### 4.2.3 Pre-amplifier

The photo sensor collects scintillating light produced in the crystal and creates a charge signal which is amplified by a pre-amplifier and converted to a shaped voltage signal suitable for signal transmission. There are two approaches to build a pre-amplifier: voltage sensitive and charge-integrating pre-amplifier. Schematics of both approaches are shown in Fig. 4.5. The voltage sensitive pre-amplifier has a resistance ($R_1$) at its input which gives rise to noise. To avoid this noise, charge-integrating pre-amplifiers are built to integrate the input charge at $C_i$ using the capacitor $C_f$ as a feedback element. A parallel large-ohmic resistor ($R_f$) is used to reset the amplifier after each pulse. This approach is used to build the PANDA EMC pre-amplifier.

The requirements for the PANDA EMC pre-amplifiers are:

- Low power consumption ($< 100$ mW) to operate inside a cooled volume at $-25°$C,

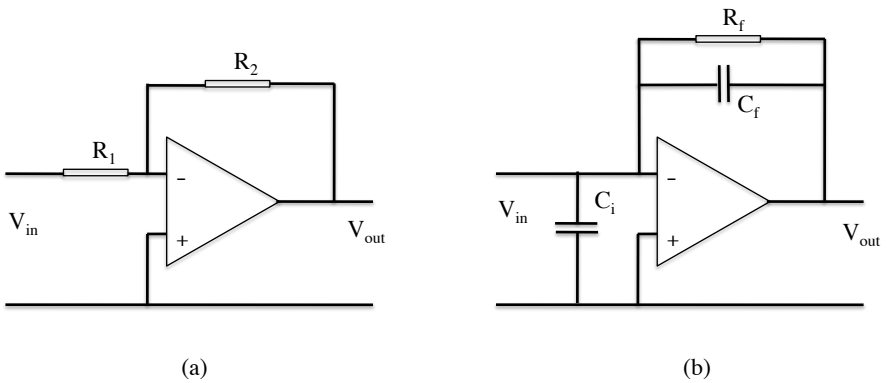


*Figure 4.5: Schematic diagram of (a) A voltage sensitive pre-amplifier with negative feedback, (b) charge-integrating pre-amplifier. The triangle represents an operational amplifier.*

- Low noise ($\leq$ 1 MeV) to achieve a low energy threshold and hence a wide dynamic energy range,
- High hit rate capability (up to 500 kHz) and short pulse width to reduce pulse pile-up.

In order to cope with different hit rates and space limitations, two different pre-amplifiers were developed, namely the Low Noise discrete component Pre-amplifier (LNP) [99] and the ASIC called APFEL (ASIC for PANDA Front-end Electronics) [100].

In the PANDA EMC collaboration, the LNP pre-amplifier is designed at the department of physics, Basel University [101], Switzerland. The output signal of the LNP pre-amplifier has a long decay tail of 25 $\mu$s. A typical output signal of the LNP shaper is shown in Fig. 4.6 (a), where part of the 25 $\mu$s decay tail is visible. Therefore, analog shaping stages are developed to reduce the pulse width. The analog shaper has a single-ended dual-gain output with a pulse width of about 280 ns. A typical output signal shape of the analog shaper is shown in Fig. 4.6 (b). The analog shaper is designed at KVI [102]. For the forward-endcap EMC, the LNP and the shaper coupled with a VPTT will be used to operate in the high-rate environment of about 500 kHz. The performance of the LNP coupled with an APD was tested in an experiment with tagged photons at the Mainz

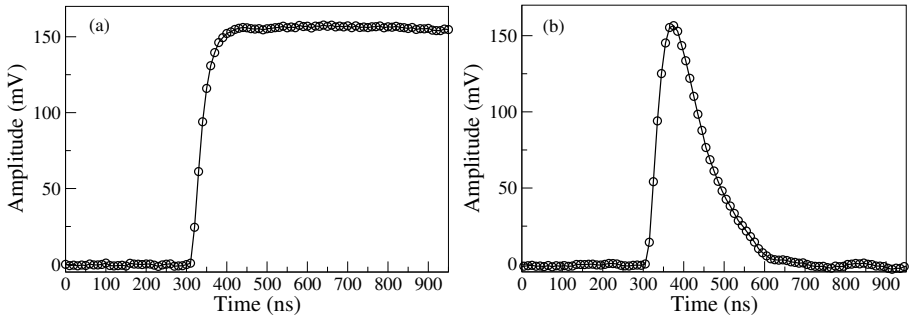


*Figure 4.6: Signal shape obtained using LED light pulser for (a) LNP pre-amplifier only (b) LNP pre-amplifier with a four-stage analog shaper.*

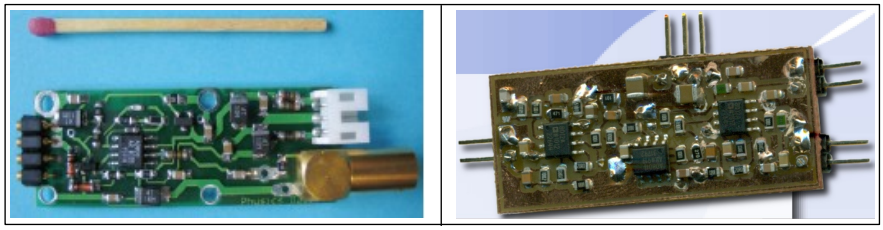

*Figure 4.7: Photograph of the low-noise discrete component pre-amplifier (left) for VPTT readout and the four-stage shaper (right). The dimensions of LNP pre-amplifier and shaper are approximately* $2 \times 4$ cm$^2$.

Microtron (MAMI) accelerator facility in Germany. The obtained noise level is well below 1 MeV [64] at an LAAPD gain of 100. The power consumption is about 50 mW and it is capable to work with high hit rates. A photograph of the LNP and the shaper is shown in Fig. 4.7.

The ASIC pre-amplifier is designed at GSI [28] for the barrel EMC where the maximum expected hit rate is about 100 kHz. It is small in size compared to the LNP and it has a built-in shaper. The ASIC contains two channels with differential dual-gain output. A typical output signal shape of the ASIC pre-amplifier is shown in Fig. 4.8 (a). The pulse width of the ASIC pre-amplifier is about 800 ns with a peaking time of 200 ns and the power consumption per channel is about 60 mW. The test experiment performed with a tagged photon beam at LAAPD gain 100 resulted in a noise level of about 3 MeV which is higher

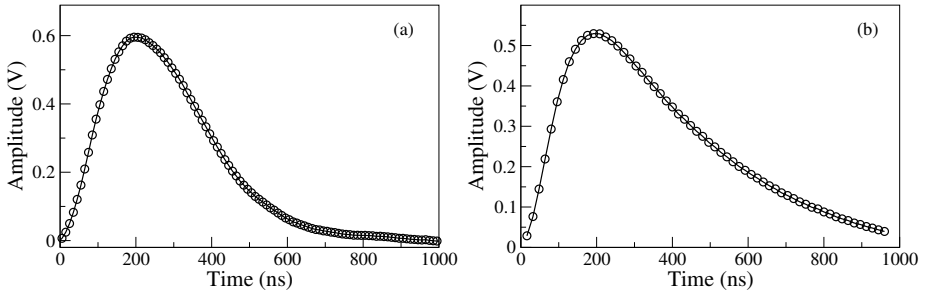


*Figure 4.8: Signal shape obtained using LED light pulser for (a) ASIC pre-amplifier and (b) pre-amplifier designed at KVI.*

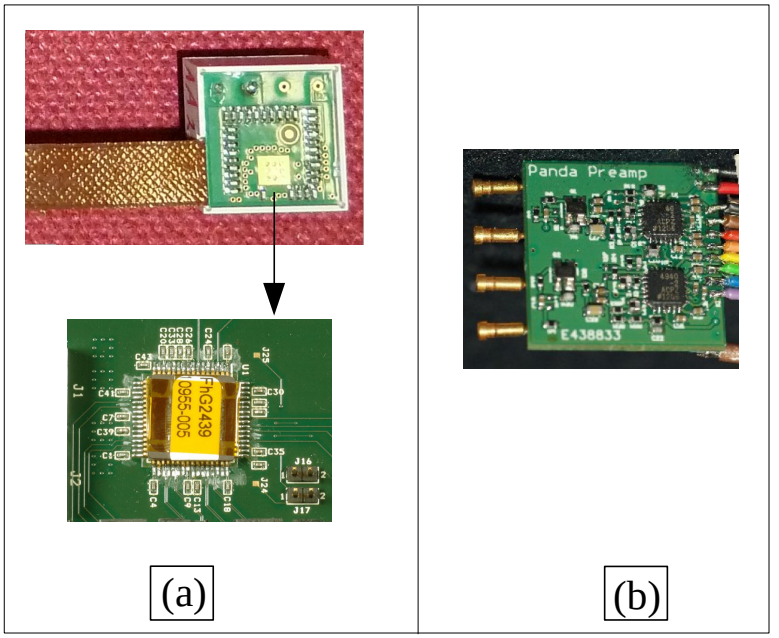


*Figure 4.9: Photograph of (a) the ASIC pre-amplifier (bottom) and the ASIC pre-amplifier mounted on a PCB, placed inside the APD holding capsule (top) designed at GSI and (b) discrete component pre-amplifier designed at KVI. The dimensions of both pre-amplifiers are approximately* $20 \times 20$ mm$^2$.

than expected. Due to imperfect shielding, the pick-up noise contributes to such a high noise level. In the future, improvement in the shielding will help to resolve the problem of a pick-up noise and, therefore, it will be possible to achieve a satisfactory performance of the ASIC pre-amplifier.

An alternative charge-integrating pre-amplifier is under consideration for the barrel EMC. It is a discrete component pre-amplifier developed at KVI [102]. It also has two channels with differential dual-gain output. A typical output signal shape of the KVI pre-amplifier is shown in Fig. 4.8 (b). The pulse width is about 800 ns with a rise time of 150 ns. The noise level is the same as for the ASIC pre-amplifier and the power consumption per channel is about 40 mW. Photographs of both pre-amplifiers are shown in Fig. 4.9.

## 4.3 PANDA EMC readout chain

### 4.3.1 Readout concept

The readout chain of the PANDA EMC is based on the PANDA Data Acquisition (DAQ) concept discussed briefly in section 3.2.3. The PANDA experiment will employ a novel electronics readout concept: *Readout without hardware trigger* called trigger-less readout. This readout concept implies an event selection based on the physics properties of detected particles, like reconstructed invariant mass or a detected secondary vertex. Such an approach requires a completely new design of the readout chain from the front-end to the data acquisition.

The schematic representation of the PANDA EMC readout chain is shown in Fig. 4.10. In this type of trigger-less readout, the EMC signals will be detected above a certain energy threshold and processed on-line in an FPGA of the digitizer module to obtain precisely the energy and the time of the signals in a process called feature extraction. This information will then be transferred to the Data Concentrator (DC) module where the energy calibration will be done. This collective information will be time synchronized using a module called Synchronization Of Data Acquisition (SODA). The crucial component of the readout chain is the synchronous optical-link connection, which will allow to transfer clock signals and time synchronization commands in an unambiguous way. The higher

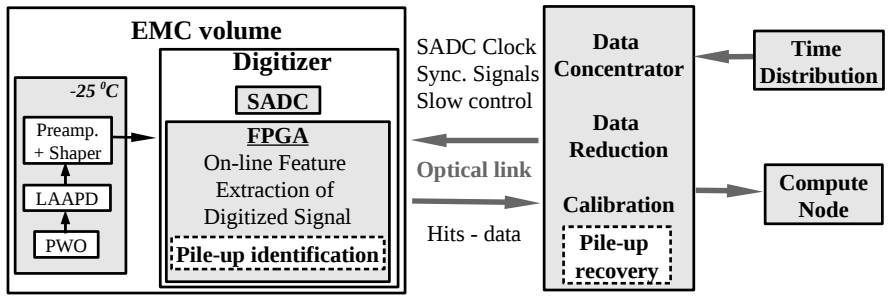


*Figure 4.10: Schematic representation of the PANDA EMC trigger-less readout chain [73].*

level tasks such as clustering, electromagnetic shower-energy reconstruction, particle identification, and event pre-building will be done using a Compute Node (CN) (see section 3.2.3).

The PANDA DAQ combines EMC data with high-level information from all other PANDA sub-detectors, and only to such complete events the physics selection criteria will be applied. In the digitizer part, the pulse-identification algorithm will discriminate single pulses and pile-up pulses caused by a high hit rate at the detector. The single pulses will be fed to the feature extraction part and the pile-up pulses will be sent directly to the DC. In the DC the pulse pile-up recovery algorithm will be applied to recover the energy and the time of the pile-up pulses. This section describes a fully-functional prototype of the readout chain for the PANDA EMC which includes the description of various stages of the readout chain such as the digitizer and the on-line feature extraction, data concentrator, compute node, and the synchronization of the data acquisition system.

### 4.3.2 Prototype of the readout chain

The prototype of the digitizer module contains an SADC which is used to sample and digitize the pre-amplified analog signals. The prototype digitizer module is specially designed for the PANDA EMC prototype readout chain. These modules will be placed very close to the readout electronics of the detector for continuous digitization of the pre-amplifier signals and for on-line data processing inside

their FPGAs. For the on-line data processing the feature-extraction algorithms are developed and implemented [103] in the FPGAs of the digitizer, which include dynamic base-line compensation, hit detection and extraction of the hit information. The on-line data processing helps to reduce the large amount of data and to perform the readout without dead-time. The dead-time of such a readout system is only limited by the pulse pile-up caused by the high hit rate. Using a serial optical-link connection, these reduced data sets will be transferred to the DC module, which will be located outside the PANDA detector. This type of data connection is dictated by the high data rate (few Gb/s) and mechanical constraints.

In the initial period, the commercial 16 bit 100 MHz Struck SADC SIS330 [104], shown in Fig. 4.11 (a), was used for the front-end electronics development. The Struck SADC VME module was chosen because it was possible to modify the standard SADC firmware according to our needs. The feature extraction algorithms were first successfully tested off-line [64] and then implemented in VHDL (Very high-speed integrated circuits Hardware Description Language), which is used to program FPGAs for on-line tests [103].

At present the prototype of a dedicated digitizer module [105] for the PANDA EMC readout chain is designed and shown in Fig. 4.11 (b). The module is designed at Uppsala University [106]. The module sized $110 \times 75$ mm$^2$ hosts 16 SADC channels, operated at 125 MHz sampling rate with a resolution of 14 bit. The on-line feature-extraction firmware is developed at KVI [102]. The firmware was successfully tested on the Struck SADC and is now being used in the Digitizer prototype. All acquired SADC data can be processed on-line by means of a Xilinx Virtex-5 FPGA (XC5FX70T) [107].

The on-line feature-extraction process is designed in two stages, as shown in Fig. 4.12. In the first stage the base-line follower determines and removes the constant offset of the incoming signal. The baseline is determined by averaging the data samples before the pulse. Once the baseline is restored, the data samples above a low-energy threshold are stored. The sum (I) of all samples and the maximum value (A) of these stored data are calculated. The value of the ratio I/A is used for the pulse identification. The pulses which have an I/A ratio above a pre-set value are classified as pile-up or overlapping pulses, and are sent as raw

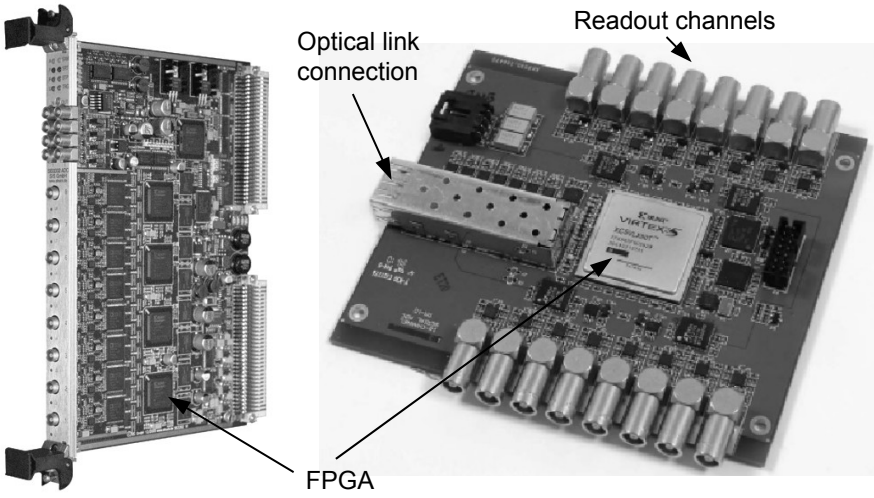


(a) (b)

*Figure 4.11: Photograph of (a) Struck SADC [104] and (b) The prototype SADC specially designed for the PANDA EMC [73, 105].*

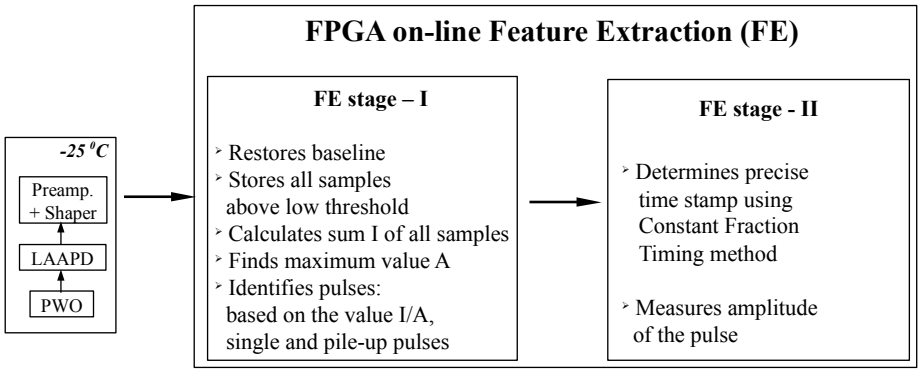


*Figure 4.12: Schematic diagram of on-line Feature-Extraction stages of digitized signals.*

signals to the next step i.e. the DC part of the readout chain. There, the pulse pile-up recovery algorithm will treat these pile-up pulses to restore their energy and time values. The pulses below the pre-set threshold on the I/A ratio are classified as single clean pulses and are sent to the second stage of the feature-extraction process. In the second stage, the single-pulse features such as the pulse amplitude (energy) and the time are estimated. The time stamp is determined by the Constant Fraction Timing (CFT) [64] method. This information is carried to the DC part for the calibration and time synchronization.

The DC module plays a crucial role in the time-distribution system. The time ordering of data from all inputs and communication protocols are developed at KVI [102]. The DC module receives a clock signal and synchronization commands from the time-distribution system and redistributes these data with constant latency to digitizer boards. We define this mode of operation of the optical-link connections as synchronous. The main feature of the synchronous serial connection is a stable and guaranteed phase difference between margins of serial data words and a clock signal for the parallel data. In order to guarantee such a stable phase, a special procedure during the initialization of the serial connection was developed and followed. For the development of the DC functionality, a

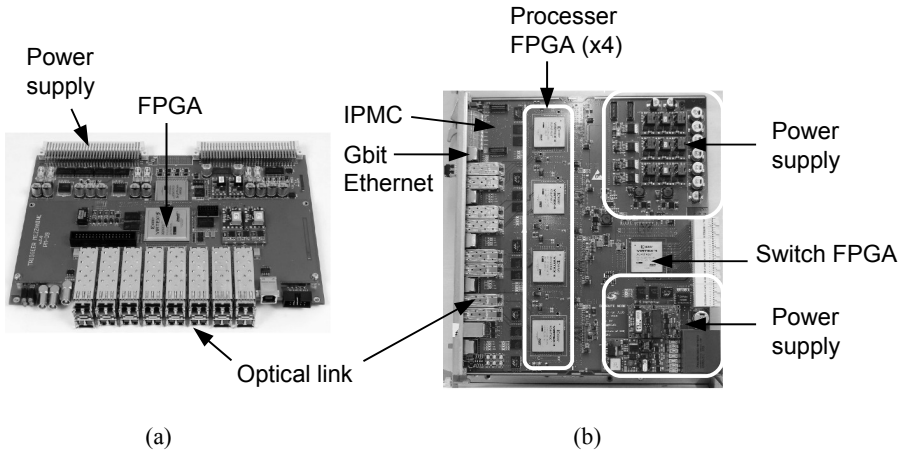


*Figure 4.13: Photograph of (a) Data Concentrator module [73] and (b) Compute Node [108], respectively.*

module [105] designed for the WASA experiment [109] was used. The module was designed at Uppsala University [106]. The DC module, shown in Fig. 4.13 (a), consists of a motherboard with VME interface and a piggyback board with 16 high-speed optical interfaces (up to 3.2 Gb/s) directly coupled to a Xilinx Virtex-5 FXT FPGA. The EMC readout-prototype employs only this piggyback board of the module. The details of the functional prototype of the hardware trigger-less readout prototype developed for the PANDA EMC are documented in Ref. [73].

The trigger-less readout concept requires a precise time synchronization of all data acquired by the digitizer modules. Therefore, all SADCs should use the same clock source and there should be a possibility to set simultaneously the zero-time for all digitizers. For this purpose the PANDA experiment employs a time-distribution system to be developed along the lines of the SODA [70] idea which includes a specially designed data-transfer protocol. The implementation and performance tests of the synchronous optical-link connection for the PANDA EMC are described in Ref. [73].

To complete the readout chain, the Compute Node (CN) [108] which is already developed and used in the BESIII experiment [9], is applied. Fig. 4.13 (b) shows a photograph of the CN. Its basic building blocks are 5 XILINX Virtex 4 FX60 FPGAs. Four FPGAs are used to execute the algorithms. The $5^{\text{th}}$ FPGA serves as a switch connecting to other CN modules in the same ATCA (Advanced Telecommunications Computing Architecture) [108, 110] shelf via a full-mesh backplane. The CN has 2 GB DDR2 RAM per FPGA (10 GB total) and two embedded power PCs in each FPGA. A customized Intelligent Platform Management Controller (IPMC) is used to fulfill the ATCA requirements such as adjusting the power consumption in agreement with requirements imposed by the ATCA shelf manager, voltage and temperature monitoring, and FPGA configuration check. As part of the prototype readout chain the CN is used in the test experiment reported in chapter 6. More details about the CN can be found in Ref. [108].

# Chapter 5

# Pulse Pile-up Recovery Algorithm

***This chapter is published as: "Pulse pile-up recovery for the front-end electronics of the PANDA Electromagnetic Calorimeter", G.Tambave et al. JINST 7, P11001, 2012. doi:10.1088/1748-0221/7/11/P11001***

In the PANDA experiment, 1.5 to 15 GeV/c antiprotons will annihilate with a hydrogen target at rates up to 20 MHz. Due to such high annihilation rates, the EMC will be exposed to single-detector hit rates of up to and above 500 kHz, which will lead to pulse overlap. Hence, to recover energy and time information of the overlapping pulses, a pulse pile-up recovery method is developed. The pulse pile-up identification is done by monitoring the ratio of pulse integral over pulse amplitude. The estimated pile-up identification efficiency is almost 100% and the false rate of identification is below 1%. The Moving Window Deconvolution is used to obtain almost symmetric pulse shapes. The Constant Fraction Timing algorithm is applied on the trailing edge of the symmetric pulses to accurately determine the time stamp of pile-up pulses. The energy and the time information

of pile-up pulses can be recovered up to time differences of 50 ns, equal to the pulse rise-time, in a large dynamic energy range. The method is easy to implement in FPGA for on-line data processing.

This chapter is divided in four subsections. Section 5.1 gives a brief introduction and motivation behind the development of the pile-up recovery algorithm. The experimental setup used to produce single pulses as well as pile-up pulses is described in section 5.2. Section 5.3 contains a detailed description of various studies such as pulse shape stability, pile-up pulse identification algorithm, energy and time recovery algorithms, simulation details, and results on pile-up probability. The summary and conclusions of the chapter are presented in section 5.4.

## 5.1 Introduction

In the PANDA experiment, antiprotons with momenta between 1.5 GeV/c and 15 GeV/c will interact with either a pellet or a cluster-jet hydrogen target at annihilation rates of up to $2 \cdot 10^7$ events/s. Since PANDA is a fixed target experiment, single crystal hit-rates of up to 100 kHz are expected in the barrel EMC and more than 500 kHz in the forward endcap EMC. These high rates may lead to pulse overlap i.e. pile-up. The simulated hit-rate distribution [12] for the forward endcap EMC is shown in Fig. 5.1.

The scheme of the PANDA EMC trigger-less readout chain [73] is shown in Fig. 4.10 (see section 4.3). In the initial stage of the digitization process the shaped pile-up pulses will be identified and then transferred to the data concentrator where the pile-up recovery algorithm will be applied. The pile-up recovered information will be sent to the compute node for on-line clustering and shower energy reconstruction. The single-pulse feature-extraction algorithms have already been implemented in FPGA and tested successfully [103]. At present, the FPGA implementation of the algorithm is re-written in a pipelined way, which eliminates dead-time caused by the data processing. The only possible source of dead-time of the system is pile-up of two or more sequential pulses.

To deal with pile-up pulses, various methods have been introduced and developed [111–113]. Since the data for the PANDA EMC will be processed on-line

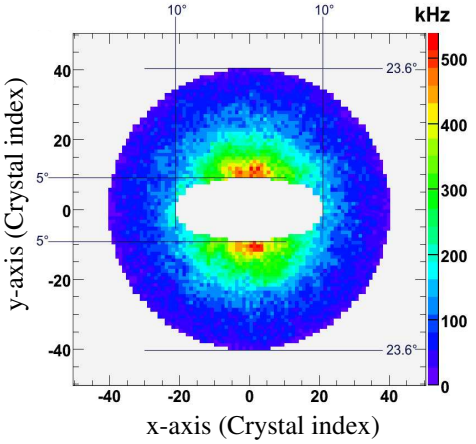


*Figure 5.1: Integrated single-crystal hit rate [12] as a function of vertical and horizontal coordinates for the forward endcap EMC simulated using the DPM (Dual Parton Model) generator at antiproton beam momentum of* 15 GeV/c. *The hit rate is about* 500 kHz *at a polar angle of about* 5°.

in FPGAs, we are developing an FPGA-friendly method. The digitizer modules, which will process the data on-line, will be located inside the detector volume. This arrangement sets constraints on the power consumption. Therefore, the developed data processing algorithms have to consume as little resources as possible.

In this work the pile-up pulse recovery algorithm is developed and tested off-line on the LED light-pulser data as well as on simulated pile-up pulses over a large dynamic range for various combinations of amplitude ratios (first pulse / second pulse). Single pulses measured with the EMC prototype using a 10 GeV positron beam are employed to validate the pulse shape stability. The implementation of the pile-up recovery algorithm in VHDL code for an FPGA is in progress. The off-line tests reveal that the pile-up pulse recovery method can recover pile-up pulse information up to a minimum pulse distance of 50 ns keeping the dead-time of the readout chain below 50 ns, which is equal to the pulse rise time.

Due to fluctuations in the hydrogen pellet target density [51] (see chapter 3)

the peak hit rate at the forward endcap EMC will be 1 MHz, instead of the expected 500 kHz, resulting in a pile-up probability of up to 21% for the pulse width of 280 ns. By applying the proposed pile-up recovery method the pile-up probability is reduced to 4.2%. At nominal hit rates of 500 kHz, the pile-up probability of 12% is reduced to 2.4%.

## 5.2 Experimental setups

This section describes two different experimental setups used in the reported study. The first setup, described in section 5.2.1, was designed to study the performance of the pulse pile-up recovery algorithm. The setup produces pile-up pulses by using two LED light pulses and delaying one of them. In this way it was possible to study energy and time recovery for various time differences between two pile-up pulses as well as for different amplitude-ratio combinations of two pulses (first pulse / second pulse). The second experimental setup, described in section 5.2.2, was designed to study the single pulse shape stability over a large dynamic energy range. The pulse shape stability plays an important role in the energy recovery of the pile-up pulses. Single pulses were produced by a 10 GeV positron beam aimed at a PWO crystal, kept at $-25°$C.

### 5.2.1 LED light pulser setup

The block diagram of the electronics configuration used for systematic studies of pile-up events is shown in Fig. 5.2. The setup consists of a single $2 \times 2 \times 20$ cm$^3$ $PbWO_4$ (PWO) scintillating crystal kept at room temperature. A Large Area Avalanche Photodiode (LAAPD) photo sensor with gain of 200 was mounted on a $2 \times 2$ cm$^2$ face of the PWO crystal. The sensor was coupled to a LNP pre-amplifier [99] with four-stage (dual gain, rise time 50 ns) analog shaper feeding signals to a 16-bit 100 MHz Struck [104] Sampling ADC (SADC). Two LED light pulsers were used to generate double-pulses. The light pulse of the LED-2 was delayed using a variable delay line in order to generate pulse pile-up. The light was guided using a bundle of optical fibers, shining light on the face of the PWO crystal opposite to the LAAPD. In this setup the PWO crystal acts as

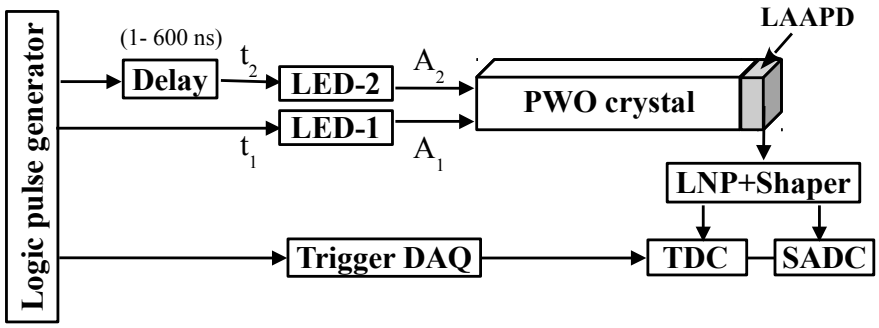


*Figure 5.2: The block-diagram of the experimental setup. The details are explained in the text.*

waveguide. The LNP pre-amplifier converts the charge signal from the LAAPD to voltage pulses with a long exponential tail of 25 $\mu$s. The LNP pulses were further shaped using a four-stage analog shaper, resulting in the pulse width of 280 ns. The analog-shaper pulses were digitized by the SADC. Data were collected for various time differences $\Delta\tau$ by making a time scan of the delayed pulse over a time interval of 1 ns $< \Delta\tau <$ 600 ns for various pulse amplitudes $A_1$ and $A_2$. During the scan measurements, the $\Delta\tau$ distribution was kept as close as possible to a uniform distribution. In addition to the SADC data, the reference time of the first ($t_1$) and the second ($t_2$) pulses were recorded by the time-to-digital converter (TDC).

A VERSAModule Eurocard (VME) bus and a Multi-Branch System (MBS) [114] developed at GSI [28] were used to readout the SADC and the TDC modules. The MBS runs on the Lynx real-time operating system in a VME PowerPC controller RIO3 8064 from Creative Electronic Systems (CES) [115]. The Transistor Transistor Logic (TTL) output of the pulse generator was used to trigger the Data AcQuisition (DAQ) via a TRIVA VME module [116]. The TRIVA module triggers the acquisition only when the logic pulse from the coincidence of interest occurs. On-line visualization of the data stream was performed using the GSI Object Oriented On-line Off-line system, Go4 [117] which is based on the ROOT [76] package developed at CERN [62].

An example of a digitized pile-up pulse waveform for the time difference of

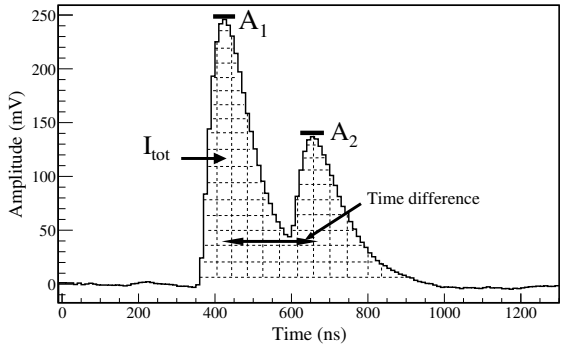


*Figure 5.3: Digitized pile-up pulse waveform, generated by two LED light pulsers. The time difference ($\Delta\tau$) between the first and the second pulse is about 200 ns and the amplitude ratio ($A_1/A_2$) is 2 where $A_1$ is the first, $A_2$ is the second pulse amplitude and $I_{tot}$ is the integral of the pile-up pulse waveform.*

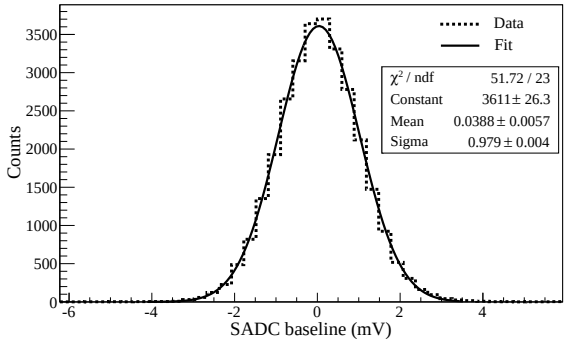


*Figure 5.4: Baseline distribution of the digitized signal trace. The dashed line corresponds to the measured data and the solid line to the Gaussian fit. The width obtained from the fit indicates the noise level of $\sigma \approx 1$ mV.*

200 ns and the amplitude ratio of around 2 ($A_1/A_2 = 246$ mV/121 mV) is shown in Fig. 5.3. Here, $A_1$ is the first and $A_2$ is the second pulse amplitude. The baseline distribution of the digitized signal trace is shown in Fig. 5.4. The width obtained from the Gaussian fit indicates the noise level of $\sigma \approx 1$ mV.

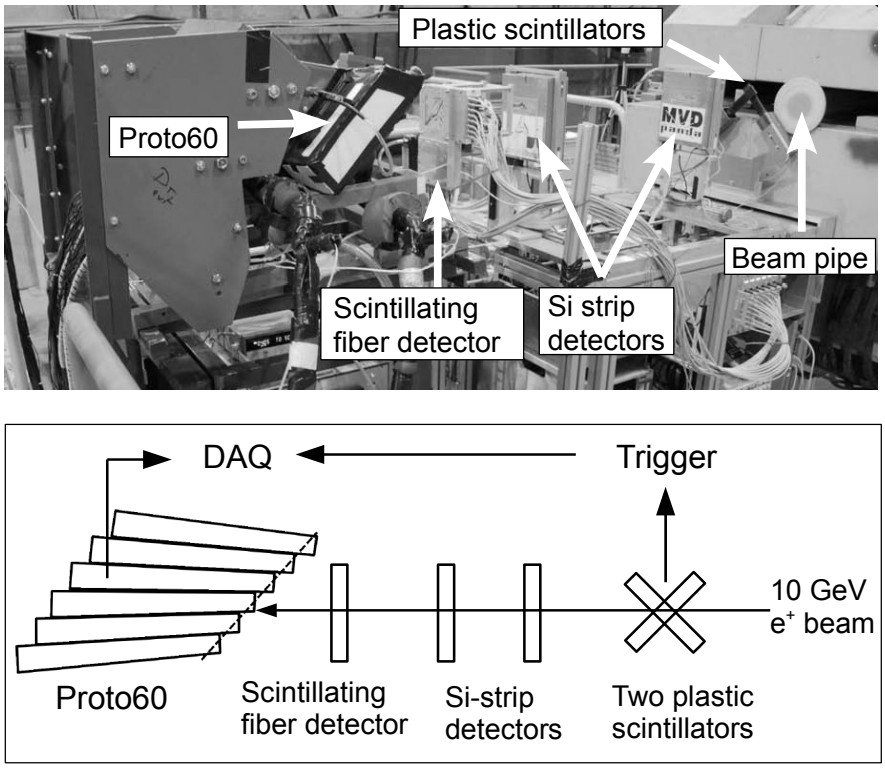


*Figure 5.5: Photograph (upper panel) and schematic representation (lower panel) of the experimental setup.*

### 5.2.2 Positron beam setup at CERN

The aim of the experiment was to study the single-pulse shape stability over a large dynamic energy range. The experiment was performed in the North area of the CERN accelerator complex [118] at Geneva, Switzerland. A 10 GeV positron beam was aimed at the center of the PWO-II crystal. The beam diameter was about 2 cm and the maximum possible beam rate was about 100 Hz. Therefore, data were collected only for single pulses, which are useful for the experimental verification of the pulse-shape stability.

The experimental setup is shown in Fig. 5.5. The setup consists of the EMC

prototype of sixty PWO-II crystals (proto60) [64], a scintillating fiber detector, two silicon strip detectors and two plastic scintillators. The PWO-II crystals were read out using LAAPDs (see section 4.2.2) coupled with LNP pre-amplifiers and analog shaper modules (see section 4.2.3). The gain of the LAAPD was 50. Shaped analog signals were digitized using a sampling ADC. The scintillating fiber and silicon-strip detectors were mounted for the positron beam tracking and position resolution studies. The tracking information was not used for the analysis reported in this chapter. The two plastic scintillators were used to trigger the DAQ. The DAQ system described in the previous section was used for the readout and data storage.

## 5.3 Algorithm, results, and discussion

### 5.3.1 Pulse shape stability

#### Using LED light pulser

Measurements with a single LED light pulser were performed in order to confirm the pulse-shape stability. We measured a linear relation between the pulse amplitude ($A$) and the pulse integral ($I$), i.e., $I = k \cdot A$, where $k$ is a calibration constant. The distributions of the pulse integral and the $I/A$ ratio as a function of the pulse amplitude for single pulses are shown in Fig. 5.6 (a) and (b), respectively. The pulse integral is the sum of all samples above a certain energy threshold. Since there are no significant deviations of the $I/A$ ratio from a constant value, the pulse shape is obviously stable for various pulse amplitudes.

#### Using 10 GeV positron beam

To verify the pulse-shape stability observed with the LED light pulser, measurements were performed using a 10 GeV positron beam. The experimental setup and the data collection were explained in section 5.2.2. The distributions of the pulse integral and the $I/A$ ratio as a function of the pulse amplitude for single pulses are shown in Fig. 5.7 (a) and (b), respectively. The relation between the pulse amplitude and the pulse integral, obtained by using the positron beam,

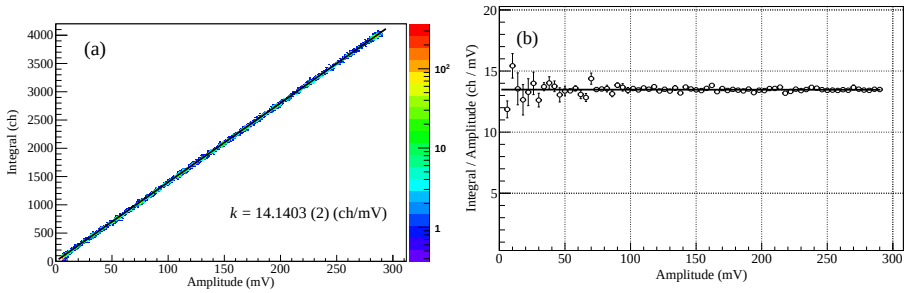


*Figure 5.6: The pulse integral (a) and the ratio of the pulse integral over the pulse amplitude (b) as a function of the pulse amplitude obtained for single pulses using the LED light pulser. The linear relationship with slope parameter k between the integral and amplitude of a pulse indicates that the pulse shape is stable for different pulse amplitudes.*

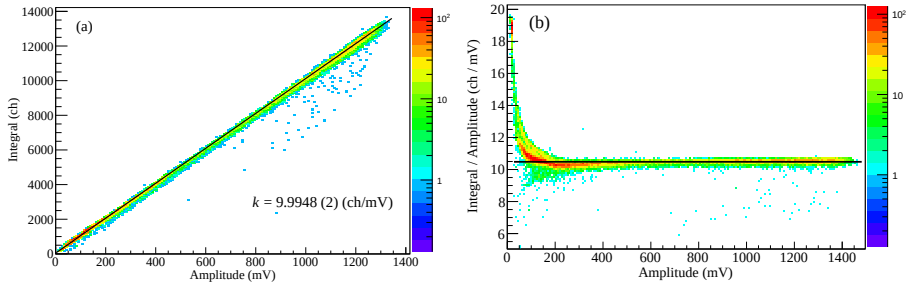


*Figure 5.7: The pulse integral (a) and the ratio of the pulse integral over the pulse amplitude (b) as a function of the pulse amplitude obtained for single pulses using the 10 GeV positron beam. The slope parameter of a linear fit is given in (a).*

is linear as already measured in light-pulser studies reported in the previous paragraph (see Fig. 5.6). Therefore, we conclude that the pulse shape is stable for larger pulses up to the pulse amplitude of 1.5 V. The linearity measured with beam can be considered as an extension of the low-amplitude measurements shown in Fig. 5.6 (a). Since the beam was aimed at a single PWO-II crystal, the maximum range of about 1.5 V of the pulse amplitude plotted in Fig. 5.7 (b) roughly corresponds to 7 GeV energy deposition. In the high-energy region up

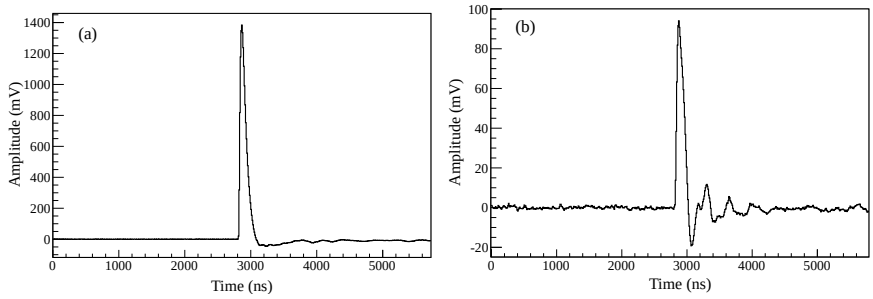


*Figure 5.8: (a) A high-energy clean pulse shape and (b) a low-energy pulse shape distorted due to cross talk.*

to 7 GeV the pulse shape is stable and this stability can be safely extrapolated to the maximum energy deposition of 12 GeV in the single crystal. The $I/A$ ratio in Fig. 5.7 (b) is not constant in the low-energy region. This deviation is caused by the cross talk between neighboring readout channels of the analog shaper. An example of cross talk is shown in Fig. 5.8 (b). When a high-energy pulse is measured in one of the readout channels (Fig. 5.8 (a)), a distorted pulse is induced in the neighboring channels (Fig. 5.8 (b)). The distorted pulse shape is clearly visible in Fig. 5.8 (b). This pulse-shape distortion changes the pulse integral and the value of the $I/A$ ratio increases as seen in the low-amplitude region of Fig. 5.7 (b). The cross talk between the readout channels is removed in the improved design of the shaper [119] and, therefore, future measurements will be free from cross talk.

### 5.3.2 Pile-up pulse identification

As mentioned in section 5.1, the pulse pile-up identification takes place in the digitizer (Fig. 4.10) in the initial stage of the digitization process. For the identification process the following considerations are in order. The pile-up of two pulses happens when both pulses have amplitudes above a certain value of the pulse-detection threshold and both pulses merge into a single structure extending above the threshold. The pile-up identification algorithm is based on the assumption of stability of the pulse shape in the complete dynamic range. For a stable

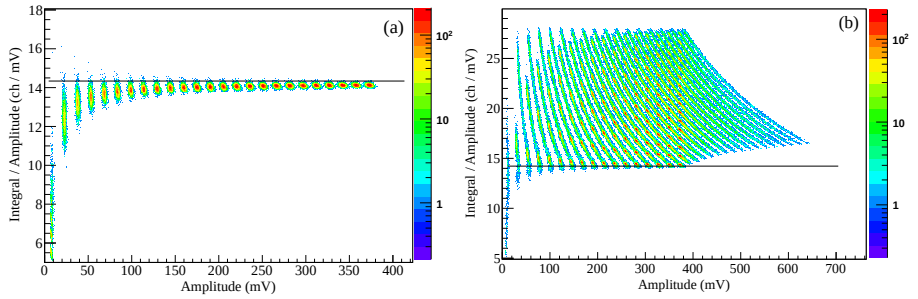


*Figure 5.9: The ratio of the pulse integral over the pulse amplitude as a function of the pulse amplitude from simulations: (a) for single pulses only; (b) for pile-up pulses only. The horizontal line indicates the pile-up identification threshold* $T_{I/A} = 14.3$ ch/mV.

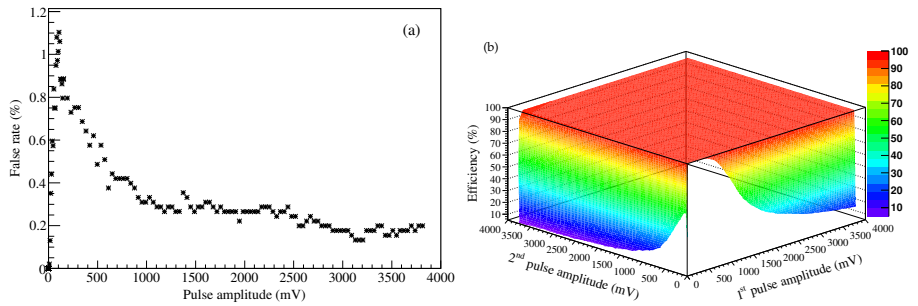


*Figure 5.10: (a) The false rate of pile-up identification as a function of the pulse amplitude. (b) The efficiency of the pile-up identification as a function of the first- and the second-pulse amplitudes covering an amplitude ratio of 500 ranging from 7.6 mV to 3.8 V.*

pulse shape, the $I/A$ ratio does not depend on the pulse amplitude. However, in the case of pile-up the pulse shape is distorted and the $I/A$ ratio increases. This effect is used for the pile-up pulse identification by monitoring the $I/A$ ratio for the incoming pulses.

Simulations were done to study the performance of the pile-up identification method. The simulation technique is described in section 5.3.4. The $I/A$ ratio as a function of the pulse amplitude for single pulses only and for pile-up pulses

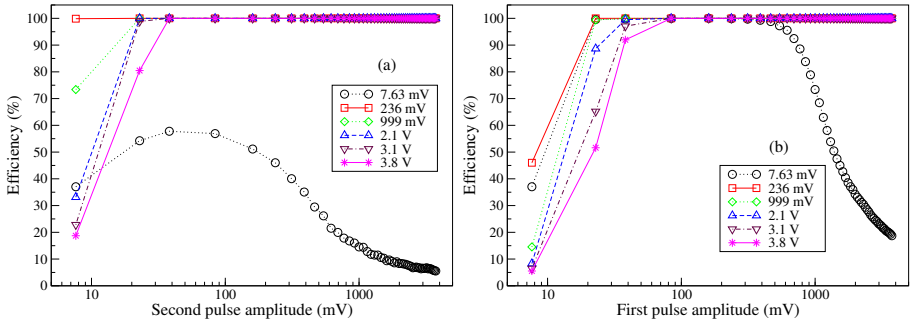


*Figure 5.11: Pile-up identification efficiency as a function of: (a) the second-pulse amplitude for various values of the first-pulse amplitude; (b) the first-pulse amplitude for various values of the second-pulse amplitude. Note the logarithmic horizontal axis.*

is shown in Fig. 5.9 (a) and (b), respectively. For single pulses, the $I/A$ ratio is almost constant around 14.3 ch/mV, except for the very low pulse amplitudes close to the detection threshold. To calculate the pulse integral, all samples above the threshold are summed up. This simple and fast method of the pulse-integral estimation yields a precise result only for pulses with amplitude much higher than the threshold. In the low-amplitude region the method underestimates the pulse integral. Therefore, as can be noticed in Fig. 5.9 (a), the $I/A$ ratio in the low-amplitude region drops below the constant value. However, as shown in Fig. 5.9 (b), the $I/A$ ratio for pile-up pulses is larger than observed for a single pulse. Therefore, the pile-up identification is achieved by setting a discriminating threshold $T_{I/A}$ on the $I/A$ ratio. For the investigated pulse shape the optimal threshold value $T_{I/A} = 14.3$ ch/mV was found. This threshold value is indicated as horizontal line in Fig. 5.9 (a) and (b) and yields a false pile-up identification rate below 1%. The false rate is obtained by simulating single pulses of different amplitudes and counting the fraction of pulses above the $I/A$ threshold. The obtained false pile-up identification rate as a function of the pulse amplitude ranging from 7.6 mV to 3.8 V is shown in Fig. 5.10 (a). The fraction of pulses above the $I/A$ threshold in Fig. 5.9 (b) is defined as the pile-up identification efficiency. The obtained efficiencies as a function of the first and the second pulse amplitude are shown in Fig. 5.10 (b) covering the dynamic range of 500. Because

of the smooth and flat behavior at large pulse amplitudes, the efficiencies obtained in the investigated dynamic range of 500 may be safely used as upper limits for the required larger dynamic range of 10,000. Figure 5.11 shows corresponding slices of the efficiency distribution: (a) for various fixed first-pulse amplitudes and (b) for various fixed second-pulse amplitudes. The detection efficiency is almost 100% for the high-amplitude combinations of pile-up pulses. The efficiency decreases only if one of the pile-up pulse amplitudes approaches the pulse-detection threshold. Therefore, we may conclude that the described pile-up detection algorithm is sufficiently robust and efficient. Moreover, due to its simplicity, the algorithm will consume only little resources in the digitizer FPGA.

### 5.3.3 Energy recovery

In case of two events close in time, it is possible to measure the first-pulse amplitude ($A_1$) and the integral ($I_{tot}$) of the pile-up pulse structure, which contains the energy information of both pulses. Thus, the relation between amplitude and integral is given by $I_{tot} = k(A_1 + A_2)$, which implies $A_2 = (I_{tot}/k) - A_1$, where $A_2$ is the second pulse amplitude, see Fig. 5.3. In this section, the energy recovery studies, performed with LED light-pulser data, are discussed. The experimental setup and the data collection details were reported in section 5.2.1. In Fig. 5.12, as an example, the amplitudes of the first and the second pulses are plotted as a function of the reference time difference ($\Delta\tau = t_2 - t_1$) between the first and the second pulses, calculated for the amplitude ratio 2. Two regions are defined by the time $T_0 = 280$ ns (black dashed line): $\Delta\tau < T_0$ is the pile-up pulse region and $\Delta\tau > T_0$ is the separated-pulse region. In this second region, the amplitudes shown on the vertical axis are found to be constant (horizontal straight lines) and independent of the time difference. At the interface between these two regions, i.e. at time differences between 280 and 300 ns, the amplitudes do not match perfectly. Obviously, the pile-up region should have been chosen slightly wider up to 300 ns. In the region below 50 ns the amplitudes are not constant, since in this region both pulses overlap completely and appear like a single pulse. In the pile-up region, the second-pulse amplitude (black data points) is recovered down to a time difference of 50 ns and the recovered amplitude is constant. The recovery of the second-pulse amplitude is limited by the pulse rise time of 50 ns.

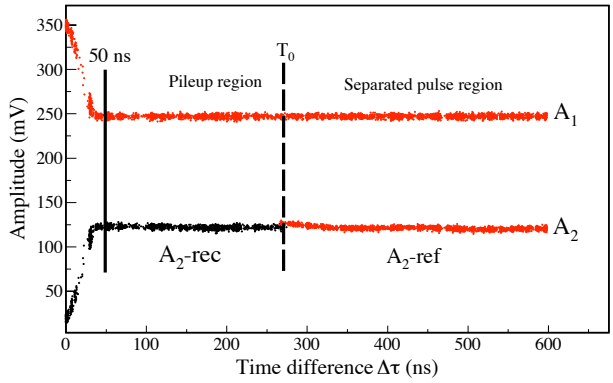


*Figure 5.12: Pulse amplitudes as a function of the time difference ($\Delta\tau$) for the amplitude ratio 2. Two regions are defined using the time* $T_0 = 280$ ns*: $\Delta\tau < T_0$ (pile-up pulse region) and $\Delta\tau > T_0$ (separated-pulse region). The black data points indicate the recovered second pulse ($A_2 - \mathrm{rec}$) amplitudes which extend into the separated-pulse region as the reference signal $A_2 - \mathrm{ref}$. The $A_2 - \mathrm{rec}$ amplitude is recovered down to a minimum time difference of 50 ns which is equal to the rise-time of the pulse.*

The pile-up probability for the forward endcap EMC, estimated using a Poisson distribution function (see section 5.3.7) is about 12% at a hit rate of 500 kHz for the pulse width of 280 ns as found in section 5.2. Since the pile-up pulse amplitude is recovered down to a time difference of 50 ns, the pile-up probability is reduced to 2.4%, which is close to the PANDA EMC requirement of about 1% [12].

The projections onto the vertical axis of Fig. 5.12 for $\Delta\tau > 50$ ns are shown in Fig. 5.13 (a) and (b). Fig. 5.13 (a) shows the projection over the time interval of $\Delta\tau > T_0$, the region where pulses are well separated, to obtain the reference resolution for the second pulse. Fig. 5.13 (b) shows the projection over the time interval of 50 ns $< \Delta\tau < T_0$, to obtain the amplitude value and resolution measured after the recovery procedure. A complete pile-up pulse amplitude recovery is achieved if the recovered pulse amplitude coincides with the reference measurement. The relative energy resolution $\sigma/\mu$, measured in % is obtained using a Gaussian fit to both the amplitude distributions. The measured reference energy resolution is 1.37% and the recovered resolution is 1.41%. This difference

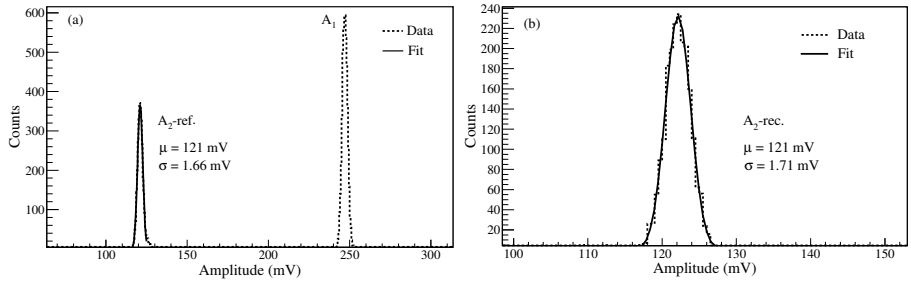


*Figure 5.13: The amplitude distributions obtained by projecting the curves in Fig. 5.12 onto the vertical axis: (a) $\Delta\tau > \mathrm{T}_0 = 280$ ns, the region of well-separated pulses i.e. the reference pulse amplitude ($\mathrm{A}_2$-ref.). (b) $50\ \mathrm{ns} < \Delta\tau < \mathrm{T}_0$, the pile-up region, where the second pulse amplitude ($\mathrm{A}_2$-rec.) is obtained by the recovery method. The dashed black-line histogram corresponds to the measured data and the solid black-line to the Gaussian fit.*

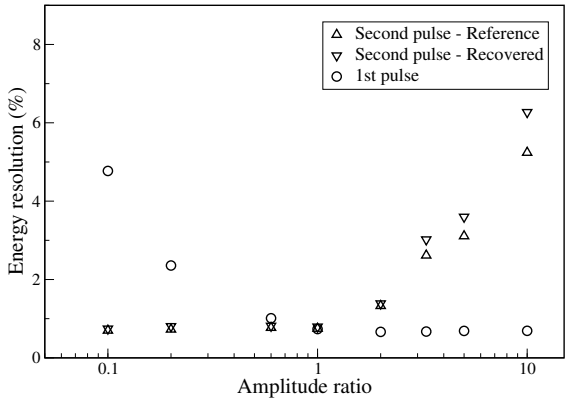


*Figure 5.14: The relative energy resolution $\sigma/\mu$ averaged over a range of time differences is shown as a function of the amplitude ratio. The amplitude ratio of 10 corresponds to a first-pulse amplitude of 250 mV and a second-pulse amplitude of 25 mV. The up-triangle, down-triangle, and circle data points indicate the measured energy resolution for the second reference pulse, the second recovered pulse, and the first pulse, respectively.*

in the resolution is mainly caused by the error propagation of the first-pulse amplitude measurement into the determination of the second-pulse amplitude. We thus conclude that for a time difference larger than 50 ns the second-pulse amplitude can be fully recovered within 1.5%. The same procedure as described above is followed to study the pulse-amplitude recovery for various amplitude ratios ($A_1/A_2$). The relative energy resolution $\sigma/\mu$ averaged over a range of time differences $\Delta\tau$ is plotted as a function of amplitude ratios in Fig. 5.14. The circles indicate the resolution values of the first pulse. The reference resolution (up triangle) averaged over an interval of time differences with $\Delta\tau > T_0$ is compared to the recovered resolution (down triangle) averaged over an interval of time differences with 50 ns $< \Delta\tau <$ $T_0$. The maximum deviation in resolution is seen for high amplitude ratios, while for low pulse-amplitude ratios the deviation is smaller.

### 5.3.4 Simulation studies for energy recovery

#### Single-crystal detector pulse pile-up

In order to test the performance of the energy recovery method for combinations of signals in a wide range of pulse heights, we have simulated special test waveforms. We used the function shown in equation 5.1, which describes the measured pulse shape:

$$f(x) = A\left(\frac{x-t}{\tau}\right)^N e^{-N\ (\frac{x-t}{\tau})} + Bl \tag{5.1}$$

Here, the pulse amplitude is obtained as $A\ e^{-N}$ from the parameters $A$ and $N$, $Bl$ is the baseline, $\tau$ is the decay time, and $t$ is the time stamp. The single pulse shape shown in Fig. 5.15 (a) was fitted using equation 5.1. This function was used to introduce two additional pulses into the measured signal trace with a time difference chosen in an interval of 50 ns $< \Delta\tau <$ 280 ns. In this way, we can control precisely the amplitude values of the simulated pulses, preserving the realistic noise of the measured waveforms. An example of the simulated pulse is shown in Fig. 5.15 (b).

The simulated waveforms were analyzed by following the same procedure used for the measured data. The recovered second-pulse energy resolution $\sigma/\mu$ plotted

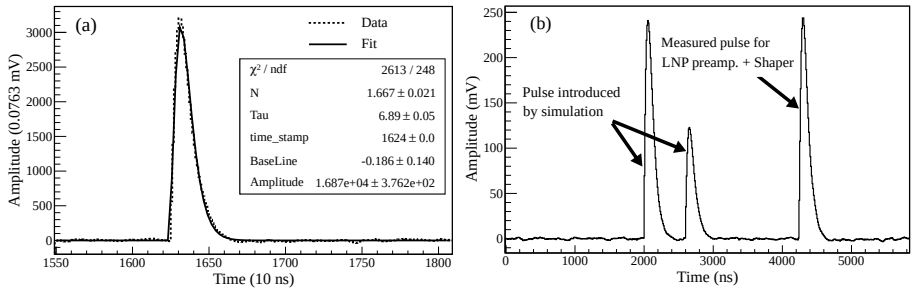


*Figure 5.15: (a) The single LNP + shaper pulse fitted using equation 5.1. The pulse amplitude is defined by the parameters Amplitude (A) and N as $A\, e^{-N}$. (b) The two pulses introduced by the simulation and the single pulse measured after the LNP + shaper.*

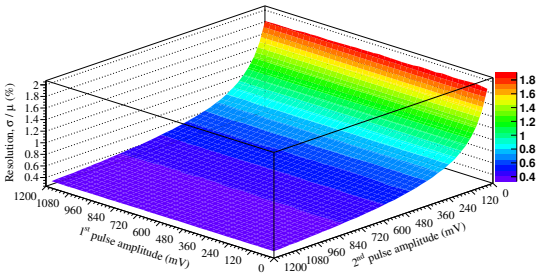


*Figure 5.16: The recovered second-pulse energy resolution ($\sigma$ / $\mu$ ) in % as a function of the amplitude of the first and the second pulse.*

as a function of the amplitude of the first and the second pulse is shown in Fig. 5.16. In the shown coordinate system, the x-axis is the first-pulse amplitude, the y-axis is the second-pulse amplitude, and the z-axis is the energy resolution obtained for the second pulse. The energy resolution improves as a function of the second-pulse amplitude. The relative difference $[(\sigma_{rec} - \sigma_{ref})/\sigma_{ref}]$ between the recovered ($\sigma_{rec}$) and reference ($\sigma_{ref}$) energy resolution as a function of the amplitude of the first and second pulse is shown in Fig. 5.17. The resolutions can be recovered for all investigated combinations of amplitudes of the first and second pulse in the range from 70 mV to 1100 mV. The relative difference is

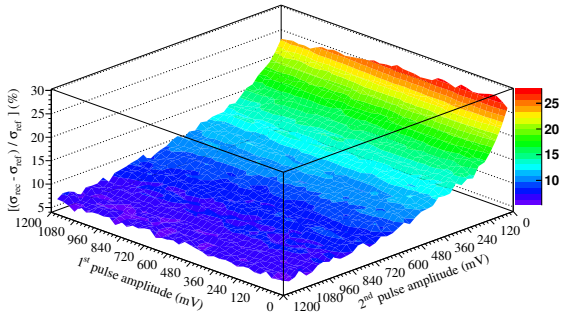


*Figure 5.17: The relative difference* $[(\sigma_{rec} - \sigma_{ref})/\sigma_{ref}]$ *between the recovered* $(\sigma_{rec})$ *and reference* $(\sigma_{ref})$ *energy resolution as a function of amplitude of the first and second pulse.*

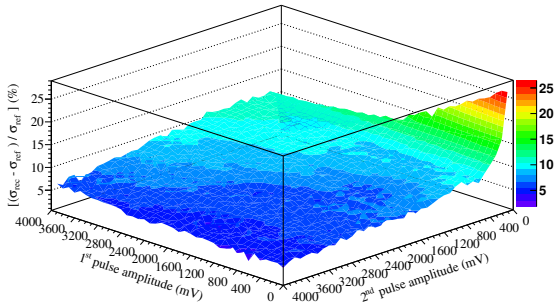


*Figure 5.18: The relative difference* $[(\sigma_{rec} - \sigma_{ref})/\sigma_{ref}]$ *between the recovered* $(\sigma_{rec})$ *and reference* $(\sigma_{ref})$ *energy resolution as a function of amplitude of the first and second pulse over the larger dynamic range of* 1000 (3.8 V/3.8 mV).

almost independent of the first-pulse amplitude at a given second-pulse amplitude and it is inversely proportional to the second-pulse amplitude. The maximum deviation is seen at the lowest pulse amplitudes, while at higher amplitude values less deviation is obtained. Since the PANDA EMC will be operated in a large dynamic energy range of up to 10,000, the equivalent graph of relative differences in resolutions as a function of the amplitude of the first and the second pulse is

shown in Fig. 5.18 for a larger dynamic amplitude range of 1000 (3.8 V/3.8 mV). The relative difference plotted on the vertical axis follows the same trend over the larger dynamic range as seen in Fig. 5.17. The fluctuations are caused by numerical effects. Due to the small values of $\sigma_{ref}$, the relative difference is very sensitive to fluctuations and, therefore, to rounding errors. Nevertheless, these plots provide a reasonable estimate of the recovery precision. Once again, the maximum deviation is seen at the lowest pulse amplitudes. The relative difference decreases with the increase in pulse height. Therefore, the results obtained in the investigated dynamic range of 1000 may be safely used as upper limits for the required larger dynamic range of 10,000.

### Pulse pile-up for 5×5 cluster

To simulate pulse pile-up in a cluster of twenty five ($5 \times 5$) scintillating crystals, that may respond to a single high-energy photon, we have used analysis results obtained with the charge-integrating (QDC) readout of the sixty-crystal EMC prototype (proto60) [64] experiment. In the proto60 experiment, the energy-tagged photons were used to study the detector response. Two examples of the photon energy-deposition spectrum are shown in Fig. 5.19 in the top and bottom panels [64] for incident photon energies of 150 MeV and 1.4 GeV, respectively. We observe 80% of the incident photon energy deposition in the central crystal, 15% in the first ring, i.e. the eight neighboring crystals of the central crystal, and 5% in the second ring, i.e. the sixteen neighboring crystals of the first ring. These results were considered while introducing two additional pulses into the measured trace digitized by the SADC. These pulses were generated using the response function shown in equation 5.1 and fed into the measured trace over a time difference interval of 50 ns $< \Delta\tau <$ 280 ns (Fig. 5.12) for all detectors in the $5 \times 5$ cluster. Using the measured first-pulse signal has the advantage that the proper electronic noise is included in the pile-up simulation. The simulated $5 \times 5$ cluster energy-deposition spectrum is shown in Fig. 5.20. To study the energy recovery of pile-up pulses over the cluster, the simulations were done for various photon energies ranging from 50 MeV to 1.4 GeV of the second pulse while the first-pulse energy was about 300 MeV. The $5 \times 5$ cluster energy spectrum was fitted using an asymmetric Gaussian fit function [120] to obtain the peak

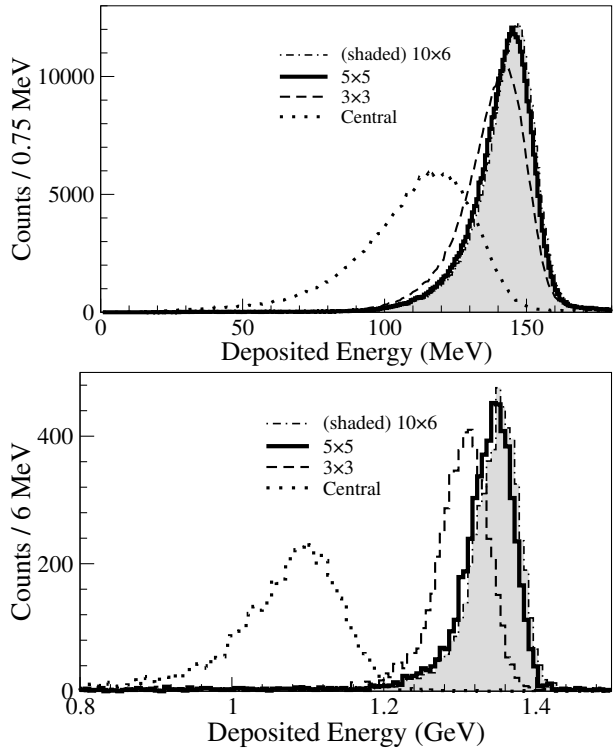


*Figure 5.19: Measured photon energy-deposition spectrum for incident photon energies of 150 MeV (top panel) and 1.4 GeV (bottom panel), obtained with the charge-integrating (QDC) readout of the sixty-crystal EMC prototype (proto60) [64] experiment. The energy depositions in the central crystal and the* $3 \times 3$*,* $5 \times 5$*, and* $10 \times 6$ *crystal matrices are indicated by the dotted line, the dashed line, the solid line, and the shaded area, respectively.*

position and Full Width at Half Maximum (FWHM). The energy resolution as a function of the photon energy is shown in Fig. 5.21. The energy resolution is defined as (FWHM/2.35)/(peak position). If the addition of the contributing terms in the fit function is done in quadrature ($\oplus$) (see section 4.1.3), the fit-parameter values are larger e.g., a simple addition of $0.68\% + 0.20\%/(\mathrm{E/GeV}) + 1.52\%/\sqrt{(\mathrm{E/GeV})}$ results in 2.4% at 1 GeV and the addition in quadrature of $1.12\% \oplus 0.3184\%/(\mathrm{E/GeV}) \oplus 2.089\%/\sqrt{(\mathrm{E/GeV})}$ (fit not shown in figure) results

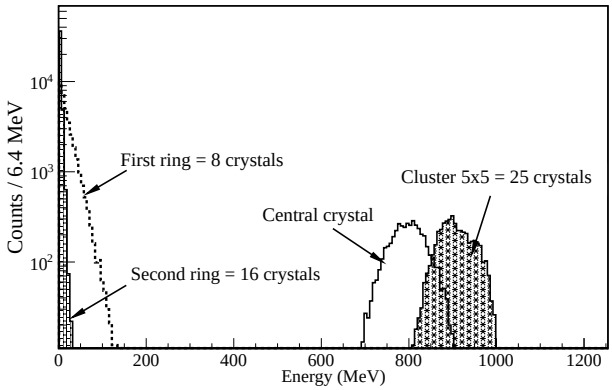


*Figure 5.20: Simulated* $5 \times 5$ *cluster energy deposition spectrum for single pulses at 1 GeV photon energy. The energy depositions in the central crystal, the first ring of crystals, the second ring, and the* $5 \times 5$ *crystal matrix are indicated by the solid line, the dashed line, the shaded area with bricks and the shaded area with stars, respectively.*

in 2.4% at 1 GeV. However, in the given fit range the shape of the fit function does not change significantly. The $5 \times 5$ cluster simulation produces an energy resolution close to the values obtained for proto60 [64]. The reference $5 \times 5$ cluster energy resolution shows better resolution values for high-energy photons than the $3 \times 3$ cluster SADC data because of the $5 \times 5$ cluster summation. The pile-up recovered cluster energy resolution is only 20% worse than the non-pile-up cluster energy resolution.

### Pulse pile-up for two overlapping 5×5 clusters

In order to determine the impact of pile-up recovery on the effective energy resolution, we studied overlapping clusters of photons and the probabilities for certain overlap situations. The effective energy resolution is the resolution of the properly weighted sum of single-pulse energies and pile-up recovered energies for a $5 \times 5$ cluster. To generate pulse pile-up in the overlapping regions of two neighboring clusters, two symmetric $5 \times 5$ clusters were simulated as described in the previous section. These two clusters were named cluster-1 and cluster-2 as shown in Fig. 5.22. The crystal marked by 0 in both clusters re-

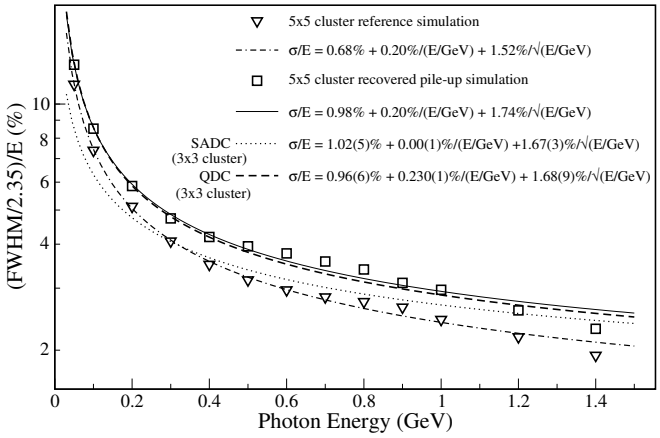


*Figure 5.21: Energy resolution for the pile-up recovered second-pulse as a function of photon energy. The triangles are the reference resolution for the* $5 \times 5$ *cluster and the dash-dotted line is the corresponding fit. The squares are the pile-up recovered resolution for* $5 \times 5$ *clusters and the solid line is the corresponding fit. The dashed line is the* $3 \times 3$ *cluster resolution for QDC readout and the dotted line is the* $3 \times 3$ *cluster resolution for SADC readout (data from [64]).*

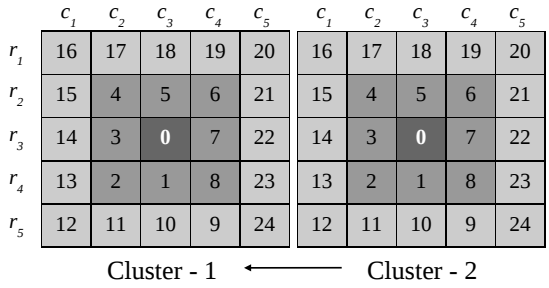


*Figure 5.22: Schematic representation of two symmetric* $5 \times 5$ *clusters. The letters* $c_1$, $c_2$, $c_3$, $c_4$, *and* $c_5$ *indicate the columns and* $r_1$, $r_2$, $r_3$, $r_4$, *and* $r_5$ *indicate the rows of the symmetric* $5 \times 5$ *cluster.*

ceives the highest energy deposition in comparison with its neighboring crystals and hence it is called "seed". The photon energy distribution for the forward endcap EMC was simulated using the Dual Parton Model (DPM) background

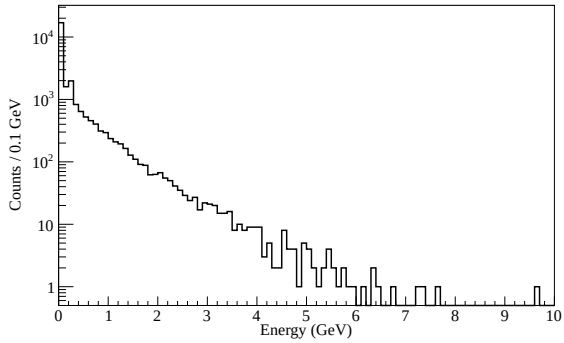


*Figure 5.23: The photon energy distribution for the PANDA forward endcap EMC simulated using the DPM background generator at $\bar{p}$ beam momentum of* 15 GeV.

generator [121] embedded in the PandaRoot software package [122]. In the DPM generator, $p\bar{p}$ inelastic scattering produces a parton shower forming mesons and baryon resonances ($\pi^0$, $\eta$, $\Delta$, $\Sigma$, etc.) which further decay within the volume of the detector. The simulated photon energy distribution shown in Fig. 5.23 was used as input for the energy deposition in cluster-1. The input energy deposition for cluster-2 was varied from 50 MeV to 1.4 GeV at time differences relative to cluster-1 randomly chosen from 50 ns to 280 ns and the pile-up pulses were simulated in the overlapping regions of $5 \times 5$ clusters.

To simulate overlapping regions where the pulse pile-up will occur, cluster-2 was moved in steps of one column in the direction of the arrow towards cluster-1 (see Fig. 5.22). If the first column ($c_1$) of cluster-2 overlaps the last i.e. the fifth column ($c_5$) of cluster-1, the distance between the seeds of cluster-1 and cluster-2 is four crystals and hence this situation is called "seed distance-4 ($s.d.4$)". Accordingly, the overlapping situations for the remaining four columns were defined as "seed distance-$n$ ($s.d.n$)", $n = 0$ to 3, with $n = 0$ for complete overlap. The energy resolution for the pile-up recovered second pulse as a function of the energy is shown in Fig. 5.24. The pile-up recovered energy resolution for the seed distance-3 and 4 produces energy resolutions almost equal to the reference energy resolution. The relative difference between the reference energy resolution and the recovered energy resolution for seed distance-0 is about 20%. In the simulation above, we have considered the worst-case scenario in which the

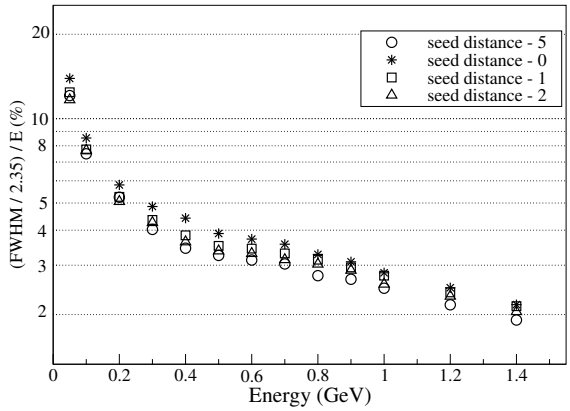


*Figure 5.24: Energy resolution for the pile-up recovered second pulse as a function of the energy. The circles indicate the reference energy resolution for a* $5 \times 5$ *cluster without any overlap or pile-up. The seed distance-2 (triangles), seed distance-1 (squares), and seed distance-0 (stars) indicates the pile-up recovered second-pulse energy resolution for the overlapping columns of both the showers.*

two $5 \times 5$ clusters were shifted against each other in the horizontal direction. In this way we obtained the largest overlap of single-crystal hits for a particular seed distance. Therefore, the presented simulation provides a conservative estimate of the pile-up effect on the final performance of the EMC.

The geometry of the forward endcap EMC was taken into account to estimate the overlap-occurrence probabilities of the five selected cases. In order to obtain a worst-case estimate, we chose the region of highest hit rates with polar angle $\theta$ between 5° and 10° (see Fig. 5.1). The probability of a second photon hitting a certain position in the overlap region is proportional to $P_{(s.d.n)} = P_{r_i(c_i+c_j-1)}(\theta_i)$, where $i$ and $j$ $(1 \leq i,\ j \leq 5)$ are the hit position indices of cluster-1 and cluster-2, respectively, generating overlap at five representative seed distances. For a fixed seed distance the hit probability for each relevant crystal depends on the polar angle. The probability is $P_{r_i c_i}(\theta_i) \sim \left(\frac{1}{N(\theta_i)}\right)$, where $N(\theta)$ is the number of crystals located at the polar angle $\theta$.

We assume that the first photon hits the EMC at a fixed position $c_3$ $r_3$ (see

Fig. 5.22) in one of the $5 \times 5$ clusters with probability proportional to $P_{r_3c_3}$. The probability of a second photon hitting one of the nearest neighbors for the case of seed distance-1 ($s.d.1$) is defined by $P_{(s.d.1)}$:

$$P_{(s.d.1)} = \sum_{i=2,4} P_{r_3c_i} + \sum_{i=2}^{4} (P_{r_4c_i} + P_{r_2c_i}) \tag{5.2}$$

Similarly, the probabilities of a second photon hitting in the vicinity of the first hit for the other cases were evaluated. The resulting normalized overlap probabilities for the case $s.d.0$ to $s.d.4$, exhausting all possible worst-case pile-up cases, are 1%, 9%, 19%, 30%, and 41%, respectively. Hence the probability of complete shower overlap ($s.d.0$) is almost negligible compared to the rest.

In the peripheral overlap region the pile-up of low-energy pulses will occur. According to Fig. 5.17 the maximum difference between the pile-up recovered and the reference energy resolution was seen at the lowest pulse amplitudes. However, the effective energy resolution for a $5 \times 5$ cluster for peripheral overlap including the slight deterioration due to the pile-up recovery, is almost not affected. The resulting energy resolution for the endcap, obtained by averaging the properly weighted energy resolutions shown in Fig. 5.24, only slightly deteriorates. For example, the pile-up free energy resolution at 1 GeV is 2.48%, the effective energy resolutions for EMC hit rates of 1 MHz and 500 kHz are 2.50% and 2.49%, respectively.

### 5.3.5 Time recovery

The time stamp of the pulse was estimated using the Constant Fraction Timing (CFT) method [64]. This is realized using an algorithm that is described by equation 5.3. In this method, a fraction $f$ of the pulse amplitude is inverted and added to the pulse, after being delayed by the rise time of the pulse.

$$\begin{aligned} I[i] &= -f\ (S[i] - Bl), \\ CFT[i] &= I[i] + (S[i - D] - Bl). \end{aligned} \tag{5.3}$$

In equation 5.3, $I[i]$ is the attenuated and inverted pulse amplitude for sample $i$, $f$ is the attenuation constant or fraction of the pulse amplitude, $S[i]$ is the raw digitized data at sample $i$, $Bl$ is the baseline, $CFT[i]$ is the CFT signal, and $D$ is the time delay. The CFT algorithm was applied at the leading edge to obtain the time stamp $t_1$ of the first pulse. Equivalently, to obtain the time $t_2$ of the second pulse, the CFT algorithm was applied at the trailing edge. This approach implies using the measured data in the time-reversed order to obtain $t_2$. An example of a digitized raw pulse and the CFT signal is shown in Fig. 5.25 (a) and (b), respectively. In Fig. 5.25 (b) the linear interpolation (solid line) was applied to estimate the zero-crossing point (dashed line), which defines the time-stamp of the second pulse.

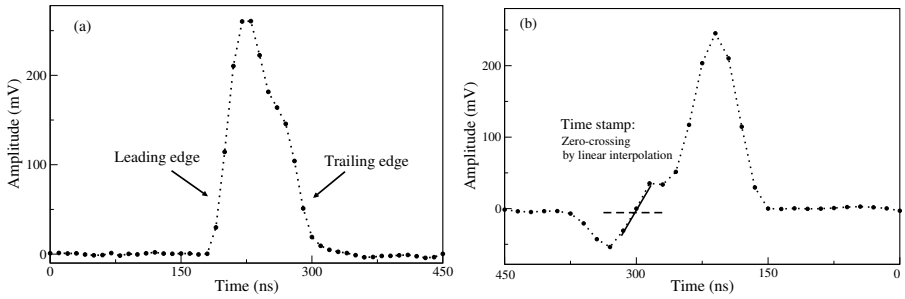


*Figure 5.25: (a) An example of a digitized pile-up pulse. (b) The CFT signal constructed using the time-inverted data to extract the trailing-edge timing for the second pulse in the pile-up structure. A linear interpolation was applied to find the zero-crossing point which defines the time stamp of the second pulse.*

The time difference between trailing and leading edge is defined as the *recovered* time difference ($\Delta\ T$). In order to characterize the performance of the algorithm we introduce a reference time difference $\Delta\tau\ =\ t_2 - t_1$ (see section 5.2.1). It is known only for the performed simulation and validation experiment. The subtraction of the reference time difference ($\Delta\tau$) from the recovered time difference ($\Delta\ T$) results in the difference ($\Delta\ T - \Delta\tau$) which is equivalent to the pulse width and is expected to be constant because the pulse shape was found to be constant. The obtained pulse width as a function of $\Delta\tau$ for different values of the CFT parameter time delay $D$ is shown in Fig. 5.26. For larger values of $D$, the

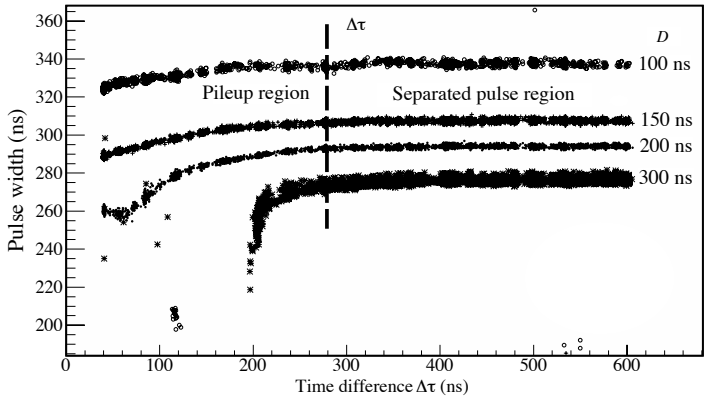


*Figure 5.26: The pulse width ($\Delta\ T - \Delta\tau$) as a function of the time difference $\Delta\tau$ for different values of the CFT time delay parameter $D$ for an amplitude ratio 2. The region $\Delta\tau\ <$ 280 ns is the pile-up region where the pulse width is not constant due to the asymmetric pile-up pulse shape.*

trailing-edge zero-crossing point moves closer to the leading-edge time-stamp and the recovered time difference ($\Delta\ T$) decreases. Hence, the absolute value of the time difference ($\Delta\ T - \Delta\tau$) or pulse width decreases with CFT parameter $D$ (see eq. 5.3). In the region $\Delta\tau > 280$ ns the pulse width is constant as expected for a well separated pulse. The region $\Delta\tau < 280$ ns is the pile-up region where the measured pulse width is not constant due to the overlap of the second pulse at the trailing edge of the first pulse. This resulting distortion is amplified by the asymmetric pulse shape. Due to this effect it is almost impossible to recover the time stamp in the pile-up region.

To symmetrize the asymmetric pulse shape, we have applied the Moving Window Deconvolution (MWD) [64, 123, 124] filter on the digitized raw pulse. The MWD filter is expressed by:

$$\mathrm{MWD_M(n)} = x(n) - x(n-M) + \frac{1}{\tau} \sum_{i=n-M}^{n-1} x(i), \tag{5.4}$$

where $M$ is the length of the filter, $\tau$ is the decay time of the signal, and $x(n)$ is the $n^{th}$ input sample. The MWD filter differentiates the raw signal with the

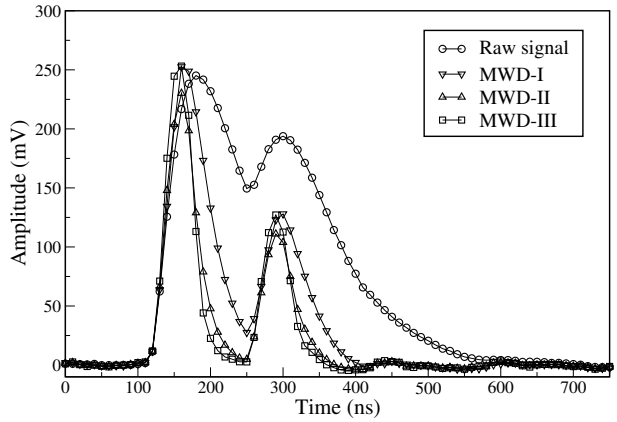


*Figure 5.27: The comparison of the raw digitized and MWD filtered pulse shapes. Circles: raw pulse shape at* $\Delta\tau = 100$ ns *for the amplitude ratio 2, triangles down: MWD applied once (MWD-I), triangles up: MWD applied twice (MWD-II), squares: MWD applied three-times (MWD-III). After MWD-III, the pile-up pulses appear as two separated single pulses with a more symmetric shape.*

length ($M$) of the filter and compensates for the exponential decay of the signal using the decay time $\tau$. Thus, the MWD filter cancels the semi-exponential tail of the shaped pulse. The resulting pulse shape is shown in Fig. 5.27. A single MWD filtering can not completely compensate the tail of the pulse, as it does not have the perfect exponential behavior. After applying the MWD filter two times, the tail at the trailing edge is still visible. Hence we have applied the MWD filter three times (MWD-III) in order to obtain pile-up pulses appearing as two separated single pulses with a symmetric shape. The pulses obtained after the MWD-III filter were used to apply the time recovery algorithm. The corresponding filter parameters are shown in Table 5.1. For each MWD filter the parameter $M$ was chosen to be slightly larger than the pulse width in order not to affect the pulse amplitude. The values of the decay-time parameter $\tau$ were deduced from the exponential fit of the trailing edges of the pulses at each filtering step. The same pulse shape can be achieved by different combinations of the $M$ and $\tau$ parameters. Since the pulse shape is symmetric, we expect the measured pulse width ($\Delta\ T - \Delta\tau$) to be constant. The resulting distribution of the pulse width as a function of $\Delta\tau$ is shown in Fig. 5.28 ($a$). The pulse width

| Parameter | Filter type | | |
|---|---|---|---|
| | MWD-I | MWD-II | MWD-III |
| $M$ (ns) | 40 | 20 | 20 |
| $\tau$ (ns) | 80 | 30 | 20 |

*Table 5.1: The parameter values used to generate symmetric pulse shapes by MWD filtering.*

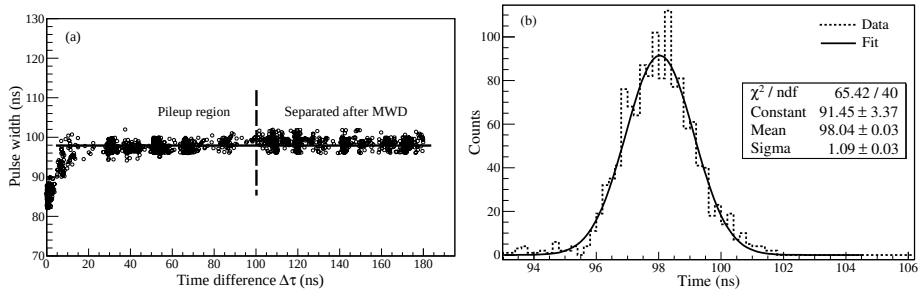


*Figure 5.28: (a) The pulse width ($\Delta\ T - \Delta\tau$) versus time difference $\Delta\tau$. The pulse width is constant (solid horizontal line) above $\Delta\tau = 10$ ns. The vertical dashed line separates the pile-up region from the region where pulses are separated after the MWD filter. (b) The projection onto the vertical axis of Fig. (a) above $\Delta\tau = 10$ ns. The pulse-width distribution is fitted with a Gaussian function (solid line). The obtained uncertainty ($\sigma$) or the average time resolution is $\approx 1$ ns for the amplitude ratio 2.*

obtained is constant above $\Delta\tau = 10$ ns. The projection onto the vertical axis of Fig. 5.28 ($a$) above $\Delta\tau = 10$ ns is shown in Fig. 5.28 ($b$). The uncertainty ($\sigma$) of the pulse-width distribution is defined as the time resolution for the pile-up pulses. The obtained average time resolution is $\approx 1$ ns for the amplitude ratio 2. The same procedure is repeated for various amplitude ratios (first-pulse amplitude / second-pulse amplitude). The result of the averaged time resolution as a function of the amplitude ratio is shown in Fig. 5.29. The reference pulse resolution (triangles) is compared with the recovered pulse resolution (circles). The maximum deterioration of the time resolution is about a factor 2.

The effect of the MWD filter on the energy resolution is shown in Fig. 5.30, obtained for a single simulated pulse amplitude of 250 mV. The energy resolution

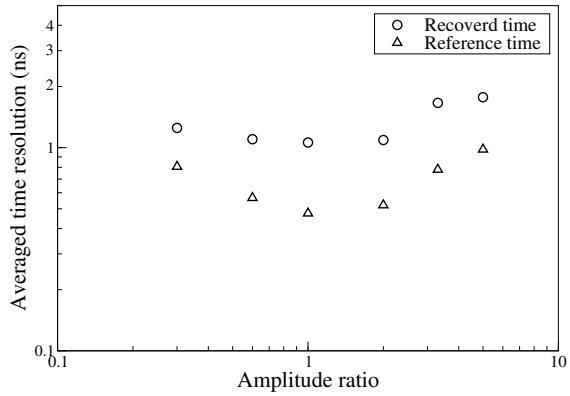


*Figure 5.29: The comparison of the averaged time resolution of the recovered (circles) and the reference pulse (triangles) as a function of the amplitude ratio. The amplitude ratio of 2 corresponds to a first-pulse amplitude of* 250 mV *and a second-pulse amplitude of* 125 mV *and the second-pulse amplitude is varied. Significant time recovery is obtained. Both axes are plotted on log scale.*

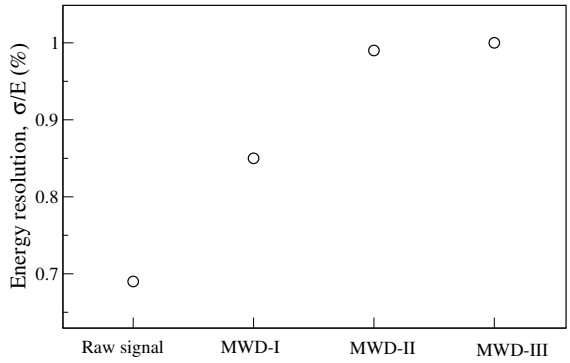


*Figure 5.30: The energy resolution obtained for a single simulated pulse amplitude of* 250 mV *as a function of the signal type without filter (raw) or after the MWD filter of level I to III.*

gets worse due to the application of the MWD filter onto the digitized signal. Thus, the MWD filter will not be used for energy recovery of pile-up pulses.

### 5.3.6 Simulation studies for time recovery

Simulations were done to study the performance of the time recovery method over a large dynamic energy range. The procedure described in section 5.3.4 was followed to generate pile-up pulses. However, in the wide dynamic amplitude range the pile-up region with full recovery of the pulse width (see Fig. 5.28) is limited to time differences $\Delta\tau >$ 50 ns because otherwise the second pulse, after the MWD filter, can not be safely separated for all amplitude combinations.

Equation 5.1 was used to introduce two additional pulses into the measured signal trace with a time difference chosen in an interval of 50 ns $< \Delta\tau <$ 100 ns. The time recovery method has been described in the previous section where the MWD-III filter was used to obtain a symmetric pulse shape as seen in Fig. 5.27. Due to the MWD-III filter the pulse width was reduced to $\sim$ 100 ns. Thus the maximum time difference of 100 ns was used to simulate pulse pile-up. To obtain the time stamp, the CFT method was applied to the leading edge of the first pulse and to the trailing edge of the second pulse in the pile-up structure. The time difference between trailing-edge and leading-edge time stamps is called the *recovered* time difference (section 5.3.5). The recovered time resolution $\sigma_{rec}$ as a function of the first and the second-pulse amplitude over a large dynamic energy range of $\sim$ 1000 (7 V/7 mV) is shown in Fig. 5.31. The recovered time resolution $\sigma_{rec}$ shown on the vertical axis is obtained from the variance of the

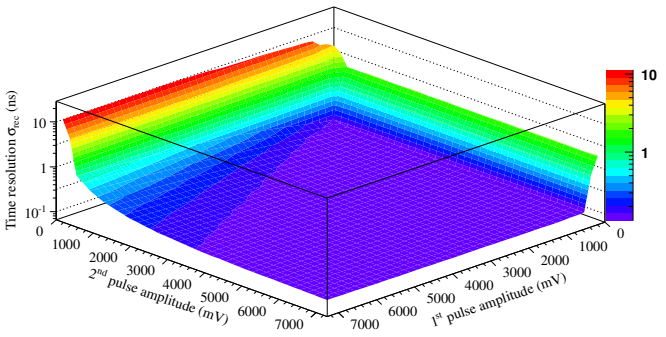


*Figure 5.31: The pile-up recovered time resolution $\sigma_{rec}$ as a function of the first and the second-pulse amplitude over a large dynamic range of* $\sim$ 1000 (7 V/7 mV).

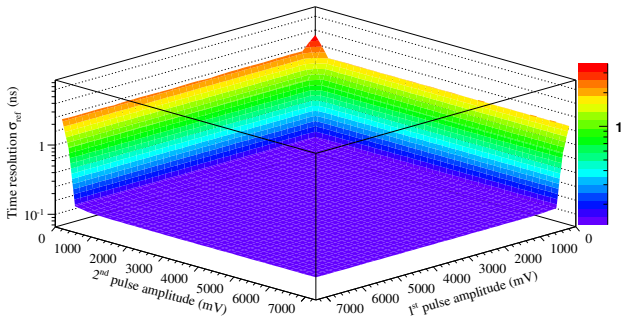


*Figure 5.32: The time resolution $\sigma_{ref}$ of the well separated pulses as a function of the first and the second-pulse amplitude over a large dynamic range of* $\sim 1000$ (7 V/7 mV).

time difference distribution obtained by subtracting the recovered time difference and the true time difference. The time resolution improves as a function of the second-pulse amplitude.

The same simulation procedure and the time-recovery method have been applied on pulses well separated in time, obtained by adding two pulses with a time difference chosen in an interval of 300 ns $< \Delta\tau <$ 350 ns. The resulting time resolution $\sigma_{ref}$ is plotted as a function of the first and the second-pulse amplitudes in Fig. 5.32. The time resolution for well-separated pulses improves as a function of both the pulse amplitudes.

The relative difference $[(\sigma_{rec} - \sigma_{ref})/\sigma_{ref}]$ between the recovered ($\sigma_{rec}$) and the reference ($\sigma_{ref}$) time as a function of the first and second-pulse amplitude over a large dynamic range of $\sim$ 1000 (7 V/7 mV) is shown in Fig. 5.33. The largest deviation is seen at the lowest second-pulse amplitudes, while at the lowest first-pulse amplitudes the deviation is well below 1%. The MWD-III filter plays an important role in the region of low amplitudes of the second pulse. If the first-pulse amplitude is very high, e.g. 7 V, and the second-pulse amplitude is less than about 100 mV, the MWD-III filter is unable to reconstruct the second-pulse amplitude, resulting in the maximum deviation in the relative difference. Conversely, if the first-pulse amplitude is low and the second-pulse amplitude

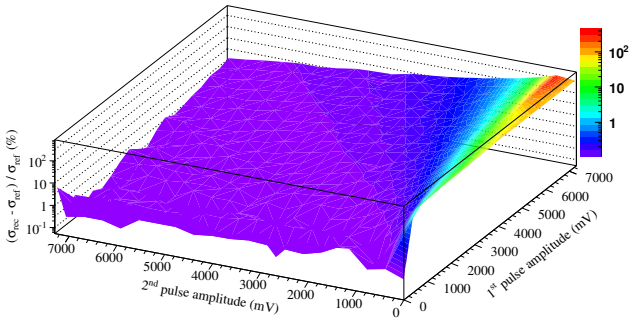


*Figure 5.33: The relative difference* $[(\sigma_{rec} - \sigma_{ref})/\sigma_{ref}]$ *between the recovered* ($\sigma_{rec}$) *and reference* ($\sigma_{ref}$) *time as a function of the first and second-pulse amplitude over a large dynamic range of* $\sim 1000$ (7 V/7 mV).

is high, then the MWD-III filter recovers the second pile-up pulse resulting in smaller deviations.

### 5.3.7 Pile-up probability

The Poisson distribution function is commonly used to estimate the number of events occurring in a given time interval. Therefore, the pile-up probability was estimated using a Poisson time-distribution function:

$$P[k;(r \cdot w)] = \frac{(r \cdot w)^k e^{-(r \cdot w)}}{k!} \tag{5.5}$$

where $r$ is the hit rate for the EMC, $w = 280$ ns is the pulse length used in the test experiment (see section 5.2.1), $k$ is the number of occurrences of the events within a time interval equal to the pulse width $w$. The pile-up probability for $k = 1$ as a function of the EMC hit rate is shown in Fig. 5.34. The pile-up probability at a hit-response time of 280 ns is rather high and is significantly reduced using the proposed pile-up recovery method by recovering features of all pulses arriving after a time delay of about 50 ns. Due to the hydrogen pellet target fluctuations, the most forward region ($\theta = 5°$ to $7°$) of the forward endcap

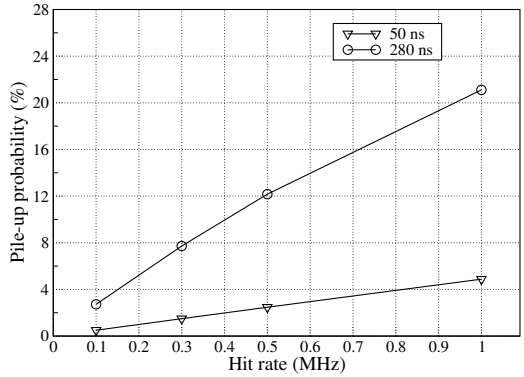


*Figure 5.34: The pile-up probability as a function of the EMC hit rate estimated using a Poisson time-distribution function. The circles indicate the pile-up probability at a hit-response time of* 280 ns *and the triangles indicate the remaining pile-up probability after pile-up recovery for an effective hit-response time of* 50 ns.

EMC will be exposed to a peak hit rate of 1 MHz resulting in a pile-up probability of 21%. After applying the recovery method, the remaining pile-up probability is reduced to 4.2%. Similarly, at hit rates of about 500 kHz the pile-up probability is about 12%. The reported pile-up recovery method can reduce this probability to 2.4%.

For the pulse-length of 280 ns, the pile-up probability is about 21% at 1 MHz detector hit-rate. This means that, out of 1 million events, 21% i.e $2.1 \cdot 10^5$ events will be pile-up events. The digitizers for the PANDA EMC will be operated at a sampling rate of 80 MHz corresponding to a sample period of 12.5 ns. Therefore, as a worst-case estimate for a maximum pile-up waveform length of about 560 ns, the rate of samples contributing to the pile-up will be $2.1 \cdot 10^5 \cdot 560$ / 12.5 $= 9.4 \cdot 10^6$ samples/s (9.4 MHz per SADC channel). The pile-up recovery will be done on-line inside the FPGAs of the Data Concentrator (DC) module (see Fig. 4.10). Each of these FGPAs disposes of several units of reusable logic cells called Intellectual Property Core (IPC). The PANDA EMC readout chain is based on the pipeline design where each clock accesses one data sample. The clock speed (i.e. the rate at which the processor can complete a processing cycle) of the Xilinx Virtex-5 FPGA used in the DC module is about

500 MHz [107]. At this clock speed, a single IPC of an FPGA can process pile-up waveforms for almost 54 SADC channels (9.4 MHz per channel) at a detector hit rate of 1 MHz. A single DC can digest data from 8 digitizer modules which will have 32 readout channels. Therefore, in total only 5 IPCs will be needed for processing the pile-up waveforms, which can be easily achieved using the PANDA EMC readout-chain.

## 5.4 Summary and conclusion

A pulse pile-up recovery method is developed and tested for the front-end electronics of the PANDA EMC. It allows to recover the pulse amplitude completely with a minimum time difference equal to the pulse rise-time. The pile-up probability of 21% is reduced to 4.2%. Pile-up simulations are done to study the energy recovery over a large dynamic energy range of 1000. It is seen that the relative difference in recovered and reference energy resolution is almost independent of the first-pulse amplitude and it is inversely proportional to the second-pulse amplitude. The maximum deviation is seen for the lowest pulse amplitudes, while at higher amplitude values less deviation is obtained.

The simulation studies for the $5 \times 5$ cluster energy recovery reproduce the energy resolution values obtained for the prototype experiment proto60. The pile-up recovered cluster energy resolution is at most 20% worse than the pile-up free cluster energy resolution. Similarly the overlapping-shower simulation studies have shown that the recovered energy resolution for the peripheral overlap produces energy resolutions almost equal to the pile-up free reference energy resolution. The difference between the reference energy resolution and the recovered energy resolution for maximum overlap is about 20%. The estimated probabilities for the occurrence of two overlapping showers vary from 1% to 41% from maximum to peripheral overlap, respectively. The effective energy resolution, obtained by properly weighting the pile-up recovered energy resolutions and the reference energy resolutions for a $5 \times 5$ cluster, reveals only little deterioration, e.g., at 1 GeV and for an EMC hit rate of 1 MHz a change from 2.48% to 2.5% is observed.

The CFT method is applied at the trailing edge of the pile-up pulse. The tail

at the trailing edge plays an important role in the time recovery. The MWD filter is applied three times to remove the tail at the trailing edge and to obtain an almost symmetric pulse shape. Simulations were done to study the time recovery over a wide dynamic range of 1000. The systematic behavior of the observed results allows a safe extrapolation to the required dynamic range of 10,000. In the lowest second-pulse amplitude region, the MWD-III filter is unable to reconstruct the second-pulse amplitude accurately, resulting in a large deviation in the relative difference in time resolution. Conversely, in the lowest first-pulse amplitude region the MWD-III filter recovers the second pile-up pulse, resulting in a small deviation and significant recovery of time resolution.

The reported method for energy and time recovery is simple and effective and could be easily implemented in FPGAs. Due to the simplicity of the method the processing will require little FPGA resources and eventually consume less power. The pile-up identification algorithm has already been implemented in FPGA and its on-line performance studies with the tagged photon beam will be discussed in detail in the next chapter.

# Chapter 6

# Performance Test

***Part of this chapter is published as: "Trigger-Less Readout of the PANDA Electromagnetic Calorimeter", M. Kavatsyuk et al. (G. Tambave), in Conf. Record, NSS IEEE 2012, Oct. 29 - Nov. 3, 2012, Anaheim, California, USA.***

The on-line performance test of the PANDA EMC prototype readout chain, discussed in chapter 4, was needed to improve and finalize the ongoing hardware and firmware development for the PANDA experiment. The pile-up recovery algorithm, discussed in chapter 5, was tested off-line on simulated and measured pile-up waveforms generated using an LED light pulser. It was necessary to validate the performance of the recovery algorithm with high-rate data obtained from the realistic detector response. In this context, the PANDA EMC prototype of nine PWO-II crystals (proto9) was built at KVI to test the performance of the EMC readout-chain prototype and the pile-up recovery algorithm.

This chapter is dedicated to the proto9 design and its performance test carried out using tagged photons at the MAMI accelerator facility in Mainz, Germany. Section 6.1 describes the design and development of proto9, its front-end electronics and data acquisition system. The experimental setup designed for the test experiment at Mainz is explained in section 6.2. The data analysis, the results

and a discussion of the performance test of the readout chain and of the pile-up recovery algorithm are presented in section 6.3. A summary and conclusions are given in section 6.4.

## 6.1 EMC prototype (proto9)

Proto9 was built using nine PWO-II crystals (see section 4.2.2) which are developed for the geometry of the forward endcap EMC. These crystals were wrapped inside reflecting foil for optimal collection of the reflected scintillation light. A photograph of PWO-II crystals wrapped in the reflecting foil is shown in Fig. 6.1 (a). All nine wrapped crystals were inserted inside a carbon-fiber alveole, specially designed for holding sixteen PWO-II crystals. The remaining space was filled using seven brass bars, cut in the same size as the crystals, to stabilize

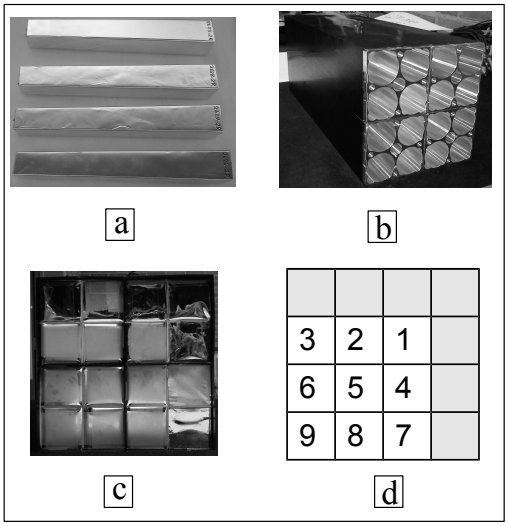


*Figure 6.1: Photograph: (a) PWO-II crystals wrapped in reflecting foil, (b) A backside view of the subunit showing the carbon-fiber alveole and aluminum inserts, (c) A front view of the subunit showing the matrix of nine wrapped PWO-II crystals and seven brass bars inserted in the top row and the right side column, (d) Mapping of the crystals.*

the alveole. The alveole holding all the crystals and bars is called a subunit. A photograph of such a subunit is shown in Fig. 6.1 (b) and (c), seen from the backside and from the front side, respectively. Figure 6.1 (d) shows the mapping of the crystal positions and their numbering. To collect the scintillation light produced by tagged photons, rectangular APDs (see section 4.2.2) were used as photosensors. Two of these APDs were optically coupled to each crystal. In order to amplify the APD signals, a dedicated pre-amplifier (see section 4.2.3) was developed at KVI. The pre-amplifier has two inputs and four outputs for each input channel for high gain and low gain, respectively. The test of a newly developed first version of this pre-amplifier was one of the goals of this experiment. One pre-amplifier per each PWO-II crystal was used to readout two APDs. In this way in total eighteen APDs and nine pre-amplifiers were used for nine PWO-II crystals. A plastic capsule shown in Fig. 6.2 (a) and (b) was designed to hold a pair of APDs and the pre-amplifier. Two sockets, made for mounting two APDs, are visible in the front view of the capsule in Fig. 6.2 (a). A side view of the capsule in Fig. 6.2 (b) shows a simple arrangement to connect a pre-amplifier to the APDs and the pre-amplifier heat-removing arrangement. The pre-amplifier was placed on gap-pad material [125] and the excessive heat was removed using a copper plate placed below the gap-pad. The copper plate was soldered to a thick copper mesh routed outside of the subunit to the cooled mounting plate of the subunit. In this way nine capsules were equipped with all the components. An aluminum insert, seen from the backside of the subunit in Fig. 6.1 (b), has cylindrical openings to insert all nine fully equipped capsules from the APD end. Fig. 6.2 (c) shows a backside view of the subunit after insertion of the capsules and various cables together with the copper mesh. The cables include the pre-amplifier power supply and output signal cables and APD high-voltage supply cables. Optical fibers are inserted to shine light from an LED light pulser into the crystals and metal springs are used to press the APDs against the crystal face.

The complete subunit was mounted on a 10 mm thick aluminum mounting plate. To cool the subunit, chilled [126] alcohol (at $-34°$C) was flown through a 5 mm diameter metal pipe soldered onto the backside of the aluminum mounting plate. The aim was to cool the PWO-II crystals to $-25°$C to improve the light yield (see section 4.2). This was achieved by keeping the subunit with its

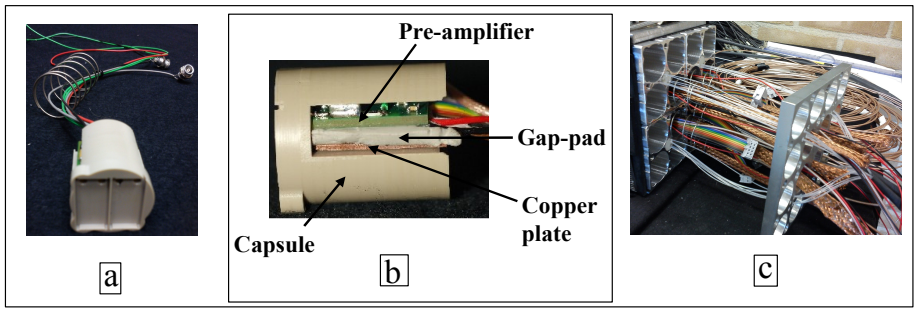


*Figure 6.2: Photograph: (a) A capsule specially designed for holding APDs and the pre-amplifier, (b) A side view of a capsule showing the pre-amplifier placed on top of the gap-pad and the copper plate, (c) A back view of a subunit with completely equipped capsules inserted from the APD side into the aluminum insert.*

mounting plate inside a thermally-insulated detector box ($40 \times 40 \times 100$ cm$^3$). To keep the humidity below 10% and hence to avoid condensation inside the box, a continuous flow of dry nitrogen gas was circulated throughout the cold-box volume. After a successful test of all the pre-amplifier signals and the temperature stability, the proto9 setup was installed for the test experiment.

## 6.2 Experimental setup

The performance of the proto9 setup was assessed using a tagged-photon beam produced by the tagger spectrometer of the Mainz Microtron (MAMI) accelerator facility [127] located in Mainz, Germany. The floor plan of the MAMI accelerator facility (Fig. 6.3) shows the electron source, the tagger system [128], and the location of the experimental hall (A2) where the proto9 was mounted. The maximum electron beam energy at the MAMI facility is about 1.5 GeV. A high energetic electron beam is used to produce tagged photons. The incident electron beam interacts with a 10 $\mu$m thick Copper radiator and produces Bremsstrahlung photons. The scattered electrons are deflected by a 1.8 T magnetic field towards an array of plastic scintillators to measure the electron energy by means of their position in the focal plane. The difference between incident and outgoing electron energy determines the energy of the Bremsstrahlung photons. A photograph and

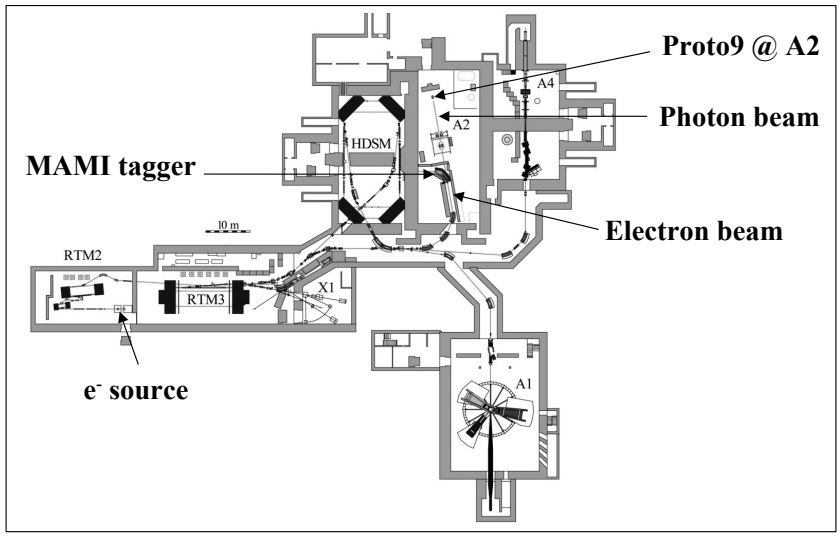


*Figure 6.3: Floor plan of the MAMI accelerator facility at Mainz, Germany, used to produce the tagged photon beam.*

the schematic of the experimental setup are shown in Fig. 6.4. The photograph shows the insulated detector box containing proto9 (kept at $-25°$C) and facing the tagged photon beam, the readout electronics, and the cooling machine. The detector box was mounted on a X-Y positioning table used to calibrate the position of each crystal in the photon beam and to scan the beam across the crystals.

The schematic illustration in the lower panel of Fig. 6.4 shows the tagged-photon spectrometer generating the tagged-photon beam aimed at the proto9 setup. The newly developed prototype readout chain discussed in section 4.3 was used for data acquisition. The readout chain (see Fig. 4.10) consists of a digitizer, a data concentrator, a compute node, and a computer for data storage. The digitizer is equipped with Sampling ADC (SADC) and FPGAs. The SADC was used for the digitization of analog signals produced by proto9. The FPGAs were used for on-line processing (feature-extraction) of the digitized signals. The SADC has sixteen readout channels, fifteen of them were used to sample the detector signals and the remaining channel was dedicated to the tagger signal

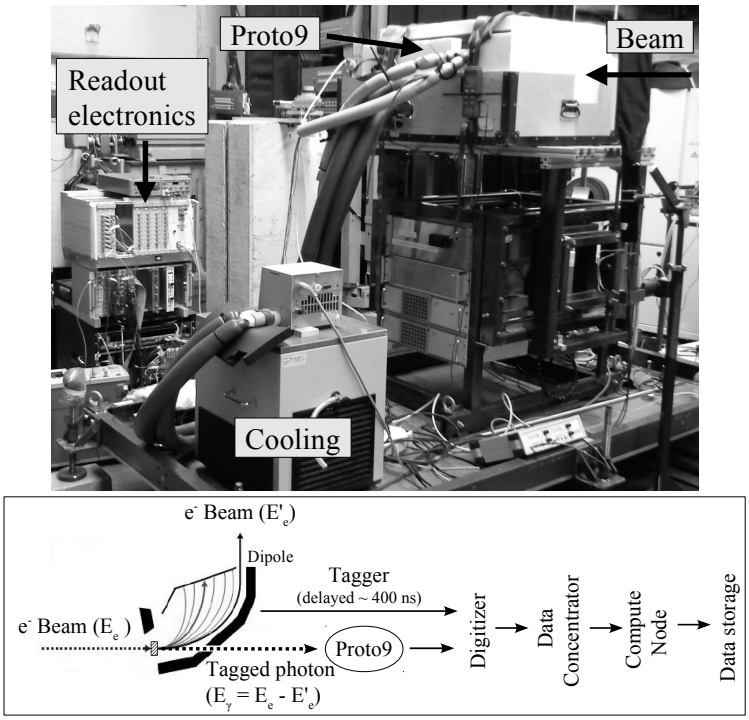


*Figure 6.4: (upper panel) Photograph of the proto9 mounted in the experimental hall (A2) at MAMI; (lower panel) schematic representation of the experimental setup.*

readout. Since the energy of the tagged photons was low in comparison to the full dynamic range of the EMC, only the high-gain outputs of the pre-amplifiers were connected to the digitizer.

In order to make the readout architecture scalable within the available resources, the data acquisition system was designed in such a way that, above a certain energy threshold, data can be stored in three different modes:

- Waveforms only,
- Extracted features of waveforms such as energy and time of valid hits,
- At high hit-rate, overlapping waveforms as well as only features of single waveforms.

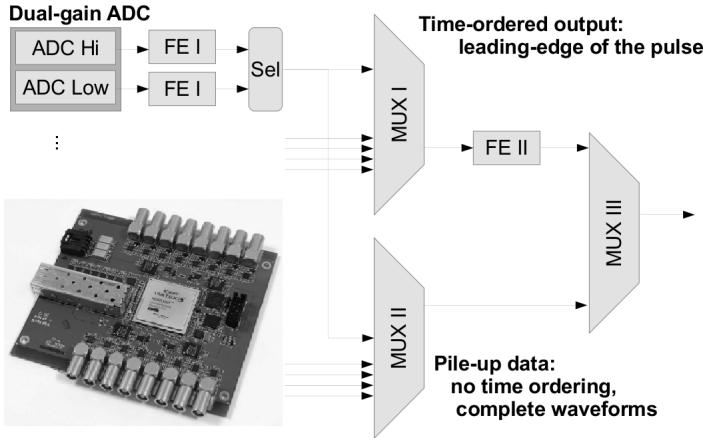


*Figure 6.5: A photograph of the prototype of the PANDA-EMC digitizer using a 16 channel 14 bit 125 MHz SADC and the functional diagram of the implemented feature-extraction firmware.*

The digitizer module together with a functional diagram of the implemented feature extraction (FE) firmware is shown in Fig. 6.5. Each photo sensor is read out by two SADC channels, one for low and the other for high amplification gain. In this way the required dynamic range of 10,000 (see section 4.2) can be achieved. Data from each SADC channel are processed by functional blocks FE I, which include baseline follower and pulse detection. The baseline follower removes a slowly fluctuating offset level from the digitized signal. The pulse is detected in two steps. Once the signal crosses a defined *pulse detection threshold*, the signal samples are written into the memory of the FPGA until the signal level drops below the threshold. Simultaneously, the total sum I of these samples is calculated and the sample with the maximum amplitude A is identified. Finally, based on the values of the ratio I/A and the total length of the pulse, the pulse-detection decision is made. For a well-separated pulse the I/A ratio does not depend on the pulse amplitude and, therefore, is constant. If the measured I/A ratio for a single pulse drops below the constant value, such an event is most probably a noise signal and should be rejected. Larger values of the I/A ratio are caused by the pile-up of several pulses. Therefore, for each waveform the I/A ratio is compared with two discrimination thresholds in order to identify noise, well-separated pulses, and pile-up pulses. A detailed investigation of the pile-up

detection and recovery techniques is reported in the previous chapter. A rough time-stamp is assigned to the detected pulse based on the temporal position of the data sample with the maximum amplitude.

Once the pulse is detected, the FE I block sends the waveform data to the Sel block, where only valid high- or low-gain data are selected. Single and pile-up waveforms are sent to the subsequent time-ordering data-multiplexer MUX I and MUX II, respectively. The data with single waveforms are processed by the FE II block, where the precise time-stamp is determined by the Constant-Fraction timing algorithm and the energy assignment is taking place. These reduced data and the data stream of waveforms from pile-up pulses are combined in the MUX III block and sent to the data concentrator module via an optical fiber.

During the photon-beam experiment, the available highest photon energy was 418 MeV and the beam RMS radius was about 1 cm. The chosen tagger-channel numbers and corresponding photon energies are listed in Table 6.1. The data

| Tagger ch. | 1 | 2 | 3 | 4 | 5 | 6 |
|---|---|---|---|---|---|---|
| Energy | 52 | 80 | 109 | 138 | 195 | 225 |
| | | | | | | |
| Tagger ch. | 7 | 8 | 9 | 10 | 11 | |
| Energy | 278 | 303 | 350 | 390 | 418 | |

*Table 6.1: Selected tagger channels and the corresponding photon energies.*

collection was mainly focused on performance testing of the prototype of the trigger-less readout chain and the pulse pile-up detection algorithm. Therefore, data were collected in two different steps.

First, the photon beam was aimed at the center of one of the crystals at low beam rate (few kHz). This type of data was useful to evaluate the on-line data processing algorithms implemented in the FPGA of the digitizer and to perform the off-line event correlation with the simultaneously recorded signal from the tagging detectors.

After this run, the hit rate was increased to tens of kHz to store overlapping waveforms for the evaluation of the pile-up recovery algorithm. Examples of a single and a pile-up waveform measured at low and high hit-rate are shown in

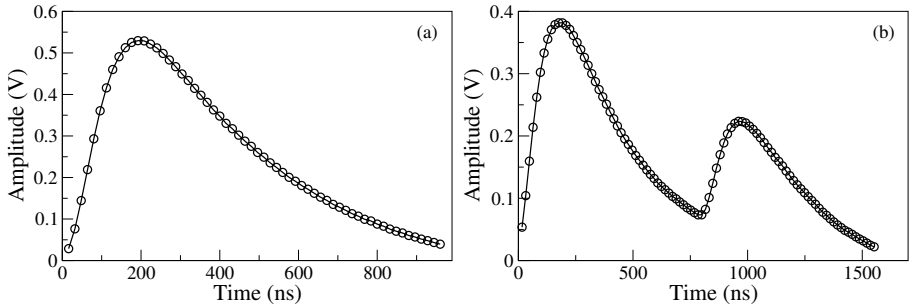


*Figure 6.6: Examples of signal shapes obtained from the detector response to tagged photons: (a) single waveform at low hit rate, (b) pile-up waveform at high hit rate.*

Fig. 6.6 (a) and (b), respectively. The length of the single waveform is about 800 ns and the rise-time is 150 ns. Since the pre-amplifier used in this test is built as an alternative to the ASIC pre-amplifier, the length of the waveform was kept at about 800 ns which is the same as the ASIC waveform length (see section 4.2.3).

Due to inadequate shielding of the pre-amplifiers, the measurements were disturbed by relatively strong pick-up noise and pre-amplifier ringing. Therefore, data were analyzed only for crystals numbered 2 and 3. Due to the high noise level, the single-crystal energy threshold was kept at about 0.014 V (150 SADC channels or ∼22 MeV) for one and at 0.015 V (160 SADC channels or ∼23 MeV) for the other crystal. In the updated version of the pre-amplifier these high noise levels are reduced by almost a factor five [129].

## 6.3 Analysis, results, and discussion

This section contains performance results of the trigger-less readout chain and the pile-up recovery algorithm. In the performance test of the readout chain several topics such as the hit-detection response at low and at high hit rate, and the tagger-correlated event reconstruction using the hit-time information will be covered. In the pile-up recovery, the performance of the energy recovery algorithm is studied using data collected with high detector hit rate.

### 6.3.1 Test of proto9 and the trigger-less readout chain

**Performance at high hit rate**

The expected PANDA EMC hit rate may be as high as 1 MHz and, therefore, it is important to study the performance of the EMC prototype readout chain with high hit rates. To this end, data were collected at various tagger rates and the corresponding hit-rates at the detector were determined. During this measurement only crystals numbered 2 and 3 were used and the photon beam was aimed at crystal 2 for various tagger rates of 7 kHz, 20 kHz, 40 kHz, and 150 kHz, respectively. The hit rates measured at the different SADC channels for a tagger rate of about 40 kHz are plotted in Fig. 6.7. The SADC channel

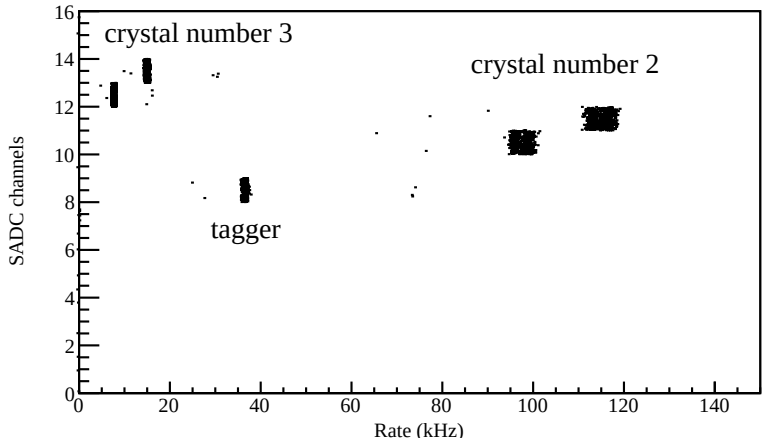


*Figure 6.7: SADC channels versus measured hit rates for a tagger rate of about 40 kHz. The beam was aimed at crystal number 2. Only tagger signals (ch. 8), crystal number 2 (ch. 11-12), and 3 (ch. 13-14) were read out. Two readout channels per each crystal are visible.*

number 8 corresponds to the tagger rate, channels 11 and 12 correspond to the 2 APDs of crystal 2, and channels 13 and 14 to crystal 3. The hit rates plotted on the horizontal axis are estimated by measuring the time required to collect 100,000 hits. Since very few (11) tagger signals were selected out of many ($\approx 400$) channels in the tagger system, the measured tagger rates are lower than the rates measured at the detector (crystal 2). The rate difference seen in the two different

channels of crystal 2 is caused by different settings of the hit-detection threshold and the gain difference of the APDs. The hit rates measured at crystal 3 are small as compared to crystal 2 because the beam was aimed at crystal 2, which caused a small amount of energy deposition in crystal 3 and thus caused a large amount of signals below the applied detection threshold.

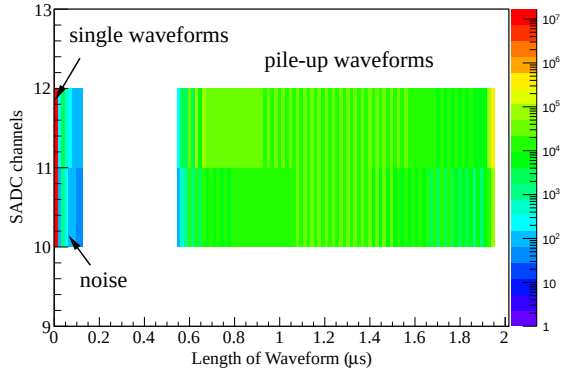


*Figure 6.8: SADC channels versus length of the waveform for almost 110 kHz hit rate at crystal number two. Both the readout channels 11 and 12 are visible.*

It is not possible to calculate pile-up probabilities from the measured data without assumptions. However, it is possible to deduce a suitable ratio $N_p/N_s$ directly from the measured data. Here $N_p$ is the number of the pile-up waveforms and $N_s$ is the number of the single pulses for a given detector hit-rate. This ratio approximates pile-up probabilities only at low pile-up rates ($N_p << N_s$). An estimate of the ratio ($N_p/N_s$) for various hit rates at the detector is carried out by plotting SADC channels versus the length of the waveform as shown in Fig. 6.8. During this measurement, the pile-up identification method was used to discriminate the single waveforms from the pile-up waveforms caused by high hit rates at the detector. The waveforms above a certain identification threshold were stored as pile-up waveforms and the waveforms below the threshold were classified as single pulses, and only features of such pulses were stored. Fig. 6.8 shows three regions: The first (red colored) is the single-pulse region where only the features (hit-energy and hit-time) of the single pulses were stored and the length of such waveforms was set to zero $\mu$s as a tag to identify FE events after feature

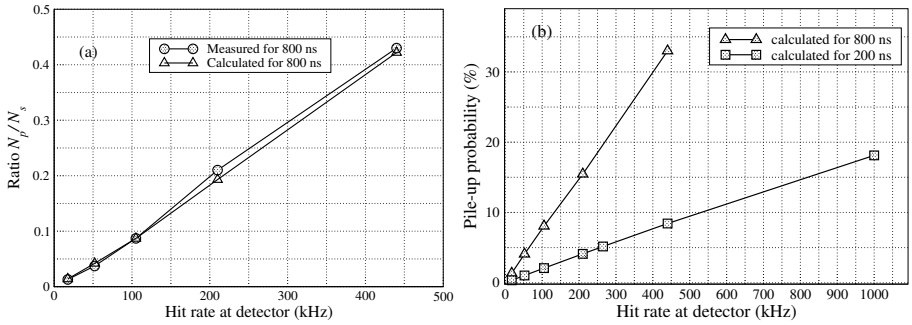


*Figure 6.9: (a) Comparison of measured and calculated ratios of the number of pile-up waveforms ($N_p$) over the number of single pulses ($N_s$) as a function of the hit rate at the detector, (b) Comparison of pile-up probability for different pulse lengths as a function of the hit rate at the detector.*

extraction. The second region contains noise (fraction of $\mu$s). The third region is the pile-up pulse region where complete waveforms of the pile-up structures were stored. The ratio ($N_p/N_s$) is estimated by taking the number of counts measured in the pile-up waveform region ($N_p$) and in the single-waveform region ($N_s$). In this way, the ratio ($N_p/N_s$) is measured for different hit rates. The calculated ratio is obtained using a Poisson time distribution (see equation 5.5). Both the measured and the calculated ratios ($N_p/N_s$) are plotted as a function of the hit rates measured at the detector in Fig. 6.9 (a). A waveform length of 800 ns (see section 6.2) was used to estimate the rate parameter of the Poisson distribution. The measured and calculated ratios are almost equal up to 440 kHz detector hit-rate. Therefore, the readout chain performed smoothly up to detector hit rates of 440 kHz.

Since PANDA is a fixed-target experiment, the forward endcap EMC will be exposed to high hit-rates of up to 1 MHz and the barrel EMC up to 100 kHz. Hence, the present test reveals that the readout chain can be used for the barrel EMC. However, for the forward endcap EMC, due to the high hit rate, the pulse length of 200 ns [12] will be used to reduce the pile-up probability. During the test experiment, the first version of the pre-amplifier with 800 ns pulse length was used. Currently, in the updated version, the pulse length is reduced to 200 ns by using various pulse-shaping stages, keeping the low noise level [129]. The

pulse length of 200 ns is chosen because it is longer than the decay time of the scintillation process, in order to collect the complete signal, and short enough to reduce the pulse pile-up. Therefore, using the pulse length of 200 ns, the performance of the readout chain can be easily increased at high hit rates. In this case the maximum pile-up structure would have a length of 400 ns. According to Fig. 6.9 (b), for a pulse length of 200 ns at a hit rate of 1 MHz the pile-up probability is about 18%. However, for a pulse length of 800 ns the measured pile-up probability of 18% corresponds to the detector hit rate of 200 kHz. Therefore, we conclude that the prototype EMC readout chain will perform well without any limitation for the incoming hit rate of up to 1 MHz for a pulse length of 200 ns for the forward endcap EMC.

### Hit correlation with tagger

In the present experiment all data were collected without hardware trigger as it is planned for the PANDA experiment. In such a trigger-less readout system the detector waveforms above a certain energy threshold were processed on-line in FPGAs and their features such as energy and time were stored.

In order to evaluate the correct data correlation, a tagged-photon beam of low rate (a few kHz) was aimed at a single crystal and only features of the detector- as well as tagger-waveforms were stored. The correlation of the detector hits with the tagger is based on the time-stamp information. Since the tagger signals were delayed in time (see Fig. 6.4), the time difference between tagger time and hit time was used to correlate detector hits with the tagger. The time difference distributions for the highest and the lowest tagger energy are shown in Fig. 6.10 (a) and (b), respectively. The time difference window marked by arrows was used to obtain detector hits correlated with the tagger. Figure 6.11 compares the distributions of energy deposition measured in a single crystal for all hits and for the hits which are correlated with the tagger. A clear hit-correlation with the tagger is obtained based on the time stamp only, showing almost background-free energy selections.

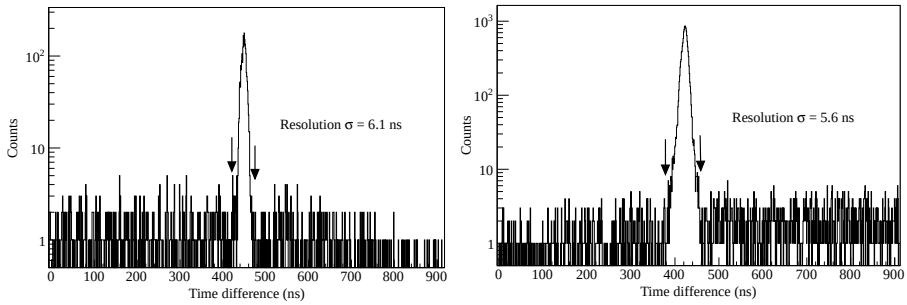


*Figure 6.10: Time difference between the tagger time and the hit time. Left panel for the highest (418 MeV) and right panel for the lowest (50 MeV) tagger energy at 20 kHz and 5 kHz detector hit-rate, respectively. The time difference window marked by arrows was used to obtain detector hits correlated with the tagger.*

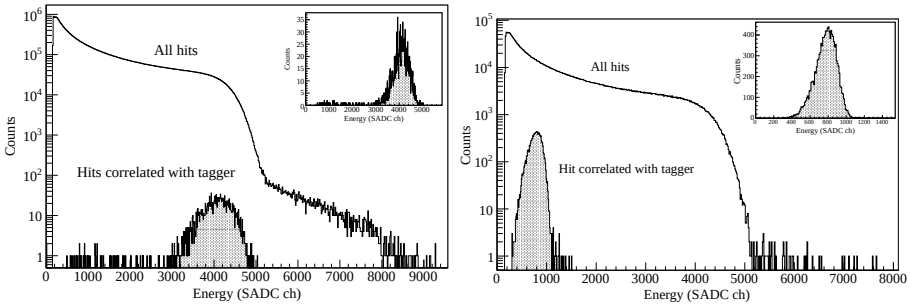


*Figure 6.11: Distributions of the energy deposition measured in a single crystal: comparison of all hits and hits correlated with the tagger (shaded area). Spectra in the left and right panels show the hit correlation for the highest (418 MeV) and the lowest (50 MeV) energy photons at 20 kHz and 5 kHz detector hit rate, respectively. The inset panels show the vertical axis of the shaded spectra on linear scale.*

### Detection-system response

In order to check the consistency of the obtained tagger-coincidence spectra, the measured energy distributions were fitted with an asymmetric Gaussian function [64] and the extracted mean values were compared with the photon energies as given by the tagging detectors. The comparison is shown in Fig. 6.12. The measured mean-amplitude values are proportional to the true photon energies. This

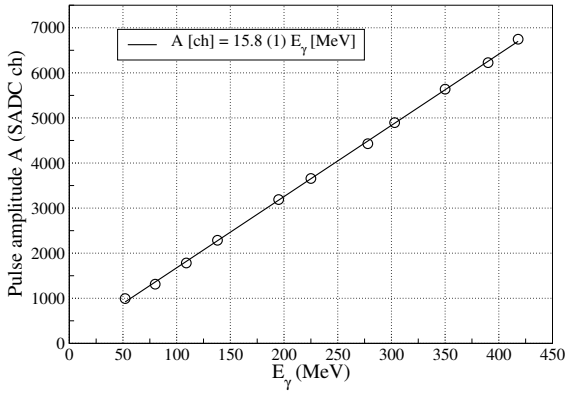


*Figure 6.12: The measured mean amplitude of hits correlated with tagging detectors, plotted as a function of the true photon energy.*

observation demonstrates that the event-identification procedure works properly and the response of the detection system is linear.

### 6.3.2 Verification of the pile-up recovery algorithm

In this section we study the performance of the pile-up identification and recovery algorithm. The tagged photon beam at a high hit rate was aimed at the center of a single crystal and only pile-up waveforms were stored. All tagger channels were read out for the pile-up identification test and only one tagger channel was selected for the pile-up recovery test.

#### Pile-up identification

The algorithm developed for the identification of pile-up waveforms was discussed in section 5.3.2 and was previously tested with simulated waveforms. In order to test the implementation of the algorithm, described in section 6.2, one of the measurements was performed with both I/A discrimination thresholds set to zero. In this mode, all detected waveforms are marked as a *pile-up structure* and thus are stored as complete waveforms for further off-line analysis. The I/A ratio was calculated off-line for each waveform. The distribution of the I/A ratio as a

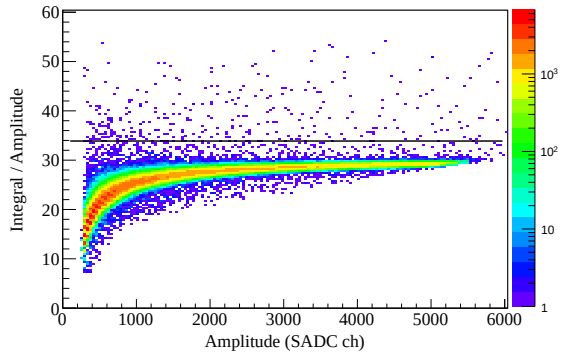


*Figure 6.13: The off-line calculated I/A ratio as a function of the maximum sample value A detected in the waveform. The black horizontal line indicates the pile-up discrimination threshold used in the further measurements.*

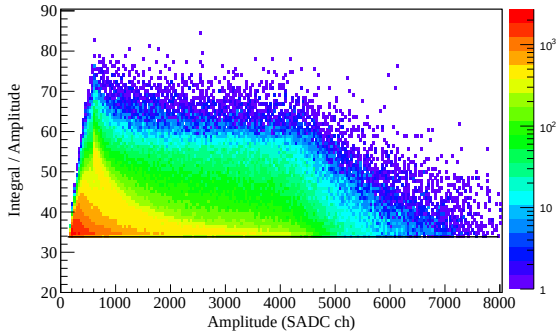


*Figure 6.14: The I/A ratio plotted as a function of the maximum sample value A, calculated off-line for waveforms identified as pile-up events. The black horizontal line indicates the pile-up discrimination threshold.*

function of the maximum sample value A, stored in the waveform, is shown in Fig. 6.13. The observed I/A ratio is constant for large values of A. At lower amplitudes the I/A becomes smaller since the sum of samples above the pulse-detection threshold is not any more a good approximation of the pulse integral. During the test experiment, the threshold on the I/A ratio was set to a value of 34. All detected waveforms with an I/A ratio below 34 were processed on-line in the digitizer. Waveforms with a larger I/A value were identified as pile-up events

and were stored on disk as complete waveforms. For waveforms identified on-line as pile-up events, the I/A ratio is plotted as a function of the maximum sample value A in Fig. 6.14. All values are indeed found above the pile-up discrimination threshold as they should. Figure 6.6 presents a typical waveform from this data sample with a large I/A ratio, where two pulses merged into a single structure recognized as pile-up signal. The off-line analysis of stored waveforms confirmed that all these events had indeed a distorted pulse shape due to pile-up.

### Energy recovery studies

In order to study the performance of the energy recovery algorithm, only pile-up waveforms and the hit-energy and hit-time of the single waveforms were stored. The hit-energy of single waveforms is useful as a reference for comparison with the recovered energy of pile-up signals. The photon beam was aimed at the center of a single crystal and only one tagger channel was selected. The stability of the signal shape is crucial (see chapter 5) and was tested by plotting the waveform integral as a function of the waveform amplitude shown in Fig. 6.15. The rather precise linear relation confirms that the stored waveform shapes are stable over the dynamic energy range of 35. This energy range is limited here by the maximum available photon beam energy.

The same procedure as discussed in chapter 5 is used to obtain the energy

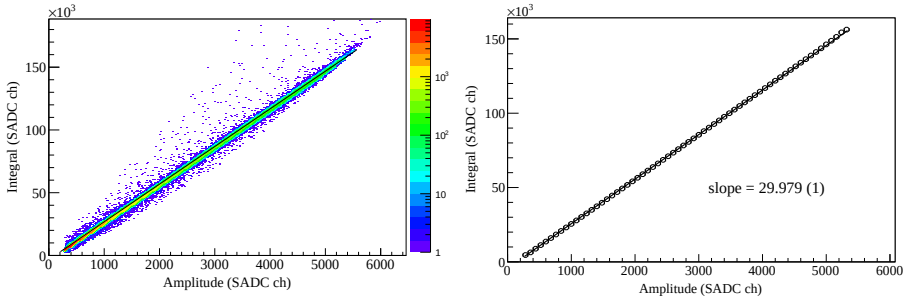


*Figure 6.15: Left panel: The waveform integral as a function of the waveform amplitude for single waveforms; right panel: horizontal axis profile of the figure in the left panel.*

of the pile-up pulses. Since the data were collected without hardware trigger, the hit-time information was used to correlate the reconstructed photon energy with the tagger. The hit-times of the first pulse and the second pulse in the two components of the pile-up waveform structure were obtained by using the time reconstruction algorithm reported in section 5.3.5. The distributions of the time difference between the tagger time and the hit time for pile-up pulses are shown in Fig. 6.16. The random hits are caused by the high hit rates. In the tagger spectrometer, at high rates several electrons may simultaneously create Bremsstrahlung photons. If the tagger-correlated photon gets lost in the collimator, we measure a random photon hitting the detector causing a random hit. These random hits are not observed at low tagger rate (see Fig. 6.10). The time-difference window marked by arrows was used to obtain detector hits correlated with the tagger. Such correlated photon-energy distributions for a single tagger

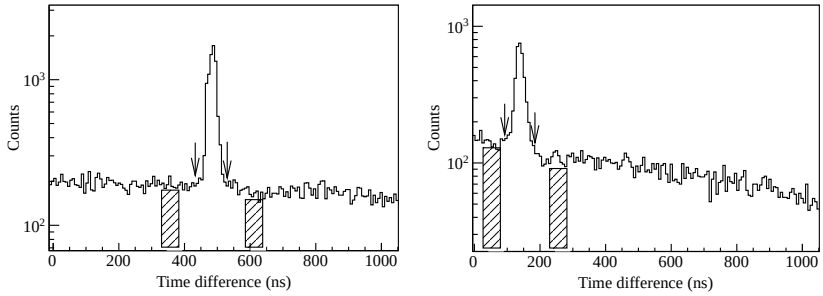


*Figure 6.16: Time difference between the tagger time and the hit time: for the first pulse (left panel) and the second pulse (right panel) in the two components of the pile-up waveform structure, respectively. The time windows denoted by the shaded regions (side windows) were used for the background subtraction.*

are shown in Fig. 6.17. The background caused by random hits is subtracted from the shown distributions. The background is obtained by measuring the energy distributions in the corresponding side windows of the time distributions (shaded regions in Fig. 6.16), exactly of the same size as used for the event-selection in the signal region and the events within this time interval (divided by 2) were used for the background subtraction. The energy distributions shown in the left and right panel of Fig. 6.17 correspond to the first and second pulses, respectively, in the two components of the pile-up waveform structure. The energy distribu-

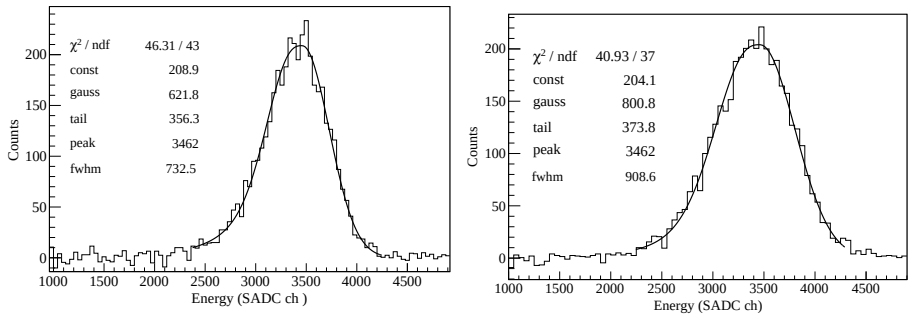


*Figure 6.17: Reconstructed and tagger-correlated photon energy distributions: for the first pulses (left panel) and the second pulses (right panel) in the two components of the pile-up waveform structure, respectively. The photon energy distributions are fitted using an asymmetric Gaussian function.*

tion for the first pulse is used as reference to judge the energy recovery of the second pile-up pulses. The measured distributions were fitted with an asymmetric Gaussian function [64]. The extracted peak values of both the distributions demonstrate a complete energy recovery of the second pile-up pulses in the two components of the pile-up waveform structure. The fit parameter fwhm gives the full width at half maximum of the distribution. The fwhm of the pile-up reconstructed distribution (right panel) is 24% higher as compared to the reference energy distribution (left panel). The difference in fwhm is caused by the propagation of fluctuations in the estimation of the first-pulse amplitude ($A_1$) into the determination of the second-pulse amplitude ($A_2 = (I_{tot}/k) - A_1$). Here $I_{tot}$ is the integral of the pile-up waveform structure and $k$ is the slope shown in Fig. 6.15.

## 6.4 Summary and conclusion

A prototype of nine PWO-II crystals (proto9) was developed to study the performance of the PANDA EMC readout chain and the pile-up identification and recovery algorithm in a tagged-photon beam. Using only the time-stamp information, the correlation of detector hits with the tagger information was achieved. The measured mean amplitude values are proportional to the true photon ener-

gies. This observation demonstrates that the event-identification procedure works properly and the response of the detection system is linear.

The performance of the prototype readout chain was tested for different detector hit-rates from a few kHz up to 440 kHz. The readout chain worked reliably for hit rates of up to 440 kHz for a waveform length of 800 ns. Since PANDA is a fixed-target experiment, the forward endcap and barrel EMC will be exposed to high hit rates of up to 1 MHz and 100 kHz, respectively. Hence, the present test reveals that the readout chain can be used for the barrel EMC. The pile-up probability obtained using a Poisson time distribution for a pulse length of 200 ns is about 18% at a hit rate of 1 MHz. However, for a pulse length of 800 ns the measured pile-up probability of 18% corresponds to the detector hit-rate of 200 kHz (see Fig. 6.9). Therefore, we conclude that the prototype EMC readout chain will perform normally at an EMC hit-rate of 1 MHz for a pulse length of 200 ns for the forward endcap EMC. The pulse length of 200 ns is chosen because it is longer than the decay time of the scintillation process, in order to collect the complete signal, and short enough to reduce the pulse pile-up.

The linear relation between the measured waveform integral and the waveform amplitude confirms that the waveform shape was stable during the measurement. The pile-up identification algorithm implemented in the digitizer FPGAs works properly. The performance of the pile-up recovery algorithm is successfully tested for the pile-up waveforms. These waveforms were collected using the detector response for the high-rate tagged photon beam. The test of the pile-up recovery algorithm results in complete energy recovery of the second pulses in the two components of the pile-up waveform structure.

# Chapter 7

# Clustering and Simple Event Selection

This chapter is dedicated to studies of two important issues related to the on-line data-processing of the PANDA EMC. The first issue is the clustering-method to achieve the best possible shower-energy reconstruction and hence energy resolution. The second issue is the demonstration of simple but effective on-line event-selection criteria which will use as little FPGA resources as possible. These two challenges will play a crucial role in the on-line and trigger-less data processing of the PANDA experiment. The clustering and the event selection will be performed in the compute-node stage of the PANDA EMC readout chain (see chapter 6). These two issues are studied using the BESIII off-line software BOSS (see chapter 3) and the BESIII experimental data collected by performing $e^+e^-$ annihilations in the charmonium mass region.

Section 7.1 contains an introduction to the BESIII EMC and its data-flow structure. In section 7.2 the EMC clustering and shower-energy reconstruction methods such as e$3\times3$, e$5\times5$, and Dynamic Sum are described. Section 7.3 contains simulations performed to validate the shower-energy reconstruction methods for single photons over the energy range from 20 MeV to 1 GeV. In section 7.4 on-line event-selection criteria are discussed for charmonium radiative

transitions $\psi' \rightarrow \gamma\chi_{cJ}$ $(J = 0, 1, 2)$. The summary and outlook is presented in section 7.5.

## 7.1 Introduction

The BESIII detector (see section 3.3.2) consists of four sub-systems: Drift chamber, Time-of-flight, EMC, and Muon counter. The EMC is designed to measure electron and photon energies and to provide hardware trigger signals to the data acquisition system. An overview of the BESIII EMC is shown in Fig. 7.1. The EMC is made of 6240 CsI (Tl) scintillating crystals, arranged in barrel and endcap shapes. This type of arrangement is made to achieve a polar angle coverage of $21.3° - 158.7°$ [80].

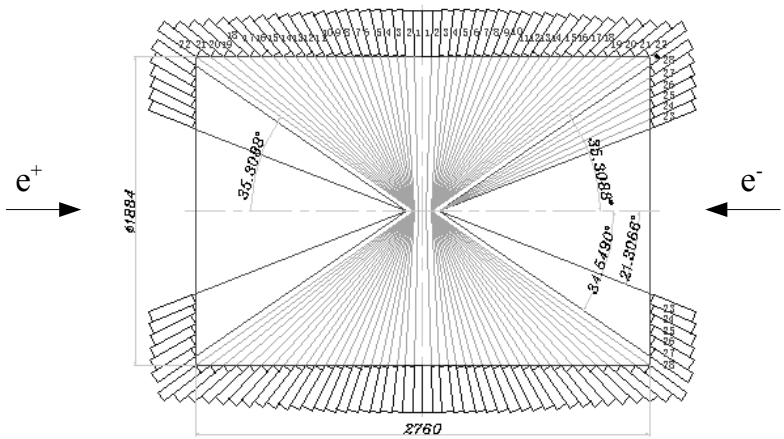


*Figure 7.1: Overview of the BESIII EMC [130].*

The BESIII collaboration has developed a dedicated off-line software BOSS (BESIII Offline Software System) for the data analysis. Before discussing the software, it is important to introduce an input to the analysis software. When electrons or photons hit the EMC crystals, they lose their energy via excitation and ionization of an atom and Bremsstrahlung, creating an electromagnetic shower (see section 4.1). The shower energy is collected by means of scintillation light using photosensors, whose signals are amplified and shaped by pre-amplifiers.

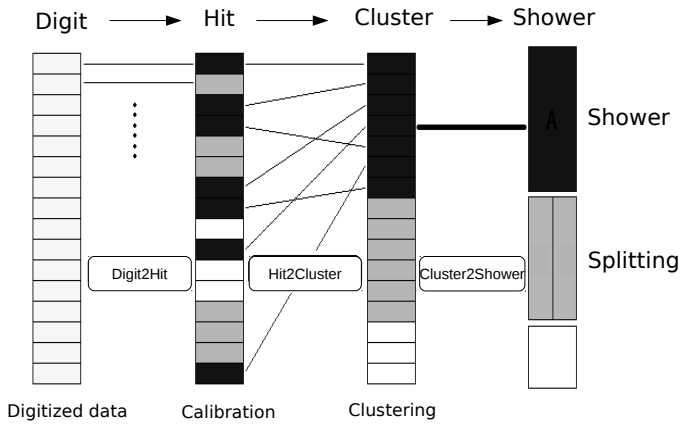


*Figure 7.2: Schematic of the BESIII EMC data flow [131].*

The analog signals coming out of the pre-amplifiers are digitized using digitizer modules. This complete scheme of front-end electronics provides the experimental input to the EMC data flow shown in Fig. 7.2. Similarly, to provide the simulation input to the EMC data-flow, the simulation part of BOSS loads the geometry of the BESIII EMC and simulates the EMC response to single photons as well as to photons and electrons from the charmonium decay channels modeled using event generators [132].

Fig. 7.2 indicates the flow of the data from left to right (Digit to Shower) in four stages. The digitized signals produced by the digitizer are shown at the left column named *Digit*. These digits, or off-line raw data, are calibrated in the second stage, named $Hit$, and this process is called $Digit2Hit$. In this process the ADC values are replaced by energy information for each crystal. In the third stage the clustering is performed where a series of connected crystals with energy deposition above a certain threshold is considered. Neighbor information from hits in the same region is collected to form a cluster. As an example the third column from the left (Cluster) shows three clusters in black, gray and white colors. This process is called $Hit2Cluster$. Each cluster formed in this stage is used as input for the forth and last stage called $Cluster2Shower$. In this process, the maximum energy deposition (seed) in the formed cluster is used to define the possible shower. The shower energy is obtained by summing the energy

deposition of each crystal contributing to the cluster. If the cluster has more than one seed, the cluster-splitting algorithm is used to split the cluster into different showers. The column at the right (Shower) shows examples of single showers by the white and black boxes and shower splitting by the two gray boxes.

## 7.2 Shower energy reconstruction method

The shower reconstruction methods are developed to measure the energy deposition of an incident particle in the EMC. To define the shower energy, commonly used methods are e3 $\times$ 3 and/or e5 $\times$ 5. Currently in the BESIII off-line software BOSS, e5 $\times$ 5 is employed to define the shower energy for the BESIII EMC [133]. An illustration of these methods is shown in Fig. 7.3. The e3 $\times$ 3 and e5 $\times$ 5

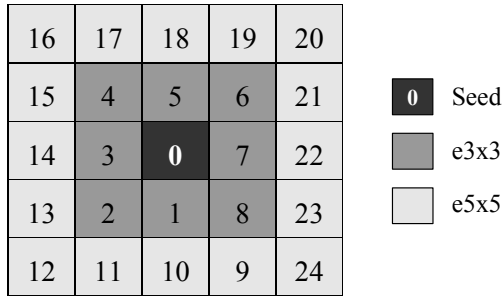


*Figure 7.3: Illustration of shower energy reconstruction methods.*

methods use the energy sum of 9 and 25 crystals, respectively, around and including the seed. In general, for high-energy incident particles the shower can spread over more than nine crystals. Therefore, the e3 $\times$ 3 method may miss important information. Conversely, at low energies the shower develops over a bunch of nine or even fewer crystals. In this case, the use of the e5 $\times$ 5 method may include crystals with low signal-to-noise (SNR) ratio and will add noise to the shower energy and affect the energy resolution. In case of the BESIII EMC, the electronic noise is about 200 to 300 keV per readout channel. Thus, a 0.5 MeV energy threshold is good enough to remove almost all false triggering of the crystal-readout. However, the electronic noise is usually mixed with real signals in the same crystal. For example, if a 2 MeV gamma hits a crystal, with

a signal fluctuation of 0.3 MeV equivalent energy from electronic noise, then the measured energy is 2.3 MeV (ideally). This means that the noise can not be removed completely from the cluster sum by any threshold. Moreover, the signals which are very close to the threshold, whose SNR is considerably lower, will also affect the energy resolution. Hence, the impact of the noise will be larger in case of very low-energy gammas.

Therefore, in the reported studies a new method called Dynamic Sum, currently used in the CMS Experiment [134] for electromagnetic showers, is considered. To achieve the best possible shower-energy reconstruction, the possible improvements in the present Dynamic Sum method are also studied. In the currently reported method, first the sum of the energy deposition in each crystal contributing to the shower is performed to obtain the energy scale of the shower. Subsequently, the crystals contained in a shower are sorted by their energies in descending order. After the crystal sorting, the energy of the first (i.e. highest energy) $N$ crystals is summed to calculate the shower energy. At this stage we reject any crystal whose energy is less than an optimized *dynamic* threshold, namely crystals with low SNR. In this way, by setting different optimized dynamic energy thresholds for each energy scale, the impact of the noise can be reduced. The performance studies of the above mentioned methods are reported in the following section.

## 7.3 Simulations using single photons

To study the performance of shower-energy reconstruction methods and to optimize the threshold for the Dynamic Sum method, simulations were carried out using single photons. They were produced by an event generator over the energy range of 20 MeV to 1 GeV. Basic tests were performed to study the response of the BESIII EMC using 10,000 single photons. Figure 7.4 (a-c) shows a few parameters such as shower energy (e5 $\times$ 5), polar angle $\theta$, and azimuthal angle $\phi$ reconstructed from the EMC response, and their comparison with the true Monte Carlo (MC) information. The reconstructed parameters are in good agreement with the true MC information. In Fig. 7.4 (b), the $\theta$ reconstruction is not seen from 0° to 20° and 160° to 180° because in this region there is no EMC cover-

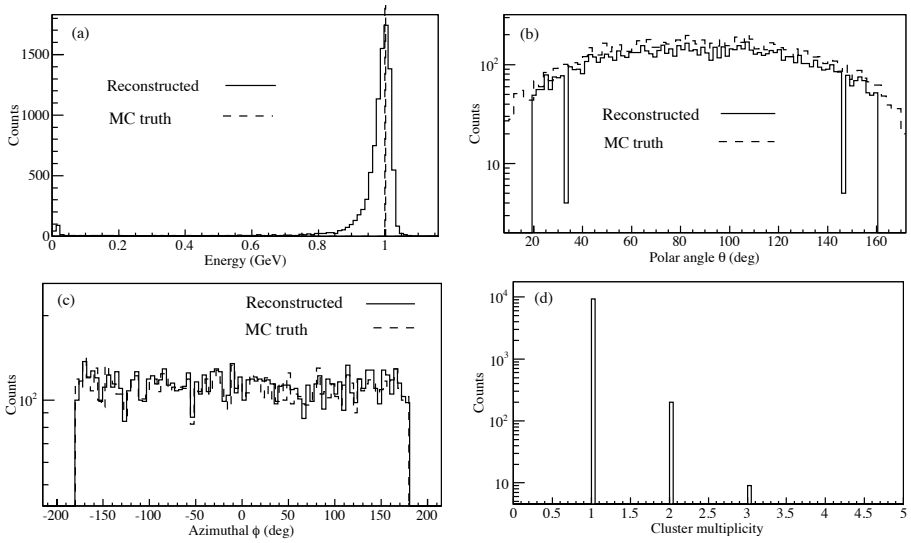


*Figure 7.4: Various parameters, reconstructed for the BESIII EMC, in comparison with the Monte Carlo (MC) truth information simulated for single photons at 1 GeV: (a) photon energy distribution, (b) polar angle distribution, and (c) azimuthal angle distribution. The histogram in panel (d) shows cluster multiplicity.*

age, since the region is occupied by the Multilayer Drift Chamber (MDC). The cluster-multiplicity distribution for single photons, shown in Fig. 7.4 (d), confirms that the cluster finding works properly and is more than 99% efficient. To simulate the realistic situation, beam-related background events are mixed into the simulation. These events consist of real gammas, electrons, and positrons from beam-gas reactions, and their energy could be a few MeV.

Using the above mentioned procedure, simulations were carried out for single photons over the energy range from 20 MeV to 1 GeV at an energy threshold of 0.5 MeV for 10,000 events. All the three methods e3 $\times$ 3, e5 $\times$ 5, and Dynamic Sum were used to reconstruct the shower energy of single photons for different energies. As an example the shower-energy distribution obtained using the Dynamic Sum method at 1 GeV single photons is shown in Fig. 7.5. An asymmetric Gaussian function [135] was used to fit the distributions and to obtain the energy resolutions. In this way the energy resolutions were obtained at various energies

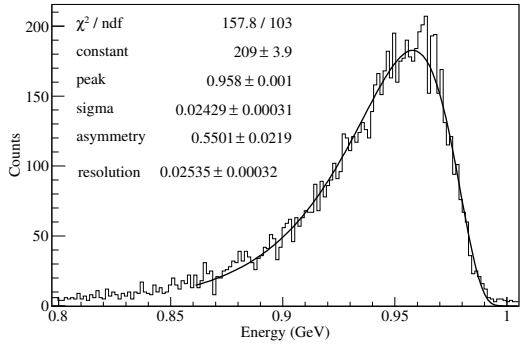


*Figure 7.5: Simulated shower-energy distribution at 1 GeV photon energy for the Dynamic Sum method. The distribution is fitted by an asymmetric Gaussian function [135].*

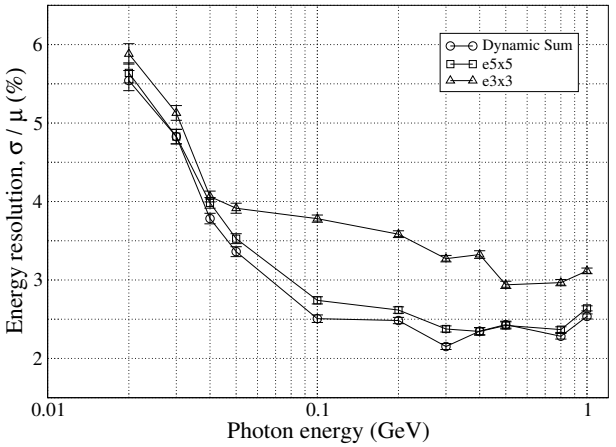


*Figure 7.6: Energy resolution as a function of the photon energy simulated for single-photon energies ranging from 20 MeV to 1 GeV. The circles, squares, and triangles indicate the Dynamics Sum,* e5 × 5*, and* e3 × 3 *method, respectively. The error bars indicate the statistical uncertainty.*

and are plotted as a function of the photon energy in Fig. 7.6. The energy resolutions obtained using the Dynamic Sum and the e5×5 methods do not differ much. However, the Dynamic Sum method provides a slightly better energy resolution than the e5×5 method. The energy resolution saturates above 300 MeV because of the material in front of the EMC. It includes the beam pipe, drift chamber

and the TOF detector with two layers of scintillator, which absorb a part of the energy with large fluctuations. This effect causes a low-energy tail for low-energy photons and enlarges the width of the energy spectrum for high-energy photons.

The energy resolution in the high-energy region (see Fig. 7.6) can be improved by correcting for the material effects [135]. In addition, to improve the performance of the Dynamic Sum method in the low-energy region, a cutoff energy threshold is applied while summing the sorted crystals for each energy scale. A crystal whose energy is less than the optimized cutoff threshold of the current sum is rejected. To obtain the optimized threshold values, a few energy scales were considered in the simulations. Figure 7.7 shows the energy resolutions as a function of the cutoff threshold obtained by simulating the EMC response to single photons of energy 128 MeV, 171 MeV, and 261 MeV. These energy scales are used because they correspond to the photon energies in the charmonium E1 transition $\psi^{'} \rightarrow \gamma\chi_{cJ}$ $(J = 0, 1, 2)$. The plots in Fig. 7.7 confirm that, in the low-energy region, the energy resolution for the Dynamic Sum method is superior to the e5 $\times$ 5 method. The optimized cutoff threshold values obtained from Fig. 7.7 are plotted as a function of the peak values of the shower-energy distribution obtained using the e5 $\times$ 5 method. The data points (circles) were fitted using a linear function and this response was used to extrapolate the cutoff energy threshold over the BESIII EMC energy range from 20 MeV to 380 MeV. At 380 MeV the extrapolated value of the threshold becomes zero. Therefore, above 380 MeV the Dynamic Sum methods with and without cutoff threshold become identical.

Using the optimized cutoff threshold, the energy resolution obtained by simulating the EMC response for single photons is plotted as a function of the photon energy in Fig. 7.9. The energy resolution obtained using the e5 $\times$ 5 method is used for a comparison with the Dynamic Sum. In the high-energy region the energy resolution is improved due to the material-effect correction as compared to the energy resolution shown in Fig. 7.6. The Dynamic Sum with cutoff threshold shows a slight improvement as compared to the earlier Dynamic Sum method. The energy resolution obtained using the Dynamic Sum with threshold is on average better by 4.8% than the e5 $\times$ 5 method. The relative shift in the peak position of the photon energy due to the application of the Dynamic Sum ($\mathrm{Peak_{E_d}}$) with threshold with respect to the e5 $\times$ 5 method ($\mathrm{Peak_{E_{25}}}$) is studied

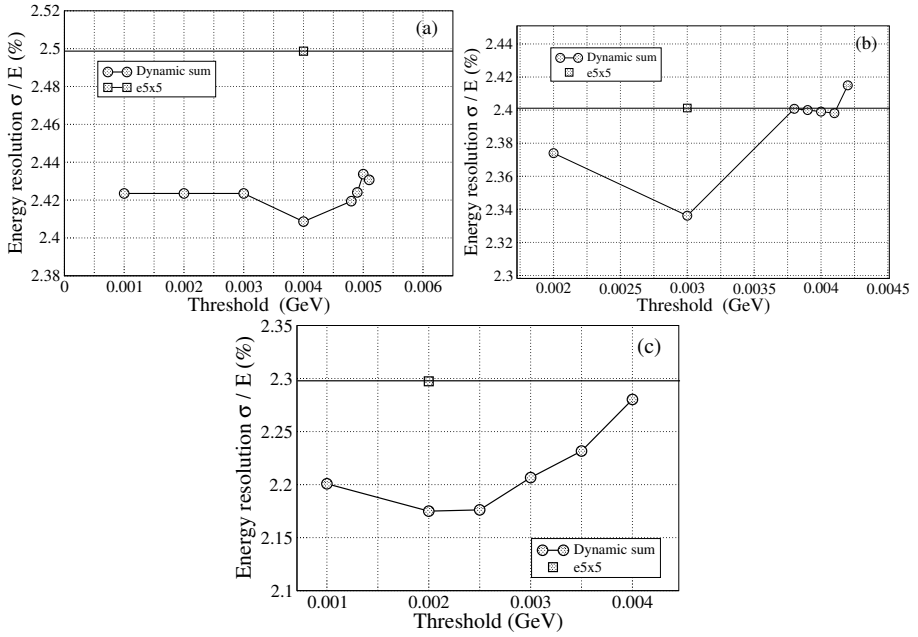


*Figure 7.7: Energy resolution as a function of the cutoff threshold for photon energy of 128 MeV (a), 171 MeV (b), and 261 MeV (c). The circles and square indicate the energy resolution obtained using the Dynamic Sum and e5×5 method, respectively.*

by plotting the relative shift (Relative shift = $(\mathrm{Peak_{E_d}} - \mathrm{Peak_{E_{25}}})/\mathrm{Peak_{E_{25}}}$) as a function of the peak position for the e5 × 5 method in Fig. 7.10 (a). It is clearly seen that the relative shift is smaller than 0.65% which is in the range of the error of the absolute energy calibration [135]. Moreover, the relative difference (Relative diff. = $(\mathrm{Peak_{E_d}} - \mathrm{E_i})/\mathrm{E_i}$) in the input energy ($E_i$) of the photon in the simulation and the reconstructed photon energy using both methods is plotted in Fig. 7.10 (b). The difference in the low-energy region is smaller. However, in the high-energy region the Dynamic Sum with threshold is superior to the e5 × 5 method because of the shower leakage in the latter. Therefore, the above reported studies show that the method of the Dynamic Sum with threshold performs slightly better compared to the e5 × 5 method and the Dynamic Sum method without threshold. Since the improvement is only marginal, the Dynamic

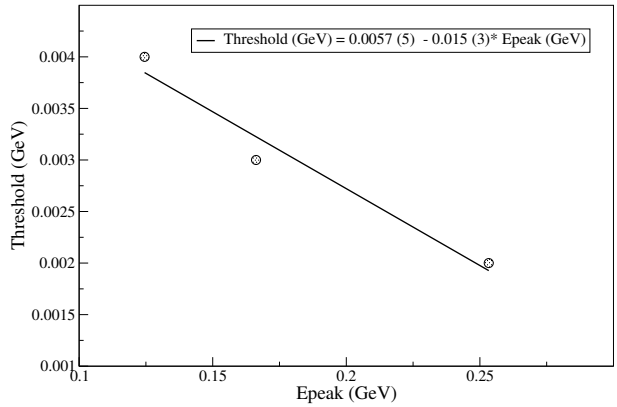


*Figure 7.8: Optimized threshold values for the Dynamic Sum method as a function of peak values of the photon energy distribution obtained using the e5 × 5 method.*

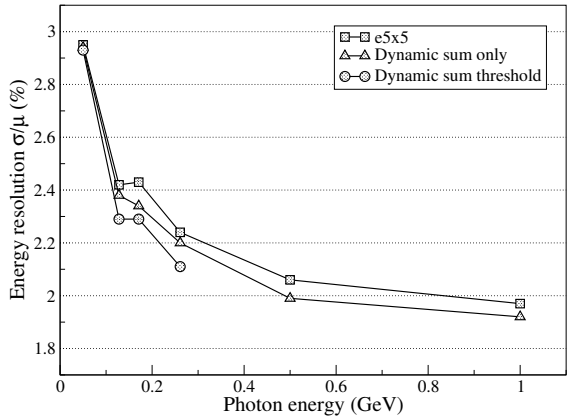


*Figure 7.9: Energy resolution as a function of the photon energy. The energy loss in the time-of-flight detector is corrected.*

Sum can safely be used for the on-line clustering and shower-energy reconstruction in the compute-node stage of the PANDA EMC readout chain. The methods e5 × 5 and Dynamic Sum with threshold require more computational steps (see section 7.2) as compared to the plain Dynamic Sum. Hence, the on-line usage of the latter method will require less FPGA resources, resulting in less power consumption, and is the preferred one.

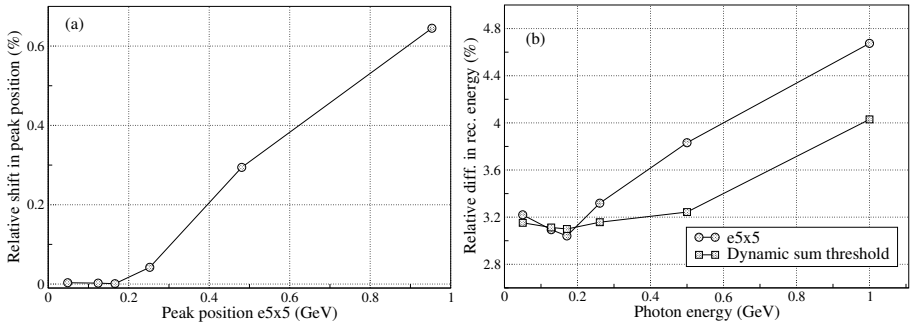


*Figure 7.10: (a) Relative shift in the peak position of the photon-energy distribution obtained using the Dynamic Sum method as a function of the peak values of the photon energy distribution obtained using the e5 × 5 method; (b) Comparison of relative differences in the recovered photon energy as a function of input photon energy used in the simulations.*

## 7.4 Charmonium radiative transition

The electric dipole (E1) transition $\psi^{'} \rightarrow \gamma\chi_{cJ}$ $(J = 0, 1, 2)$ (see Fig. 3.3) is studied to demonstrate the performance of simple event-selection criteria for the usage in on-line event-selection studies for the PANDA experiment. Since the existing BESIII experimental data-set does not contain single-crystal information, the method of Dynamic Sum can not be used for an extended physics analysis. However, since the performance of the e5 × 5 method does not differ considerably from the Dynamic Sum, the electric dipole (E1) transition has been studied using the e5 × 5 method. Moreover, the e5 × 5 method is commonly used in the BESIII collaboration for the physics analysis.

### Simple event selection

A data sample of about 106 million $\psi^{'}$ decays recorded using the BESIII detector (see section 3.3.2) was used to study the event-selection criteria and to estimate the product of branching fractions of two subsequent radiative transitions (product branching fraction) $\psi^{'} \rightarrow \gamma(\gamma J/\psi)_{\chi_{cJ}}$ $(J = 0, 1, 2)$. Here $J/\psi$ decays to a lepton pair $(l^{+}l^{-})$, where $l$ denotes $e$ or $\mu$. The photons radiating from $\psi^{'} \rightarrow \gamma_{sm}\chi_{cJ}$ and $\chi_{cJ} \rightarrow \gamma_{lg}J/\psi$ are named smaller $(\gamma_{sm})$ and larger $(\gamma_{lg})$ energy

photon, respectively. For the selected radiative E1 transition the basic selection criteria are to have only two photons and two charged particles. The charged tracks are reconstructed from hits in the Multilayer Drift Chamber (MDC). The photon candidates are reconstructed from a shower energy measured in the EMC.

At first, in the event selection only EMC information is used to demonstrate the effect of on-line event selection on the background suppression. The charged track information from the MDC is used at the end of the chain of selection criteria, since precise tracking requires a lot of on-line computation and, therefore, should be done only for a limited number of events. The shower-energy spectrum measured using the EMC without any selection is shown in Fig. 7.11 (a). The energy spectrum contains the shower energy of photons as well as charged particles. The peak around 1.8 GeV is caused by the primary electron and positron beam energy deposition in the EMC after Bhabha scattering. The energy deposition observed at very high energies is caused by the nuclear counter effect [136, 137] in the PIN diodes of the BESIII EMC. The nuclear counter effect occurs when some of the electrons and photons in an electromagnetic shower leak out from the rear end of the calorimeter and hit the PIN diode directly, thereby depositing a significant amount of energy in the PIN diode.

The very effective event-selection steps used for obtaining background suppression and almost clean signals are:

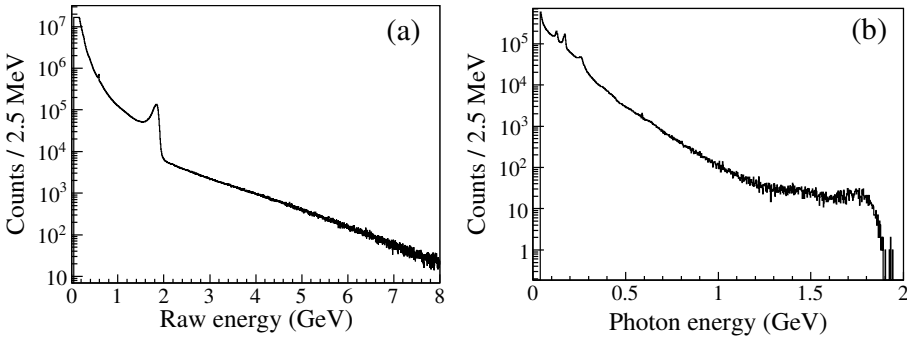


*Figure 7.11: Shower-energy spectrum measured using the EMC: (a) without any selection criteria and (b) after selection of only two photons.*

1. Events with two photons,
2. Energy sum of the two photons between 0.52 GeV to 0.62 GeV,
3. Excluded two-photon invariant mass region of:
   - $\pi^0$: 0.11 GeV/c$^2$ to 0.15 GeV/c$^2$,
   - $\eta$: 0.51 GeV/c$^2$ to 0.59 GeV/c$^2$,
4. Only two charged-tracks with invariant mass of $J/\psi$ between 3.0 GeV/c$^2$ to 3.2 GeV/c$^2$.

The first three selection criteria require only EMC information. After applying the first selection criterium the resulting photon-energy spectrum is shown in Fig. 7.11 (b). Only with this cut applied the signal photons are visible on top of a large background. The effect of the first event-selection criterium (*cut*1) on the total number of raw events (*NevRaw*) registered in the EMC is shown in Table 7.1. The first selection reduced the number of events by almost two orders of magnitude and the signal-to-background (SBR) ratio is significantly improved by about three orders of magnitude. The second selection restricts the two-

| event selection | number of events | SBR | | |
|---|---|---|---|---|
| | | $\psi^{'} \rightarrow \gamma\chi_{c2}$ | $\psi^{'} \rightarrow \gamma\chi_{c1}$ | $\psi^{'} \rightarrow \gamma\chi_{c0}$ |
| *NevRaw* | $2.02 \cdot 10^9$ | $4.7 \cdot 10^{-4}$ | $2.3 \cdot 10^{-4}$ | $2.5 \cdot 10^{-5}$ |
| *cut*1 | $1.40 \cdot 10^7$ | 0.20 | 0.40 | 0.20 |
| *cut*2 | $1.68 \cdot 10^6$ | 0.45 | 0.68 | 0.21 |
| *cut*3 | $1.07 \cdot 10^6$ | 0.54 | 0.78 | 0.48 |
| *cut*4 | $2.51 \cdot 10^5$ | 2.1 | 2.2 | 0.64 |

*Table 7.1: Change in the number of events and signal-to-background ratio (SBR) with subsequent event-selection criteria. The table is explained in the text*

photon energy sum window from 0.52 GeV to 0.62 GeV. The two-photon energy sum distribution obtained by selecting two photons is shown in Fig. 7.12 (a). The selected energy-sum window represents the energy difference between the charmonium states $\psi^{'}$ and $J/\psi$ (see Fig. 3.3) which is about 0.589 GeV [24] for the decay channel of interest. The photon-energy spectrum resulting after the first and second selection criteria is shown in Fig. 7.12 (d). The effect of the first

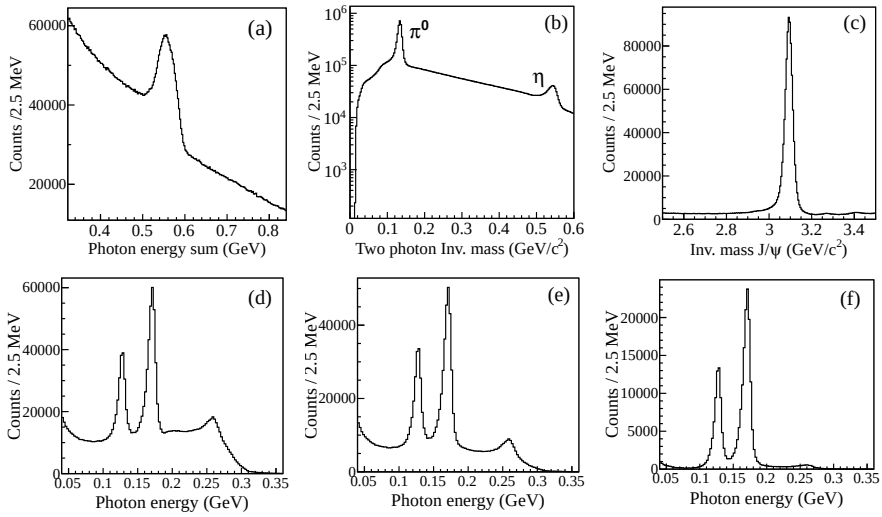


*Figure 7.12: Three event-selection criteria are applied subsequently on the spectra (a) Energy sum of larger- and smaller-energy photons, (b) Two-photon invariant-mass distribution, and (c) Two-lepton ($e^+e^-$ and $\mu^+\mu^-$) invariant-mass distribution of $J/\psi$. The corresponding effect of each event-selection criterium on the photon-energy spectrum is shown in panels d-f.*

two selections (*cut*2) on the previous number of events is shown in Table 7.1. The background events are reduced, thus improving the signal-to-background ratio seen in Fig. 7.12 (d) as compared to the distribution shown in Fig. 7.11 (b). The two-photon invariant-mass distribution is shown in Fig. 7.12 (b). The distribution is obtained by selecting only two photons and the $\pi^0$ and $\eta$ peaks are clearly visible. The $\pi^0$ and $\eta$ decay into two photons and may contribute to the background. Hence, in the third selection criterium, the photons in the invariant-mass region of $\pi^0$ and $\eta$ are excluded. The photon energy spectrum resulting after the first three selection criteria is shown in Fig. 7.12 (e). The effect of the first three selections (*cut*3) on the number of raw events is shown in Table 7.1. A factor of almost 1.6 reduction in the number of events is observed after *cut*3 and SBR is improved. In conclusion, after applying the first three event-selection criteria using only the EMC information the signal-to-background ratio is improved by almost three orders of magnitude (see Table 7.1). These three selection criteria do not involve precise tracking and are simple and very effective for application in

the on-line event-selection of the trigger-less readout chain of the PANDA EMC.

The forth and last selection criterium is based on the charged-track information obtained from the MDC. The selection includes only two-charged particles and the $J/\psi$ invariant-mass window between 3.0 GeV/c$^2$ and 3.2 GeV/c$^2$. The $J/\psi$ invariant-mass distribution is shown in Fig. 7.12 (c). The photon energy spectrum resulting after all the selection criteria is shown in Fig. 7.12 (f). The effect of all the selections (*cut*4) on the number of raw events and on the signal-to-background ratio is shown in Table 7.1. One order of magnitude difference is observed compared to the previous number of events for *cut*3 and the signal-to-background ratio is significantly improved. After using these four simple event-selection criteria the background is significantly reduced but not completely removed. To test the usefulness of the above selection criteria for the physics analysis, the product branching fractions of radiative transitions $\psi^{'} \rightarrow \gamma(\gamma J/\psi)_{\chi_{cJ}}$ $(J = 0, 1, 2)$ are estimated and compared with an advanced off-line analysis. The details of these studies are presented in the following section.

### Signal and background shape and detection efficiency

The background-reduced photon-energy spectrum for charmonium radiative transitions $\psi^{'} \rightarrow \gamma\chi_{cJ}$ $(J = 0, 1, 2)$ is shown in Fig. 7.13. A fit to the signal shapes is performed by an asymmetric Gaussian function [135] and the background shape is approximated by a forth-order polynomial. A detailed MC simulation of the BESIII detector based on Geant4 [78] is used to determine detection efficiencies, signal shapes, and contribution of background. The production of the $\psi^{'}$ resonance is simulated using the KKMC event generator [132]. Simulated events pass the same reconstruction algorithms and event-selection criteria as the measured data. To obtain the detection efficiency and the signal shapes, in total 400,000 events were simulated. The data and MC comparison of the signal shapes is shown in Fig. 7.14. The MC simulation reproduces the peak positions and widths of all three signal shapes and hence agrees satisfactorily with the measured data. The number of $\chi_{cJ}$ $(J = 0, 1, 2)$ signal events $(N_{Sev})$ and the detection efficiencies $(E_f)$ are listed in Table 7.2. The signal events are obtained from the background-subtracted signal-shape distribution of data shown in Fig. 7.14. The detection

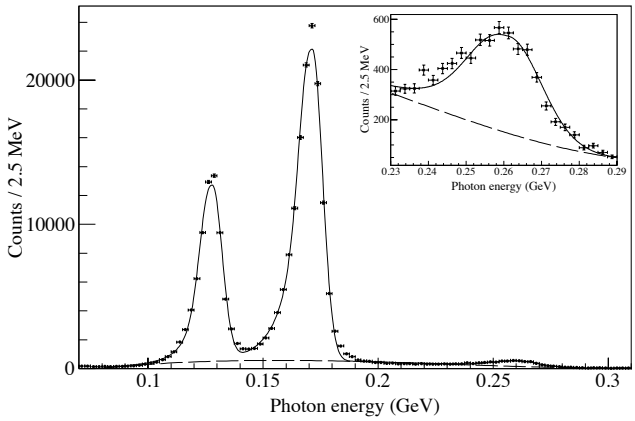


*Figure 7.13: Radiative-photon energy spectrum from $\psi' \to \gamma\chi_{cJ}$. The solid line shows a fit to the photon-energy spectrum performed by an asymmetric Gaussian function [135] and the dashed curve shows the background shape by a forth-order polynomial. The inset spectrum shows the photon energy region around 0.26 GeV.*

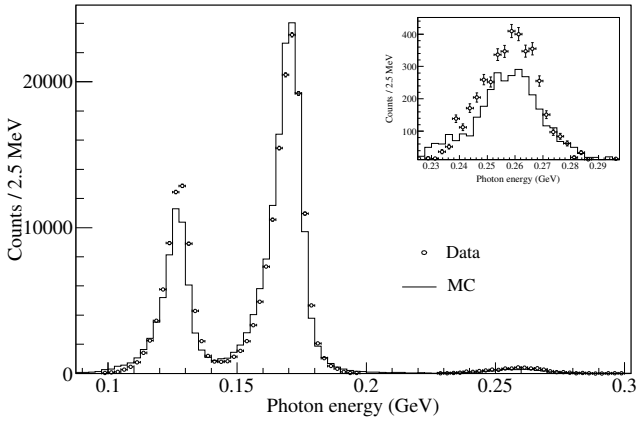


*Figure 7.14: Comparison of measured data and Monte Carlo (MC) simulations for the radiative-photon energy spectrum from $\psi' \to \gamma\chi_{cJ}$ $(J = 0, 1, 2)$. The spectrum is obtained after background subtraction. The solid line and the circles show MC and data points, respectively. The inset spectrum shows the photon energy region around 0.26 GeV.*

| Channel | $N_{Sev}$ | $E_f$ (%) |
|---|---|---|
| $\gamma(\gamma J/\psi)_{\chi_{c0}}$ | $4098 \pm 64$ | 23.7 |
| $\gamma(\gamma J/\psi)_{\chi_{c1}}$ | $136200 \pm 369$ | 32.6 |
| $\gamma(\gamma J/\psi)_{\chi_{c2}}$ | $72560 \pm 269$ | 32.0 |

*Table 7.2: The number of $\chi_{cJ}$ signal events $N_{Sev}$ and the detection efficiency $E_f$ for the transitions with $J$ = 0, 1, 2.*

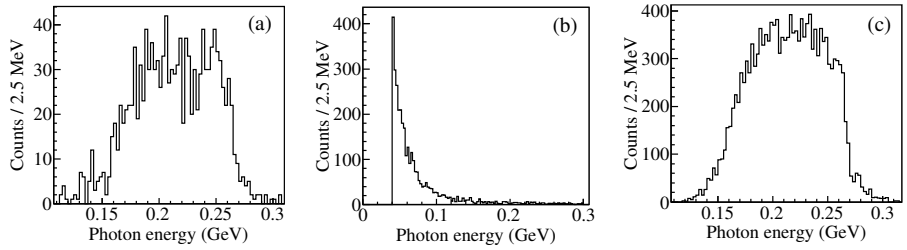


*Figure 7.15: Simulated background photon spectra for (a) $\psi' \to \pi^0\pi^0 J/\psi$, (b) $\psi' \to \pi^0 J/\psi$, and (c) $\psi' \to \eta J/\psi$. The $\pi^0$ and $\eta$ decay to two photons ($\gamma\gamma$) and $J/\psi$ to a lepton pair ($l^+l^-$), where $l$ denotes $e$ or $\mu$.*

efficiency is obtained from the MC simulations. The efficiency is calculated as the number of events remaining after the event-selection over the total number of events simulated.

The expected background contributions [24] in the signal region ($\chi_{cJ}$) mainly originate from three $\psi'$ decay modes: $\psi' \to \pi^0\pi^0 J/\psi$, $\psi' \to \pi^0 J/\psi$, and $\psi' \to \eta J/\psi$, where $\eta$ and $\pi^0$ decay in two photons. These background shapes are simulated using 400,000 events each and are shown in Fig. 7.15. These spectra show that there is no peaking background in the signal region. The normalized number of background signal events ($N^X_{Bev}$) for the background channel $X$ is estimated using the following equation:

$$N^X_{Bev} = \frac{N^X_{BSev}}{N_{MC} \cdot N_{\psi'} \cdot B(\psi' \to XJ/\psi) \cdot B(X \to \gamma\gamma) \cdot B(J/\psi \to l^+l^-)} \qquad (7.1)$$

where $N^X_{BSev}$ is the number of events in the signal region deduced from each background spectrum shown in Fig. 7.15, $N_{MC}$ is the number of simulated events

| Channel X | $N^X_{Bev}$ |
|---|---|
| $\psi^{'} \to \pi^0\pi^0 J/\psi$ | 2619 |
| $\psi^{'} \to \pi^0 J/\psi$ | 128 |
| $\psi^{'} \to \eta J/\psi$ | 4217 |

*Table 7.3: Expected total number of background events $N^X_{Bev}$ for background channel X in the $\chi_{cJ}$ $(J = 0, 1, 2)$ signal regions as derived from MC simulations.*

equal to 400,000 events, and $N_{\psi'}$ is the experimental number of $\psi^{'}$ determined to be $106.41 \cdot 10^6$ [138]. $B(\psi^{'} \to XJ/\psi)$ is the branching fraction of $\psi^{'}$ decays to $J/\psi$ via $X$ which stands for $\eta$ or $2\pi^0(4\gamma)$ or only $\pi^0$. $B(X \to \gamma\gamma)$ is the branching fraction of $X$ decaying to two photons. $B(J/\psi \to l^+l^-)$ is the branching fraction of $J/\psi$ decaying to a lepton pair $(l^+l^-)$, where $l$ denotes $e$ or $\mu$. The numbers of background signal events $(N^X_{Bev})$ for each background channel $X$ are listed in Table 7.3. The estimated number of background events in the signal region is very small as compared to the sum of the number of signal events shown in Table 7.2.

### Branching fractions and ratios

The product branching fractions of $\psi^{'} \to \gamma(\gamma J/\psi)_{\chi_{cJ}}$ $(J = 0, 1, 2)$ are estimated using the following equation:

$$B(\psi^{'} \to \gamma(\gamma J/\psi)_{\chi_{cJ}}) = \frac{N_{Sev}}{E_f \cdot N_{\psi'} \cdot B(J/\psi \to l^+l^-)} \tag{7.2}$$

where $N_{Sev}$ is the number of $\chi_{cJ}$ signal events and $E_f$ is the detection efficiency shown in Table 7.2. $N_{\psi'}$ is the number of $\psi^{'}$ determined to be $106.4 \cdot 10^6$ [138]. $B(J/\psi \to l^+l^-)$ is the branching fraction of $J/\psi$ decays to a lepton pair $(l^+l^-)$, where $l$ denotes $e$ or $\mu$. The obtained product branching fractions and branching ratios are shown in Table 7.4 and 7.5, respectively.

The values obtained in this work using simple event-selection criteria for the on-line analysis are very well comparable with the product branching fractions reported in [139] using more advanced and complex analysis techniques on the same data set. Also the estimated values in this work are comparable with the values

| Channel | $B^{this\ work}$ ($\times 10^{-4}$) | $B^{BESIII}$ ($\times 10^{-4}$) | $B^{PDG}$ ($\times 10^{-4}$) |
|---|---|---|---|
| $\gamma(\gamma J/\psi)_{\chi_{c0}}$ | $13.7 \pm 0.21_{stat}$ | $15.1 \pm 0.3_{stat} \pm 1.0_{sys}$ | $11.2 \pm 0.9$ |
| $\gamma(\gamma J/\psi)_{\chi_{c1}}$ | $330.7 \pm 0.89_{stat}$ | $337.7 \pm 0.9_{stat} \pm 18.3_{sys}$ | $316.5 \pm 19.7$ |
| $\gamma(\gamma J/\psi)_{\chi_{c2}}$ | $179.2 \pm 0.66_{stat}$ | $187.4 \pm 0.7_{stat} \pm 10.2_{sys}$ | $170.4 \pm 9.9$ |

*Table 7.4: The comparison of the product branching fractions B from eq. 7.2 determined in this work by on-line criteria with those published in [139] by the BESIII collaboration and in the PDG [24].*

| Ratio | $BR^{this\ work}$ (%) | $BR^{BESIII}$ (%) | $BR^{PDG}$ (%) |
|---|---|---|---|
| $R_{21} \equiv \frac{B_{\chi_{c2}}}{B_{\chi_{c1}}}$ | $54.18 \pm 0.24_{stat}$ | $55.47 \pm 0.26_{stat} \pm 0.11_{sys}$ | $53.83 \pm 4.5$ |
| $R_{01} \equiv \frac{B_{\chi_{c0}}}{B_{\chi_{c1}}}$ | $4.13 \pm 0.07_{stat}$ | $4.45 \pm 0.09_{stat} \pm 0.18_{sys}$ | $3.53 \pm 0.36$ |
| $R_{02} \equiv \frac{B_{\chi_{c0}}}{B_{\chi_{c2}}}$ | $7.63 \pm 0.12_{stat}$ | $8.03 \pm 0.17_{stat} \pm 0.33_{sys}$ | $6.57 \pm 0.65$ |

*Table 7.5: The comparison of the Branching Ratios (BR) determined in this work with those published in [139] by the BESIII collaboration and in the PDG [24].*

published in the particle data book (PDG). Therefore, the reported analysis results demonstrate that the simple event-selection criteria can advantageously be used in the compute-node stage of the PANDA experiment for the on-line event selection.

## 7.5 Summary and conclusion

In this chapter, two important issues, namely clustering and simple event selection criteria are tested for the possible application in the on-line data processing of the PANDA experiment. The different clustering algorithms are studied to achieve the best possible shower-energy reconstruction and hence optimal energy resolution. The clustering methods such as e3 $\times$ 3, e5 $\times$ 5, Dynamic Sum, and improved Dynamic Sum with cutoff threshold are tested using single-photon sim-

ulations. The simulation results reveal that the improved Dynamic Sum method is superior to the other mentioned methods, although the improvement in the energy resolution is marginal compared to e5 $\times$ 5 and Dynamic sum. The Dynamic sum method requires less computational steps to obtain the shower energy as compared to the other methods. Therefore, the Dynamic sum method can be used in the compute node stage of the PANDA EMC readout chain.

The performance of simple event-selection criteria and their physics evaluation is studied using the BESIII experimental data sample generated by performing $e^+e^-$ annihilations in the charmonium mass region. In the event selection we have demonstrated that by using only the EMC information the signal-to-background ratio can be improved significantly by more than three orders of magnitude. Moreover, to demonstrate the usefulness of the event-selection criteria for the physics analysis, the product branching fractions of charmonium radiative transitions $\psi^{'} \rightarrow \gamma\,(\gamma\, J/\psi)_{\chi_{cJ}}$ $(J = 0, 1, 2)$ are estimated and compared with results from an advanced off-line analysis. These analysis studies showed that the obtained values of product branching fractions and branching ratios are very well comparable with the values estimated using complex analysis techniques. Hence, the reported event-selection criteria can be safely and advantageously used in the trigger-less readout chain of the PANDA EMC for the on-line event selection.

# Chapter 8

# Summary and outlook

At the short-distance scale, the Standard Model (SM) has been very successful in predicting the interactions of quarks and leptons and provides a very good description of phenomena observed by experiments. Despite the success of the SM, it is still an incomplete theory. As an example, at the long-distance scale of QCD at low energies, phenomena such as quark confinement in the nonperturbative regime, the possible existence of glueballs, exotic mesons and hybrids, and the origin of hadron masses are yet to be completely understood.

The spectroscopy of glueballs and mesons in the charmonium mass region and above the open-charm threshold region (see Fig. 2.2) can help to improve the understanding of yet speculative phenomena and hence the nature of the strong interaction. The charmonium system is particularly suited because of the high mass of the charm quark, allowing a description of the dynamical properties of the charmonium system in terms of a non-relativistic potential model with relativistic corrections such as the spin-orbit and spin-spin interactions (see section 2.2). The free parameters in this model are to be determined from a comparison with experimental data [8].

In this context, the BESIII and PANDA experiments are designed to discover and study precisely the charmonium and open-charm resonances and their decay properties. The BESIII experiment is currently running and has already collected a wealth of data by performing $e^+e^-$ annihilations in the charmonium mass region. In $e^+e^-$ annihilation only states with quantum number $J^{PC} = 1^{--}$ can

be formed directly. However, in the future PANDA experiment using $\bar{p}p$ annihilations, charmonium states with all quantum numbers including $J^{PC} = 1^{--}$ can be formed directly. This direct formation will allow high-precision studies of the mass and the width of the charmonium states. Moreover, the PANDA experiment will operate at center-of-mass energies between 2 and 14 GeV. This broader energy range will help to study the charmonium spectrum above the open-charm threshold.

The work presented in this thesis is mainly concerned with the Electromagnetic Calorimeter (EMC) of both the BESIII and the PANDA experiment. The EMC is used for the energy, time and position measurement of photons, electrons, and neutral mesons decaying from various charmonium states (see Fig. 3.3). In modern collider or fixed-target experiments, the EMC is generally built from thousands of inorganic scintillating crystals. The incident particles lose their energy by creating an electromagnetic (EM) shower in the crystals. These EM showers are then detected by collecting scintillation light using photosensors (APDs/VPT/VPTT/SiPM). The photosensor signals are further amplified using pre-amplifiers and these amplified analog signals are converted into digital signals using ADCs. The Feature-Extraction (FE) algorithms are used to obtain features of these digitized signals. Since the incident particle creates an EM shower spread over a number of connected crystals, clustering algorithms are employed to reconstruct the EM shower energy and hence the energy of the incident particle. These reconstructed shower energies are further used for the physics analysis. The research carried out in this thesis covers almost all the topics which play a role in the above discussed chain from building a prototype EMC to the shower-energy reconstruction algorithms and their application in the physics analysis.

In the PANDA experiment, one of the important milestones was the development and verification of the Front-End Electronics (FEE), the corresponding FE algorithms and the readout chain without any hardware trigger. The project completed in the presented thesis research has two main challenges: the high hit-rate capability and the reliable on-line data processing without any hardware trigger.

The first challenge arises due to the high $\bar{p}p$ annihilation rate of 20 MHz, resulting in single-crystal hit-rates of more than 500 kHz (see Fig. 8.1 left panel) for the forward endcap EMC. This high hit rate will lead to EMC signal overlap (pile-up) and hence there is the danger of losing information due to signal overlap.

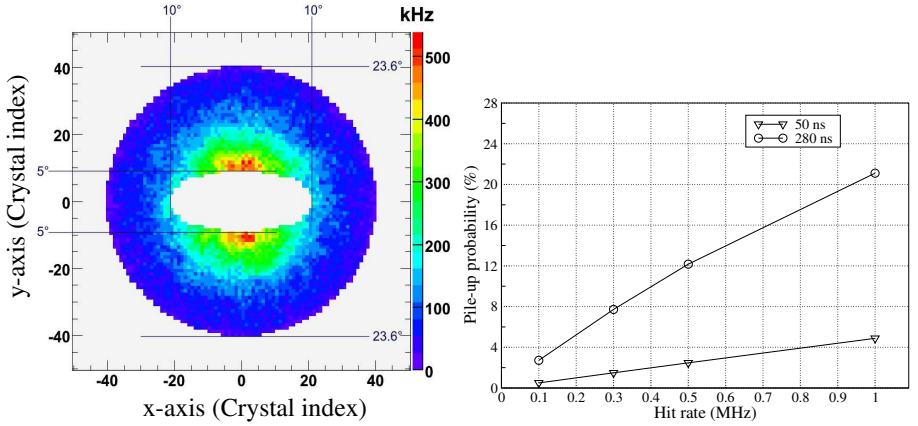


*Figure 8.1: Left panel: integrated single-crystal hit rate [12] as a function of vertical and horizontal coordinates for the forward endcap EMC simulated using the Dual Parton Model. Right panel: the pile-up probability as a function of the EMC hit rate estimated using a Poisson time-distribution function.*

Therefore, as a part of the FE algorithms, the pulse pile-up identification and recovery method has been developed and successfully tested using simulated and experimental pile-up signals.

The pile-up identification and recovery method, its in-beam validation and the results are discussed in chapter 5 and 6. The simulation studies show that the pile-up identification efficiency is almost 100% with a false rate of less than 1%. The pile-up identification algorithm is implemented in FPGA and successfully tested in EMC prototype experiments with tagged photons (see chapter 6). For the forward endcap EMC, the calculated pile-up probability (see Fig. 8.1 right panel) at a hit rate of 500 kHz is 12% for a pulse length of 280 ns. According to the PANDA EMC requirement, the pile-up probability should be close to 1%. The test of the pile-up recovery method reveals that the pile-up pulse amplitude can be completely recovered up to a minimum time difference equal to the pulse rise time. In the present studies the pulse rise time was 50 ns. Therefore, the pile-up probability of 12% is reduced to 2.4%.

As mentioned earlier, the EM shower develops over a bunch of neighboring crystals (crystal matrix or cluster). Therefore, to test the performance of the recovery algorithm on the cluster level, the pulse pile-up was simulated for single

($5 \times 5$ cluster) as well as two overlapping showers (see section 5.3.4). The estimated probabilities for the occurrence of two overlapping showers vary between 1% and 41% for maximum and peripheral overlap, respectively. The effective energy resolution is obtained by properly weighting the pile-up recovered energy resolutions and the reference energy resolutions for a $5 \times 5$ cluster. A little deterioration is observed in the effective energy resolution; for example at 1 GeV and for an EMC hit rate of 1 MHz a change from 2.48% to 2.5% is observed. In conclusion, the reported method for energy and time recovery is simple and effective and could be easily implemented in FPGAs. The simplicity of the method will require a minimum of FPGA resources and eventually reduce the power consumption.

In the second part of the thesis, for the first time in the PANDA EMC collaboration, the complete readout chain without any hardware trigger is demonstrated with tagged photons. The test was performed using a prototype of nine PWO-II crystals (proto9) completely developed at KVI in collaboration with the PANDA EMC group. Using only the time-stamp information, the correlation of the detector hits with the tagger information was achieved (see Fig. 8.2). The measured mean amplitude values are proportional to the true photon energies. This observation demonstrates that the event-identification procedure works properly and the response of the detection system is linear. The performance of the prototype

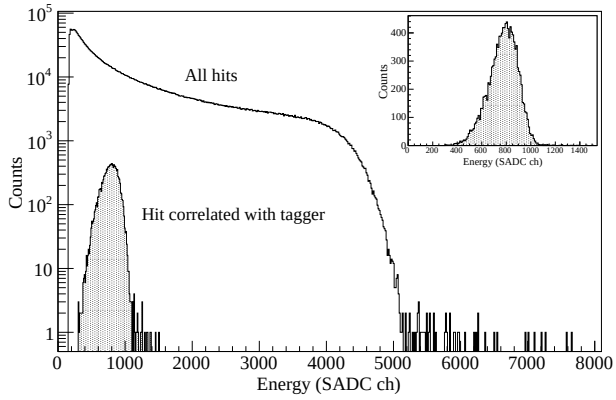


*Figure 8.2: Comparison of all hits and hits correlated with the tagger (shaded area): distributions of the energy deposition measured in a single crystal for 50 MeV energy photons at 5 kHz detector hit rate. The inset panel shows the vertical axis of the shaded spectrum on a linear scale.*

readout chain was evaluated for different detector hit rates from a few kHz up to 440 kHz. The readout chain worked reliably up to hit rates of about 440 kHz for a waveform length of 800 ns.

In the last part of the thesis, two important issues, namely clustering and simple event-selection criteria are tested for the possible application in the on-line data processing of the PANDA experiment (see chapter 7). These two challenges will play a crucial role in the on-line and trigger-less data processing of the PANDA experiment. In the first issue, the clustering methods such as e3 $\times$ 3, e5 $\times$ 5, Dynamic Sum, and improved Dynamic Sum with cutoff threshold are evaluated using single-photon simulations. The simulation studies show that, because of simplicity and almost equivalent performance compared to e5 $\times$ 5, the Dynamic sum method can be used in the compute node stage of the PANDA EMC readout chain for the EM shower energy reconstruction.

In the second issue, the performance of simple event-selection criteria and their physics evaluation are studied using a BESIII experimental data sample. The simple event-selection demonstrates that by just using only the EMC information the background can be suppressed significantly by almost three orders of magnitude and a very good signal-to-background ratio can be achieved (see Fig. 8.3). Moreover, to demonstrate the usefulness of the simple event-selection criteria for the physics analysis, the product branching fractions of the charmonium radiative transitions $\psi^{'} \rightarrow \gamma\ (\gamma\ J/\psi)_{\chi_{cJ}}$ $(J = 0, 1, 2)$ are estimated. The

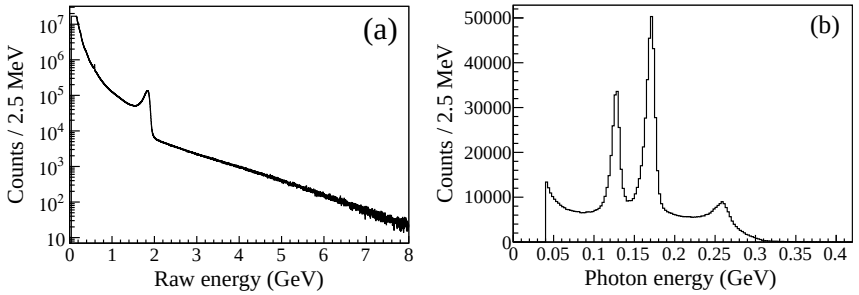


*Figure 8.3: The BESIII EMC shower energy spectrum: (a) raw without any selection and (b) with event-selection requiring only two photons, a two-photon energy-sum window between 0.52 GeV and 0.62 GeV, and excluded a two-photon invariant-mass window for $\pi^0$ and $\eta$ between 0.11 and 0.15 GeV/$c^2$ and between 0.51 and 0.59 GeV/$c^2$, respectively.*

obtained values of product branching fractions and branching ratios are very well comparable with the values measured using complex analysis techniques. Hence, the reported simple event-selection criteria can be safely and advantageously used in the trigger-less readout chain of the PANDA EMC for the on-line event selection. The projects completed in this thesis work are very important milestones for the PANDA EMC and its near-future operation in the PANDA experiment. In general, the pile-up identification and its recovery algorithms can be applied for crystal-based detectors, which will operate in a high counting-rate environment.

# Samenvatting

Het Standaard Model (SM) van elementaire deeltjes en krachten voorspelt erg succesvol de interacties tussen quarks en leptonen op korte afstand en beschrijft experimentele observaties met een hoge precisie. Ondanks het succes van het SM is het een incomplete theorie. Een voorbeeld hiervan is het regime van de Quantum Chromodynamica (QCD) bij lage energieën. Fenomenen in dit regime zoals quark confinement, de oorsprong van hadron massas en het mogelijke bestaan van glueballs, exotische mesonen en hybriden zijn nog niet volkomen begrepen.

De spectroscopie van glueballs en mesonen rond de energie van de charmonium massa en boven de open-charm drempel (zie Figuur 2.2) wordt gezien als een sleutel voor het begrijpen van nog niet doorgronde fenomenen en daarmee het gedrag van de sterke interactie. Charmonium is hier uitzonderlijk geschikt voor vanwege de hoge massa van de charm quark. Deze staat een beschrijving van de dynamische eigenschappen van charmonium toe in termen van een niet-relativistisch potentiaal model (zie sectie 2.2). De vrije parameters van dit model zouden moeten worden bepaald na vergelijking met experimentele gegevens [8].

In deze context zijn de BESIII en PANDA experimenten ontworpen om de charm-rijke resonanties en verval eigenschappen te ontdekken en te bestuderen. Het BESIII experiment is momenteel gaande en heeft al een schat aan gegevens opgeleverd door elektronen en positronen te annihileren bij energieën rond de charmonium massa. Bij dit proces kunnen alleen toestanden met de kwantum getallen $J^{PC} = 1^{--}$ direct worden gevormd. In de toekomst zal het PANDA experiment echter alle charmonium toestanden direct kunnen vormen door protonen en antiprotonen te laten annihileren. Het direct kunnen vormen van deze toestanden laat hoge-precisie metingen toe aan de massa en levensduur van charmonium toestanden. Daarbij zal het PANDA experiment gaan opereren bij mas-

samiddelpunt energieën van 2 tot 14 GeV. Deze bredere dekking van energieën zal helpen bij het bestuderen van het charmonium spectrum boven de open-charm drempel.

Het werk in dit proefschrift houdt zich vooral bezig met de Elektromagnetische Calorimeter (EMC) van zowel het BESIII als het PANDA experiment. De EMC wordt gebruikt voor energie, tijd en positie metingen aan fotonen, elektronen en neutrale mesonen die voortkomen uit het verval van charmonium toestanden (zie Figuur 3.3). In moderne botsingsexperimenten (van het collider of fixed-target type) is de EMC meestal opgebouwd uit duizenden anorganische scintillerende kristallen. De inkomende deeltjes verliezen hun energie door het veroorzaken van een elektromagnetische (EM) lawine. Deze EM lawines worden gedetecteerd door het verzamelen van scintillatielicht in fotosensoren (APDs/VPT/VPTT/SiPM). De signalen van deze sensoren worden versterkt door gebruik te maken van voorversterkers en deze analoge signalen worden omgezet in digitale signalen met behulp van Analoog naar Digitaal Converters (ADCs). Snelle Feature-Extractie (FE) algoritmes worden gebruikt om reeds *online* kenmerken van de gedigitaliseerde signalen te verkrijgen. Omdat de inkomende deeltjes EM lawines veroorzaken die zich over meerdere kristallen uitspreiden worden cluster algoritmes gebruikt om de energie van de lawine en daarmee het inkomende deeltje te reconstrueren. De gereconstrueerde energie wordt later gebruikt in fysica analyses. Het onderzoek dat uitgevoerd is in dit proefschrift dekt bijna alle onderwerpen die een rol spelen in het bovengenoemde, van het bouwen van een prototype EMC tot de reconstructie algoritmes voor de energie van EM lawines en de toepassing daarvan in fysica analyses.

Een van de belangrijkste mijlpalen van het PANDA experiment was de ontwikkeling en verificatie van de Front-End Elektronica (FEE), de bijbehorende FE algoritmes en het uitlees mechanisme zonder hardware trigger. Het voltooide project dat in dit proefschrift wordt gepresenteerd had twee belangrijke uitdagingen: de hoge hit-frequentie bekwaamheid en het betrouwbaar online verwerken van gegevens zonder hardware trigger.

De eerste uitdaging komt voort uit de verwachte hoge proton-antiproton annihilatie frequentie van 20 MHz, dat leidt tot hit-rates van 500 kHz (zie het linkerpaneel in Figuur 8.1) in de kristallen van de voorwaartse eindkap EMC. Deze hoge hit-rate heeft signaal-overlap (pile-up) tot gevolg met als consequentie dat er informatie verloren kan gaan. Vanwege dit risico is, als deel van de FE algoritmes, de puls pile-up identificatie en herstel methode ontwikkeld en met

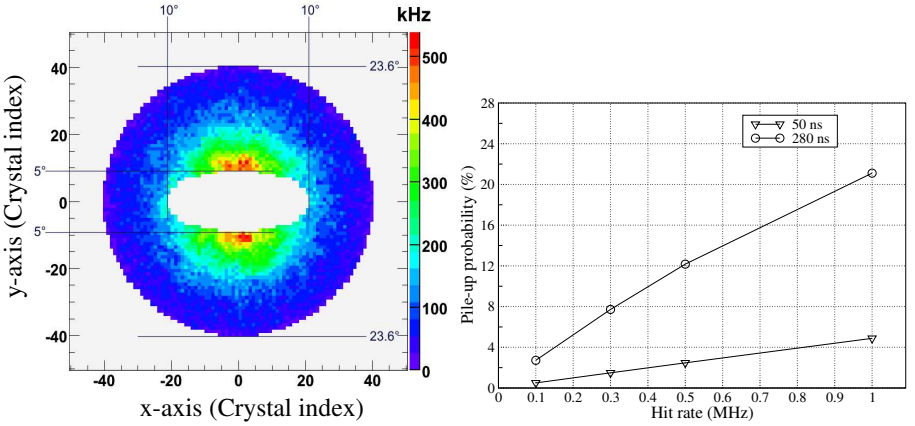


*Figuur 8.1: Linker paneel: geïntegreerde hit frequentie in enkele kristallen [12] als een functie van de horizontale en verticale coördinaten voor de voorwaartse eind kap EMC, gesimuleerd op basis van het Dual Parton Model. Rechter paneel: de pile-up waarschijnlijkheid als functie van de EMC hit frequentie, geschat op basis van een Poisson functie voor de tijdsverdeling.*

succes getest op gesimuleerde en experimentele pile-up signalen.

De pile-up identificatie en herstelmethode, haar in-bundel bevestiging en de resultaten worden besproken in hoofdstuk 5 en 6. Het simulatie onderzoek toont aan dat de efficientie van pile-up identificatie bijna 100% is met een fout-positief frequentie van minder dan 1%. De pile-up identificatie algoritme is in FPGA geïmplementeerd en met succes getest in EMC prototype experimenten met gelabelde fotonen (zie hoofdstuk 6). Voor de voorwaartse eindkap EMC is de berekende pile-up waarschijnlijkheid 12% (zie Figuur 8.1 rechter paneel) bij een hit frequentie van 500 kHz en een pulslengte van 280 ns. Volgens de PANDA EMC vereisten zou de pile-up waarschijnlijkheid rond 1% moeten zijn. De test van de pile-up herstel methode toont aan dat de pile-up pulshoogte volledig kan worden hersteld tot op een minimum tijdverschil gelijk aan de stijgtijd van de puls. In deze thesis was de stijgtijd van de puls gelijk aan 50 ns, waardoor de pile-up waarschijnlijkheid van 12% verminderd is tot een tevredenstellende waarde van 2.4%.

Zoals al eerder genoemd raakt de EM lawine meerdere naburige kristallen (kristal matrix of cluster). Om de prestatie van het herstel algoritme op cluster

niveau te testen is de puls pile-up gesimuleerd voor zowel enkele ($5 \times 5$ cluster) als twee overlappende lawines (zie sectie 5.3.4). De geschatte waarschijnlijkheden voor het plaatsvinden van twee overlappende lawines varieerde tussen 1% en 41% voor maximale en perifere overlap, respectievelijk. De effectieve energie resolutie is verkregen door het op de juiste manier wegen van de pile-up hersteldeen referentie-energieresoluties voor een $5 \times 5$ cluster. Er treedt een kleine verslechtering in de effectieve energie resolutie op; bijvoorbeeld bij 1 GeV en voor een EMC hit-frequentie van 1 MHz wordt een verandering van 2.48% naar 2.5% waargenomen. In conclusie is de besproken methode simpel en effectief en kan eenvoudig worden geïmplementeerd in FPGAs. Door de eenvoud van de methode is een minimum aan FPGA capaciteit nodig wat uiteindelijk het stroomverbruik zal verminderen.

In het tweede deel van dit proefschrift, voor het eerst in de PANDA EMC, wordt het complete uitleesmechanisme zonder hardware trigger gedemonstreerd met gelabelde fotonen. De test is uitgevoerd met een prototype van negen PWO-II kristallen (proto9), in het geheel ontwikkeld op het KVI in samenwerking met de PANDA EMC groep. Door alleen gebruik te maken van de tijdsgelabelde informatie, is er correlatie tussen de detector hits en tagger informatie bereikt (zie Figuur 8.2). De gemeten gemiddelde amplitude is proportioneel met de werkelijke foton energie. Deze observatie toont aan dat de procedure van event-

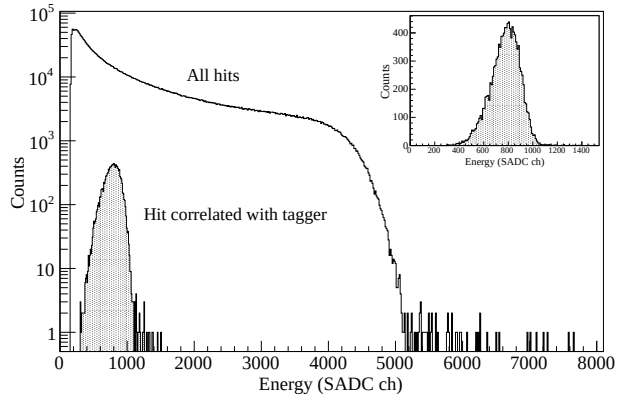


*Figuur 8.2: Vergelijking van alle hits en hits gecorreleerd met de tagger (het gearceerde spectrum): distributies van de energie depositie gemeten in een enkel kristal voor 50 MeV fotonen bij een hit-rate van 5 kHz. Het ingezette figuur laat het gearceerde spectrum zien op een lineaire schaal.*

identificatie naar behoren werkt en dat het gedrag van het detectie systeem lineair is. De prestaties van het prototype uitleesmechanisme is bekeken voor detector hit-rates van een paar kHz tot en met 440 kHz. Het uitleesmechanisme werkte betrouwbaar tot op hit-rates van ongeveer 440 kHz voor een golfvorm lengte van 800 ns.

In het laatste deel van dit proefschrift worden twee belangrijke kwesties, namelijk de clustering en de eenvoudige event-selectie criteria, getest voor een mogelijke toepassing in de online gegevens verwerking van het PANDA experiment (zie hoofdstuk 7). Deze twee uitdagingen zullen een cruciale rol spelen in het online en zonder trigger verwerken van gegevens in het PANDA experiment. Voor de eerste uitdaging worden clustering methodes zoals e3 $\times$ 3, e5 $\times$ 5, dynamische som, en verbeterde dynamische som met een afkapdrempel geëvalueerd met behulp van simulaties voor enkel-foton hits. De simulaties laten zien dat om reden van eenvoud en vanwege de bijna equivalente prestaties vergeleken met e5$\times$5, de dynamische som methode goed gebruikt kan worden voor de EM lawine reconstructie.

Voor de tweede uitdaging is de prestatie van eenvoudige event-selectie criteria en hun fysica evaluatie bestudeerd door gebruik te maken van experimentele gegevens van BESIII. De eenvoudige event-selectie laat zien dat, door alleen gebruik te maken van de EMC informatie, de achtergrond significant onderdrukt kan worden met bijna drie ordes van grootte en een goede signaal-achtergrond verhouding bereikt kan worden (zie Figuur 8.3). Om het nut van de eenvoudige

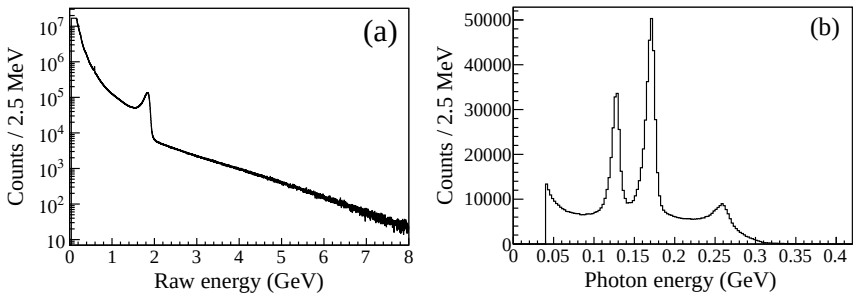


*Figuur 8.3: Het BESIII EMC lawine energie spectrum: (a) ruw zonder enige selectie en (b) met event-selectie met als enige vereisten twee fotonen, exclusief een twee-foton energie-som die tussen 0.52 GeV en 0.62 GeV ligt en een twee-foton invariante massa voor $\pi^0$ en $\eta$ die tussen 0.11 en 0.15 GeV/$c^2$ en 0.51 en 0.59 GeV/$c^2$, respectievelijk ligt.*

event-selectie criteria verder aan te tonen zijn de product branching fracties van de charmonium transities $\psi^{'} \rightarrow \gamma\ (\gamma\ J/\psi)_{\chi_{cJ}}$ $(J = 0, 1, 2)$ geschat. De verkregen waardes voor de product branching fracties en ratios zijn vergelijkbaar met de gemeten waardes verkregen met ingewikkeldere technieken. Concluderend kunnen de hier beschreven eenvoudige event-selectie criteria veilig en voordelig worden gebruikt in het uitleesmechanisme zonder trigger van de PANDA EMC voor de online event selectie. De projecten die in dit proefschrift zijn uitgevoerd zijn belangrijke mijlpalen voor de PANDA EMC en zullen worden gebruikt in het PANDA experiment in de nabije toekomst. In het algemeen kunnen de pile-up identificatie methode en haar herstel algoritmes worden toegepast in detectoren, die gebaseerd zijn op kristallen en die opereren in een omgeving met hoge telsnelheden.

# Bibliography


[1] W. N. Cottingham and D. A. Greenwood, An Introduction to the Standard Model of Particle Physics, Cambridge university press, ISBN-13 978-0-521-85249-4, 2007.

[2] Emmanuel A. Paschos, Electroweak theory, Cambridge university press, ISBN-13 978-0-521-86098-7, 2007.

[3] Walter Greiner, Stefan Schramm, and Eckart Stein, Quantum Chromodynamics, Third edition, Springer publication, ISBN-10 3-540-48534-1, 2007.

[4] G. Aad et al., Physics Letters B **716**, 1 (2012), http://www.sciencedirect.com/science/article/pii/S037026931200857X.

[5] S. Chatrchyan et al., Physics Letters B **716**, 30 (2012), http://www.sciencedirect.com/science/article/pii/S0370269312008581.

[6] W. Erni et al. (PANDA collaboration), Physics Performance Report for PANDA: Strong Interaction Studies with Antiprotons, http://arxiv.org/abs/0903.3905, 2009.

[7] D. M. Asner et al. (BESIII Collaboration), Physics at BES-III, http://arxiv.org/abs/0809.1869v1, 2008.

[8] Diego Bettoni and Roberto Calabrese, Progress in Particle and Nuclear Physics **54**, 615 (2005), http://www.sciencedirect.com/science/article/pii/S0146641004001255.

[9] BESIII collaboration, http://bes3.ihep.ac.cn/index.htm.

[10] PANDA collaboration, http://www-panda.gsi.de/.

[11] FAIR - Facility for Antiproton and Ion Research. Green Paper - The Modularized Start Version. Technical Report, http://www.fair-center.de/fileadmin/fair/publications_FAIR/FAIR_GreenPaper_2009.pdf, 2009.

[12] W. Erni et al. (PANDA collaboration), Technical Design Report for PANDA Electromagnetic Calorimeter, http://arxiv.org/abs/0810.1216, 2008.

[13] Johan Messchendorp for the BESIII collaboration, 13th International Conference on B-Physics at Hadron Machines - Beauty, Amsterdam, The Netherlands, 04 April 2011, http://arxiv.org/abs/1108.3047.

[14] M.B. Voloshin, Progress in Particle and Nuclear Physics **61**, 455 (2008), http://www.sciencedirect.com/science/article/pii/S0146641008000239.

[15] E. Eichten et al., Phys. Rev. D **21**, 203 (1980), http://link.aps.org/doi/10.1103/PhysRevD.21.203.

[16] Kenneth G. Wilson, Phys. Rev. D **10**, 2445 (1974), http://link.aps.org/doi/10.1103/PhysRevD.10.2445.

[17] V. Crede and C.A. Meyer, Progress in Particle and Nuclear Physics **63**, 74 (2009), http://www.sciencedirect.com/science/article/pii/S0146641009000052.

[18] Ulrich Wiedner, Progress in Particle and Nuclear Physics **66**, 477 (2011), http://www.sciencedirect.com/science/article/pii/S0146641011000822.

[19] Gunnar S. Bali, International Journal of Modern Physics A **21**, 5610 (2006), http://www.worldscientific.com/doi/abs/10.1142/S0217751X0603480X.

[20] Dong Chen et al., Nuclear Physics B - Proceedings Supplements **73**, 898 (1999), http://www.sciencedirect.com/science/article/pii/S0920563299852384.

[21] CP-PACS Project (Tsukuba Univerity), http://www.rccp.tsukuba.ac.jp/cppacs/project-e.html.

[22] Y. Chen et al., Phys. Rev. D **73**, 014516 (2006), http://link.aps.org/doi/10.1103/PhysRevD.73.014516.

[23] Jozef J. Dudek et al., Phys. Rev. D **83**, 111502 (2011), http://link.aps.org/doi/10.1103/PhysRevD.83.111502.

[24] Particle Data Book (PDG), http://pdg.lbl.gov/2012/html/computer_read.html, 2010.

[25] David J. Griffiths, Introduction to Electrodynamics, Third edition, Prentice-Hall, ISBN 0-13-805326-X, 1999.

[26] V.A. Novikov et al., Physics Reports **41**, 1 (1978), "http://www.sciencedirect.com/science/article/pii/0370157378901205.

[27] P. Spiller and G. Franchetti, Nucl. Instrum. and Meth. Phys. Res. A **561**, 305 (2006), http://www.sciencedirect.com/science/article/pii/S0168900206000507.

[28] GSI Helmholtzzentrum für Schwerionenforschung, http://www.gsi.de.

[29] FAIR - Facility for Antiproton and Ion Research, http://www.fair-center.eu/for-users.html.

[30] A. Dolinskii et al., Nucl. Instrum. and Meth. Phys. Res. A **629**, 16 (2011), http://www.sciencedirect.com/science/article/pii/S016890021002499X.

[31] A. Dolinskii et al., Nucl. Instrum. and Meth. Phys. Res. A **532**, 483 (2004), http://www.sciencedirect.com/science/article/pii/S016890020401294X.

[32] A. Lehrach et al., Nucl. Instrum. and Meth. Phys. Res. A **561**, 289 (2006), http://www.sciencedirect.com/science/article/pii/S0168900206000477.

[33] H. Stockhorst, Stochastic momentum cooling experiments with a barrier bucket cavity and internal targets at COSY-Juelich in preparation for HESR at FAIR, www.jacow.org/, 2010.

[34] K.-Th. Brinkmann, Nuclear Physics A **790**, 75c (2007), http://www.sciencedirect.com/science/article/pii/S0375947407002667.

[35] E. Eichten et al., Rev. Mod. Phys. **80**, 1161 (2008), http://link.aps.org/doi/10.1103/RevModPhys.80.1161.

[36] BELLE collaboration, http://belle.kek.jp/.

[37] BABAR collaboration, http://www.slac.stanford.edu/BF/.

[38] Particle Data Book, page no. 291-295, http://pdg.lbl.gov/2012/html/computer_read.html, 2010.

[39] M. Ablikim et al., Phys. Rev. Lett. **104**, 132002 (2010), http://link.aps.org/doi/10.1103/PhysRevLett.104.132002.

[40] W. Erni et al. (PANDA collaboration), Physics Performance Report for PANDA: Strong Interaction Studies with Antiprotons, section-4.2.2.6, page no. 82-84, http://arxiv.org/abs/0903.3905, 2009.

[41] N. Brambilla et al., Heavy quarkonium: progress, puzzles, and opportunities, http://arxiv.org/abs/1010.5827, 2011.

[42] T. Armstrong et al. (E-760 Collaboration), Phys. Rev. D **47**, 772 (1993), http://link.aps.org/doi/10.1103/PhysRevD.47.772.

[43] M. Ablikim et al. (BESIII Collaboration), Phys. Rev. Lett. **108**, 222002 (2012), http://link.aps.org/doi/10.1103/PhysRevLett.108.222002.

[44] Chen Y. et al., Phys. Rev. D **73**, 014516 (2006), http://link.aps.org/doi/10.1103/PhysRevD.73.014516.

[45] Progress in Particle and Nuclear Physics **57**, 564 (2006), http://www.sciencedirect.com/science/article/pii/S0146641005000761.

[46] T. Gaitanos et al., Nuclear Physics A **881**, 240 (2012), http://www.sciencedirect.com/science/article/pii/S0375947411007007.

[47] R. L. Jaffe, Phys. Rev. Lett. **38**, 617 (1977), http://link.aps.org/doi/10.1103/PhysRevLett.38.195.

[48] A. Alavi-Harati et al. (KTeV Collaboration), Phys. Rev. Lett. **84**, 2593 (2000), http://link.aps.org/doi/10.1103/PhysRevLett.84.2593.

[49] D. Oellers et al., Physics Letters B **674**, 269 (2009), http://www.sciencedirect.com/science/article/pii/S0370269309003268.

[50] G Ciullo et al., Journal of Physics: Conference Series **295**, 012150 (2011), http://iopscience.iop.org/1742-6596/295/1/012150/.

[51] W. Erni et al. (PANDA collaboration), Technical Design Report for the PANDA Internal Targets: The Cluster-Jet Target and Developments for the Pellet Target; submitted to FAIR, 2012.

[52] W. Erni et al. (PANDA collaboration), Technical Design Report for PANDA Micro Vertex Detector, http://panda-wiki.gsi.de/pub/Mvd/TalkOrPaperDrafts/panda_tdr_mvd.pdf, 2012.

[53] A. Smirnov et al., Proceedings of RuPAC 2008, Zvenigorod, Russia, accelconf.web.cern.ch/accelconf/r08/papers/MOAPH04.pdf.

[54] A. Smirnov et al., Proceedings of COOL 2009, Lanzhou, China, TH-PMCP002, cool09.impcas.ac.cn/JACoW/papers/thpmcp002.pdf.

[55] PANDA collaboration webpage, http://www-panda.gsi.de/framework/detector.php.

[56] W. Erni et al. (PANDA collaboration), Technical Design Report for the Solenoid and Dipole Spectrometer Magnets, http://arxiv.org/abs/0907.0169/, 2009.

[57] W. Erni et al. (PANDA collaboration), European Physical Journal A **49**, 25 (2013), http://dx.doi.org/10.1140/epja/i2013-13025-8.

[58] Lars Schmitt, Proposal for a Scintillator Tile Hodoscope for PANDA, http://panda-wiki.gsi.de/pub/Tof/SciTil/scitil.pdf, 2011.

[59] Compact Muon Solenoid (CMS) experiment at CERN's LHC, http://cms.web.cern.ch/.

[60] A Large Ion Collider Experiment (ALICE) at CERN's LHC, http://aliweb.cern.ch/.

[61] The Large Hadron Collider (LHC) at CERN, http://lhc.web.cern.ch/lhc/.

[62] European Organisation for Nuclear Research (CERN), http://public.web.cern.ch/public/.

[63] H. Loehner et.al, Nuclear Science, IEEE Transactions on **59**, 2237 (2012), http://ieeexplore.ieee.org/xpls/abs_all.jsp?arnumber=6170599.

[64] M. Kavatsyuk et al., Nucl. Instrum. and Meth. Phys. Res. A **648**, 77 (2011), http://www.sciencedirect.com/science/article/pii/S0168900211011600.

[65] P. Abbon et al., Nucl. Instrum. and Meth. Phys. Res. A **577**, 455 (2007), http://www.sciencedirect.com/science/article/pii/S0168900207005001.

[66] K. Ackerstaff et al., Nucl. Instrum. and Meth. Phys. Res. A **417**, 230 (1998), http://www.sciencedirect.com/science/article/pii/S0168900298007694.

[67] N Akopov et al., Nucl. Instrum. and Meth. Phys. Res. A **479**, 511 (2002), http://www.sciencedirect.com/science/article/pii/S0168900201009329.

[68] W. Erni et al. (PANDA collaboration), The technical design report of the PANDA Shashlyk calorimeter, http://btev.ihep.su/~paul/panda_tdr_FSC.pdf, 2012.

[69] Aleksandra Wronska (for the PANDA collaboration), Int. Jour. of Modern Physics A (IJMPA) **24**, 471 (2009), http://www.worldscinet.com/ijmpa/24/2402n03/S0217751X09043870.html.

[70] I. Konorov et al., IEEE NSS conference proceedings page no. 1863 (2009), http://ieeexplore.ieee.org/xpl/articleDetails.jsp?arnumber=5402172.

[71] W. Kühn et al., 15th IEEE-NPSS Real-Time Conference page no. 1 (2007), http://ieeexplore.ieee.org/xpl/articleDetails.jsp?arnumber=4382729.

[72] D. Munchow et al., 17th IEEE-NPSS Real-Time Conference page no. 1 (2010), http://ieeexplore.ieee.org/xpl/articleDetails.jsp?arnumber=5750453.

[73] M. Kavatsyuk et al., IEEE NSS conference proceedings page no. 43 (2011), http://ieeexplore.ieee.org/xpl/articleDetails.jsp?arnumber=6154360.

[74] The simulation and reconstruction framework for PANDA experiment, http://panda-wiki.gsi.de/cgi-bin/view/Computing/PandaRoot.

[75] FairROOT - The simulation and reconstruction framework, http://fairroot.gsi.de/.

[76] R. Brun and F. Rademakers, Nucl. Instrum. and Meth. Phys. Res. A **389**, 81 (1997), http://www.sciencedirect.com/science/article/pii/S016890029700048X.

[77] The Virtual Monte Carlo (VMC), http://root.cern.ch/drupal/content/vmc/.

[78] S. Agostinelli et al., Nucl. Instrum. and Meth. Phys. Res. A **506**, 250 (2003), http://www.sciencedirect.com/science/article/pii/S0168900203013688.

[79] BESIII Collaboration, Nucl. Instrum. and Meth. Phys. Res. A **598**, 7 (2009), http://www.sciencedirect.com/science/article/pii/S0168900208011790.

[80] M. Ablikim et al. (BESIII Collaboration), Nucl. Instrum. and Meth. Phys. Res. A **614**, 345 (2010), http://www.sciencedirect.com/science/article/pii/S0168900209023870.

[81] C. Zhang (for BEPC and BEPCII Teams), Performance of the BEPC and progress of the BEPCII: in proceedings of APAC Gyeongju, Korea, http://accelconf.web.cern.ch/accelconf/a04/PAPERS/MOM301.PDF, 2004.

[82] Cui Li (for the BESIII collaboration), Recent results of light hadron spectroscopy from BESIII, The 24th Rencontres de Blois, France, 2012.

[83] B. Aubert et al. (BABAR Collaboration), Phys. Rev. Lett. **98**, 211802 (2007), http://link.aps.org/doi/10.1103/PhysRevLett.98.211802.

[84] M. Staric et al. (Belle Collaboration), Search for CP Violation in D Meson Decays to phi pi+, http://arxiv.org/abs/1110.0694v2, 2011.

[85] N. Berger et al., Chinese Physics C **34(12)**, 1779 (2010), http://hepnp.ihep.ac.cn/qikan/manage/wenzhang/2010-0052.pdf.

[86] Fu Cheng-Dong et al., Chinese Physics C **32(5)**, 329 (2008), http://iopscience.iop.org/1674-1137/32/5/001.

[87] K. Kordas, Nuclear Physics B - Proceedings Supplements **172**, 178 (2007), http://www.sciencedirect.com/science/article/pii/S0920563207005865.

[88] Weidong Li et al., Proceeding of CHEP06, Mumbai, India (2006), http://indico.cern.ch/getFile.py/access?contribId=177&sessionId=3&resId=0&materialId=paper&confId=048.

[89] G. Barrand et al., Computer Physics Communications **140**, 45 (2001), http://www.sciencedirect.com/science/article/pii/S0010465501002545.

[90] CERNLIB - The CERN Program Library, http://cernlib.web.cern.ch/cernlib/.

[91] CLHEP - A Class Library for High Energy Physics, http://proj-clhep.web.cern.ch/proj-clhep/.

[92] J. Bogart, Calibration infrastructure for the GLAST LAT, Computing in HEP and NP, La Jolla, California, SLAC-PUB-9890, http://www.slac.stanford.edu/econf/C0303241/proc/papers/MOKT001.PDF, 2003.

[93] Christian W. Fabjan and Fabiola Gianotti, Rev. Mod. Phys. **75**, 1243 (2003), http://link.aps.org/doi/10.1103/RevModPhys.75.1243.

[94] Illustration of Electromagnetic shower development, http://www-zeus.physik.uni-bonn.de/~brock/feynman/vtp_ws0506/.

[95] Particle Data Book, page no. 320-321, http://pdg.lbl.gov/2012/html/computer_read.html, 2010.

[96] Hamamatsu company webpage, http://jp.hamamatsu.com/products/sensor-ssd/pd078/index_en.html.

[97] T. Ikagawa et al., Nucl. Instrum. and Meth. Phys. Res. A **538**, 640 (2005), http://www.sciencedirect.com/science/article/pii/S0168900204021758.

[98] B. Lewandowski et al., IEEE Trans. Nucl. Sci. **55**, page no. 1304 (2008), http://ieeexplore.ieee.org/xpl/articleDetails.jsp?arnumber=4545153.

[99] W. Erni and M. Steinacher, University of Basel, PANDA Technical Progress Report (Public), page 204-206, http://www-panda.gsi.de/framework/documents.php, 2005.

[100] Peter Wieczorek and Holger Flemming, IEEE NSS conference proceedings page no. 1319 (2010), http://ieeexplore.ieee.org/xpl/articleDetails.jsp?arnumber=5873982.

[101] Department of physics, Basel University, Switzerland, http://www.physik.unibas.ch/dept/pages/en/intro.htm.

[102] VHDL implementation: P.J.J.Lemmens, Shaper: F. Schreuder, (KVI), Groningen, 2010-12.

[103] E. Guliyev et al., Nucl. Instrum. and Meth. Phys. Res. A **664**, 22 (2012), http://www.sciencedirect.com/science/article/pii/S0168900211019267.

[104] Struck SADC-SIS3302, http://www.struck.de/sis3302.htm.

[105] P. Marciniewski et al., IEEE NSS conference proceedings page no. 38 (2011), http://ieeexplore.ieee.org/xpl/articleDetails.jsp?arnumber=6154359.

[106] P. Marciniewski, Department of Physics and Astronomy, Uppsala University, Sweden, http://katalog.uu.se/orgInfo/?orgId=X208, 2010-12.

[107] Documentation about Xilinx virtex-5 FPGA, http://www.xilinx.com/support/documentation/virtex-5.htm.

[108] Qiang Wang et al., Real Time Conference, 2009. RT '09. 16th IEEE-NPSS page no. 571 (2009), http://ieeexplore.ieee.org/xpl/articleDetails.jsp?arnumber=5321411.

[109] WASA (Wide Angle Shower Apparatus), http://www2.fz-juelich.de/ikp/wasa/index.shtml.

[110] PCI Industrial Computers Manufactures Group (PICMG): Advanced Telecommunications Computing Architecture (ATCA), http://www.picmg.org/v2internal/specifications2.cfm?thetype=One&thebusid=2.

[111] M. Vencelj et al., Nucl. Instrum. and Meth. Phys. Res. A **607**, 581 (2009), http://www.sciencedirect.com/science/article/pii/S0168900209012042.

[112] F. Belli et al., Nucl. Instrum. and Meth. Phys. Res. A **595**, 512 (2008), http://www.sciencedirect.com/science/article/pii/S0168900208008759.

[113] Paul A. B. Scoullar and Robin J. Evans, IEEE NSS conference proceedings, N18-4 page no. 1668 (2008), http://ieeexplore.ieee.org/xpl/articleDetails.jsp?arnumber=4774724.

[114] GSI Multi-Branch System (MBS), http://www-win.gsi.de/daq/.

[115] Creative Electronic Systems (CES), Geneva, Switzerland, http://www.ces.ch/board-products/vme-single-board-computers.

[116] TRIVA Trigger module developed at GSI, http://www.gsi.de/en/work/organisation/scientific_technological_divisions/experiment_elektronik/elektronik_entwicklung/digitalelektronik/module/trigger_synchronisation/triva3.htm.

[117] GSI Object Oriented On-line Off-line (Go4) system, http://www-win.gsi.de/go4/.

[118] CERN - Accelerator Complex, http://public.web.cern.ch/public/en/research/CERNAccel-en.html.

[119] F. Schreuder, Improved design of a four-stage shaper for FEE of the PANDA EMC, private communication, KVI Groningen, March-April 2012.

[120] A.R. Gabler et al., Nucl. Instrum. and Meth. Phys. Res. A **346**, 168 (1994), http://www.sciencedirect.com/science/article/pii/0168900294907013.

[121] A. Galoyan and V. V. Uzhinsky, AIP Conf. Proc. **796**, 79 (2005), http://dx.doi.org/10.1063/1.2130140.

[122] Johan Messchendorp and the PANDA collaboration, Journal of Physics: Conference Series **219**, 042016 (2010), http://stacks.iop.org/1742-6596/219/i=4/a=042016.

[123] J. Stein, F. Scheuer, W. Gast, and A. Georgiev, Nucl. Instrum. and Meth. Phys. Res. A **113**, 141 (1996), http://www.sciencedirect.com/science/article/pii/0168583X95014179.

[124] A. Georgiev and W. Gast, IEEE Trans. Nucl. Sci. **NS-40**, 770 (1993), http://ieeexplore.ieee.org/xpls/abs_all.jsp?arnumber=256659.

[125] Gap Pad - a thermally conductive, electrically insulating, unreinforced gap filling material, http://www.bergquistcompany.com/thermal_materials/gap_pad/gap-pad-2500.htm.

[126] Cooled alcohol was circulated using, LAUDA Low-temperature thermostats and circulation chiller (RK8KS), http://www.lauda-brinkmann.com/.

[127] Mainz Microtron (MAMI) accelerator facility, http://www.kph.uni-mainz.de/eng/108.php.

[128] J. C. McGeorge et al., European Physical Journal A **37**, 129 (2008), http://link.springer.com/article/10.1140/epja/i2007-10606-0.

[129] Takashi Nishizawa, Project report: The evaluation of the pre-amplifier developed for PWO-II crystal read-out, KVI Groningen, Sept. 2012.

[130] Junguang Lu, Status of CsI(Tl) EMC, BESIII Collaboration Spring Meeting, Jan. 23, 2007.

[131] He Miao, 14th International Conference on Calorimetry in High Energy Physics, IHEP, Beijing, 11 May 2010, http://indico.ihep.ac.cn/conferenceOtherViews.py?view=standard&confId=910.

[132] Ping Rong-Gang, Chinese Physics C **32**, 599 (2008), http://stacks.iop.org/1674-1137/32/i=8/a=001.

[133] He Miao, Journal of Physics: Conference Series **293**, 012025 (2011), http://stacks.iop.org/1742-6596/293/i=1/a=012025.

[134] Kati Lassila-Perini, CMS Conference report: Reconstruction of Higgs decays to gamma gamma, CMS CR-1997/006, 30 January 1997, cdsweb.cern.ch/record/687568/files/cr97_006.pdf.

[135] He Miao et al., Chinese Physics C **32**, 269 (2008), http://stacks.iop.org/1674-1137/32/i=4/a=006.

[136] A Satpathy et al., Nucl. Instrum. and Meth. Phys. Res. A **391**, 423 (1997), http://www.sciencedirect.com/science/article/pii/S0168900297005123.

[137] Rihua Mao et al., Journal of Physics: Conference Series **293**, 012012 (2011), http://iopscience.iop.org/1742-6596/293/1/012012/.

[138] M. Ablikim et al. (BESIII Collaboration), Determination of the number of psi(3686) events at BESIII, http://arxiv.org/abs/1209.6199, 2012.

[139] M. Ablikim et al. (BESIII Collaboration), Phys. Rev. Lett. **109**, 172002 (2012), http://link.aps.org/doi/10.1103/PhysRevLett.109.172002.

# Acronyms

| | |
|---|---|
| **ALICE** | A Large Ion Collider Experiment |
| **APD** | Avalanche Photo Diode |
| **APFEL** | ASIC for PANDA Front-end Electronics |
| **ASIC** | Application Specific Integrated Circuit |
| **ATCA** | Advanced Telecommunications Computing Architecture |
| **ATLAS** | A Toroidal LHC Apparatus |
| **BEPC** | Beijing Electron Positron Collider |
| **BESIII** | Beijing Electron Spectrometer III |
| **BOSS** | BESIII Off-line Software System |
| **CES** | Creative Electronic Systems |
| **CFT** | Constant Fraction Timing |
| **CMS** | Compact Muon Solenoid |
| **CN** | Compute Node |
| **CR** | Collecter Ring |
| **CsI** | Cesium Iodide |
| **DAQ** | Data AcQuisition |
| **DC** | Data Concentrator |
| **DDR RAM** | Double Data Rate Random-Access Memory |
| **DIRC** | Detection of Internally Reflected Cherenkov radiation |
| **DMUX** | Data MUltipleXer |
| **DPM** | Dual Parton Model |
| **DVCS** | Deep Virtual Compton Scattering |
| **DY** | Drell-Yan |

| | |
|---|---|
| **EFF** | Electromagnetic Form Factors |
| **EMC** | ElectroMagnetic Calorimeter |
| **FAIR** | Facility of Antiproton and Ion Research |
| **FE** | Feature Extraction |
| **FEE** | Frond-End Electronics |
| **FPGA** | Field Programmable Gate Array |
| **FWHM** | Full Width Half Maximum |
| **GEM** | Gas Electron Multiplier |
| **Go4** | GSI Object Oriented On-line Off-line system |
| **GSI** | Gesellschaft für SchwerIonenforschung |
| **GTL** | Global Trigger Logic |
| **HESR** | High Energy Storage Ring |
| **HEP** | High Energy Physics |
| **HL** | High Luminosity |
| **HR** | High Resolution |
| **IHEP** | Institute of High Energy Physics |
| **IPC** | Intellectual Property Core |
| **IP** | Interaction Point |
| **IPMC** | Intelligent Platform Management Controller |
| **KVI** | Kernfysisch Versneller Instituut |
| **LED** | Light Emitting Diode |
| **LHC** | Large Hadrom Collider |
| **LNP** | Low Noise Pre-amplifier |
| **LQCD** | Lattice Quantum Chromo Dynamics |
| **MAMI** | MAinz MIcrotron |
| **MBS** | Multi Branch System |
| **MCP PMT** | Micro-Channel Plate Photo-Multiplier Tube |
| **MC** | Monte Carlo |
| **MD** | Muon Detector |
| **MDC** | Multilayer Drift Chamber (in BESIII) |
| **MDC** | Mini Drift Chamber (in PANDA) |
| **MVD** | Micro Vertex Detector |
| **MWD** | Moving Window Deconvolution |

| | |
|---|---|
| **NIM** | Nuclear Instrumentation Module |
| **PANDA** | antiProton ANnihilation at DArmstadt |
| **PID** | Particle IDentification |
| **PWO** | Lead tungstate |
| **QCD** | Quantum Chromo Dynamics |
| **QDC** | Charge-to-Digital Converter |
| **QED** | Quantum Electro Dynamics |
| **RF** | Radio Frequency |
| **RMS** | Root Mean Square |
| **ROOT** | Object-Oriented C++ analysis package |
| **RPC** | Resistive Plate Chamber |
| **SADC** | Sampling Analog to Digital Converter |
| **SBR** | Signal-to-Background Ratio |
| **SiPM** | Silicon Photo-Multiplier |
| **SM** | Standard Model |
| **SODA** | Synchronization Of Data Acquisition |
| **STT** | Straw Tube Tracker |
| **TDC** | Time-to-Digital Convertor |
| **TDR** | Technical Design Report |
| **TOF** | Time-Of-Flight |
| **TTL** | Transistor Transistor Logic |
| **VHDL** | VHSIC Hardware Description Language |
| **VHSIC** | Very High-Speed Integrated Circuits |
| **VMC** | Virtual Monte Carlo |
| **VME** | VERSAModule Eurocard |
| **VPT/VPTT** | Vacuum Photo-Triode/Tetrode |

# List of Publications

## International Journals:

- *Pulse pile-up recovery for the front-end electronics of the PANDA Electromagnetic Calorimeter*, G. Tambave et al., JINST 7, 11001, 2012. http://iopscience.iop.org/1748-0221/7/11/P11001
- *Trigger-less readout system with pulse pile-up recovery for the PANDA Electromagnetic Calorimeter*, M. Kavatsyuk et al. (G. Tambave), NIMA proceedings, 2011. http://dx.doi.org/10.1016/j.nima.2012.10.007
- *VHDL implementation of feature-extraction algorithm for the PANDA electromagnetic calorimeter*, E. Guliyev et al. (G. Tambave), NIMA, 664, 22-28, 2012. http://dx.doi.org/10.1016/j.nima.2011.10.016
- *Systematic study of (n, p) reaction cross sections from the reaction threshold to 20 MeV*, B. Lalremruata et al. (G. Tambave), Phy. Rev. C, 85, 024624, 2012. http://prc.aps.org/abstract/PRC/v85/i2/e024624
- *Performance of cooled PWO scintillators with signal-sampling readout*, H. Löhner et al. (G. Tambave), IEEE Transactions on Nuclear Science, Volume: PP, Issue: 99, 1, 2012. http://ieeexplore.ieee.org/xpls/abs_all.jsp?arnumber=6170599
- *Production of hypernuclei in peripheral HI collisions: The HypHI project at GSI*, Saito T. et al. (G. Tambave), Nuclear Physics A, 881, 218-227, 2012. http://dx.doi.org/10.1016/j.nuclphysa.2012.02.011
- *Performance of the prototype of the EMC for PANDA*, M. Kavatsyuk et al. (G. Tambave), NIMA 648, 77-91, 2011. http://dx.doi.org/10.1016/j.nima.2011.06.044

- *Front-End Electronics and Feature-Extraction Algorithm for the PANDA Electromagnetic Calorimeter*, M. Kavatsyuk et al. (G. Tambave), Journal of Physics: Conf. Series, 2011, 293 (1), art. no. 012020, 2011. http://iopscience.iop.org/1742-6596/293/1/012020
- *The HypHI Phase0 experiment*, Saito T. et al. (G. Tambave), Nuclear Physics A, 835, 110-116, 2010. http://dx.doi.org/10.1016/j.nuclphysa.2010.01.182
- *Technical Design Report for the: PANDA Straw Tube Tracker*, PANDA Collaboration, arXiv:1205.5441, 2012. http://arxiv.org/abs/1205.5441

## Conference proceedings/talk:

- *Verification of pile-up recovery for the FEE of the PANDA EMC*, G. Tambave, Oral presentation, NSS IEEE 2012, Oct. 29 - Nov.3, 2012, Anaheim, California, USA.
- *Trigger-Less Readout of the PANDA EMC*, M. Kavatsyuk et al. (G. Tambave), in Conf. Record, NSS IEEE 2012, Oct. 29 - Nov.3, 2012, Anaheim, California, USA.
- *Pulse pile-up recovery for the front-end electronics of the PANDA EMC*, G. Tambave et al., NSS IEEE 2011, Conf. Record, 2163-2168. http://ieeexplore.ieee.org/xpl/articleDetails.jsp?arnumber=6154438
- *Trigger-less readout electronics for the PANDA EMC*, M. Kavatsyuk et al. (G. Tambave), NSS IEEE 2011, Conf. Record, 43-47. http://ieeexplore.ieee.org/xpl/articleDetails.jsp?arnumber=6154360
- *VHDL implementation of feature-extraction algorithm for the PANDA EMC*, M. Kavatsyuk et al. (G. Tambave), NSS IEEE 2010, Conf. Record, 785-788. http://ieeexplore.ieee.org/xpl/articleDetails.jsp?arnumber=5873866
- *Feature-extraction algorithms for the PANDA EMC*, M. Kavatsyuk et al. (G. Tambave), NSS IEEE 2009, Conf. Record, pages: 210-213. http://ieeexplore.ieee.org/xpl/articleDetails.jsp?arnumber=5401798

# Acknowledgement

Scientific research is hardly accomplished by a single person and often results from a collaborative effort. Many people supported the work documented in this thesis and I would like to thank every one of them.

At first, I would like to thank the University of Groningen for the financial support received from the Ubbo Emmius fellowship during the past four years. I acknowledge the continuous support, help and valuable advices obtained from my PhD supervisor and promotor Prof. Herbert Löhner and from my copromotor Dr. Myroslav Kavatsyuk. Their support and strong motivation has played an important role for the completion of my thesis work.

I thank Herbert for his guidance and valuable suggestions in the course of the PhD research. He was very energetic, supportive, responsible and caring all the time. I deeply appreciate all his efforts in carefully reading the thesis manuscript and contributing to its improvement. I thank him in particular for his understanding, encouragement and patience during the past four years.

I am thankful to Myroslav for his judgment and dedication as a supervisor. He provided valuable support whenever I was in trouble. I have learned a lot of things from him such as writing a shell script, C++ programming, and simple tricks in experimentation and data analysis. I enjoyed traveling with him for experiments and conferences.

I am very thankful to the members of the reading committee, Prof. Egle Tomasi-Gustafsson, Prof. Kai-Thomas Brinkmann and Prof. Nasser Kalantar-Nayestanaki, for their efforts in carefully reading my thesis and providing me clarifying questions and valuable comments. I thank Nasser for inviting me to the KVI for a PhD interview.

In the PANDA collaboration, I would like to express my thanks to the following people:
Dr. Paola Gianotti for carefully reading our JINST paper-draft and providing useful comments; Dr. Fritz-Herbert Heinsius and his team at the University of Bochum, Dr. Rainer Novotny, Dr. Peter Drexler and their team at the University of Giessen for their kind support and hard work during the beam times at CERN and Mainz; Dr. Pawel Marciniewski and his colleagues at Uppsala University for the fruitful collaboration in the development of the PANDA EMC digitizer and multiplexer; Dr. Stefano Spataro, Dr. Johan Messchendorp, Dr. Bertram Kopf, Mohammad Babai, Dr. Hossein Moeini and Dr. Aleksandra Biegun for their help in the PandaROOT simulations and Olga Bondarenko, He maio, and Gianluca Inguglia for their help during the BESIII studies. I thank Johan for his important suggestions during the weekly meetings.

I feel lucky to have worked in the PANDA and BESIII collaborations. I appreciate the hard work of all the collaboration members in making the experiment and the respective developments possible and successful.

I would like to thank the following people from the KVI:
Peter Lemmens, Frans Schreuder, Peter Schakel, Michel Hevinga, Rene Speelman and all other electronics engineers for their continuous support and endless effort in the development of the trigger-less readout chain; Henk Smit and his mechanical engineering team and all engineers in the mechanical workshop for their help during the design and development phase of the EMC prototype; the vacuum department for an uninterrupted supply of Nitrogen gas; Hilde van der Meer for her kind support and help with many official documents. Marjan Koopmans for her excellent organization of the FANTOM weeks. I'm grateful to all other departments and employees of the KVI for their direct or indirect support in the past four years.

I enjoyed sharing an office with Ali Najafi and Wouter Dekens. I am grateful to Wouter for helping me with the Dutch translation of my thesis summary (Samenvatting), which allowed me to complete my thesis officially. I thank Ali, Daren, Elmaddin, Olga, Olena, Qader and Wouter for having fruitful discussions and all kind of help and support during my stay at KVI. I thank all present and former PhD students at the KVI for their direct or indirect support during the past four years. I enjoyed working in the lab with project students: Niklas, Svende, Miguel, Keesjan, Wilco, and Takashi. I thank all the named and unnamed people who had been supportive.

Finally, I would like to thank my family, in particular, my parents and Shruti, for their love, patience, encouragement and support throughout the past four years and before.